

REPORT DOCUMENTATION PAGE

Form Approved
OMB No. 0704-0188

Public reporting burden for this collection of information is estimated to average 1 hour per response, including the time for reviewing instructions, searching data sources, gathering and maintaining the data needed, and completing and reviewing the collection of information. Send comments regarding this burden estimate or any other aspect of this collection of information, including suggestions for reducing this burden to Washington Headquarters Service, Directorate for Information Operations and Reports, 1215 Jefferson Davis Highway, Suite 1204, Arlington, VA 22202-4302, and to the Office of Management and Budget, Paperwork Reduction Project (0704-0188) Washington, DC 20503.

PLEASE DO NOT RETURN YOUR FORM TO THE ABOVE ADDRESS.

1. REPORT DATE (DD-MM-YYYY)		2. REPORT TYPE Final Technical Report		3. DATES COVERED (From - To) 01 May 2004 – 31 Dec 2006	
4. TITLE AND SUBTITLE Advancing Detached-Eddy Simulation				5a. CONTRACT NUMBER FA9550-04-1-0030	
				5b. GRANT NUMBER	
				5c. PROGRAM ELEMENT NUMBER	
6. AUTHOR(S) Dr. Kyle D. Squires				5d. PROJECT NUMBER	
				5e. TASK NUMBER	
				5f. WORK UNIT NUMBER	
7. PERFORMING ORGANIZATION NAME(S) AND ADDRESS(ES) Mechanical and Aerospace Engineering Department Arizona State University Tempe AZ 85287				8. PERFORMING ORGANIZATION REPORT NUMBER	
9. SPONSORING/MONITORING AGENCY NAME(S) AND ADDRESS(ES) Air Force Office of Scientific Research (AFOSR) 875 N. Arlington St., Rm. 3112 Arlington, VA 22203 <i>Dr Rhett Jeffries/NA</i>				10. SPONSOR/MONITOR'S ACRONYM(S) AFOSR	
				11. SPONSORING/MONITORING AGENCY REPORT NUMBER	
12. DISTRIBUTION AVAILABILITY STATEMENT DISTRIBUTION A: Approved for public release; distribution unlimited.				AFRL-SR-AR-TR-07-0507	
13. SUPPLEMENTARY NOTES					
14. ABSTRACT Measurements show that the flow over the Aerospatiale A-airfoil experiences a laminar separation in the vicinity of the leading edge region, just downstream of the peak negative pressure along the suction side. Transition occurs in the separated shear layer with the reattached turbulent boundary layer evolving further along the suction side prior to a subsequent separation near the trailing edge. The laminar separation and transition is accounted for using the triplex approach outlined by Travin (57). The triplex approach provides a means to accommodate the laminar separation and transition in the separated shear layer, in the present calculations represented by an activation of the turbulence model. The eddy viscosity upstream of the airfoil is zero, non-zero values are seeded into the suction side of the airfoil using a boundary layer trip.					
15. SUBJECT TERMS					
16. SECURITY CLASSIFICATION OF:		17. LIMITATION OF ABSTRACT	18. NUMBER OF PAGES	19a. NAME OF RESPONSIBLE PERSON	

Advancing Detached Eddy Simulation

Kyle D. Squires
Mechanical and Aerospace Engineering Department
Arizona State University
P.O. Box 876106
Tempe, AZ 85287 USA

Sponsored by:
Air Force Office of Scientific Research



20071121027

Executive Summary

Accurate prediction of turbulent flows at high Reynolds numbers and with substantial effects of separation constitute a regime of significant engineering interest. Solutions of the Reynolds-averaged Navier-Stokes (RANS) equations are unable to represent the complex physics of most separated flows to sufficient accuracy. Large-Eddy Simulation (LES) provides a more realistic treatment of the separated regions of a turbulent flow but is prohibitively expensive when applied to whole domains at high Reynolds numbers. Detached-Eddy Simulation is a hybrid method, combining RANS and LES, and attempts to take advantage of both techniques in regions where each is accurate and computationally feasible. In natural applications of the method, attached boundary layers are entrusted to the RANS model with detached regions of the flow predicted using LES.

While DES is now relatively well understood in massively separated flows characterized by thin boundary layers prior to separation, an incorrect behavior can be encountered in flows with thick boundary layers and/or shallow separations. This motivated a detailed study of the flow physics and grid-sensitivity of the solutions in the flow over an Aerospatiale A-airfoil at an angle-of-attack of $\alpha = 13.3^\circ$ and at a chord-based Reynolds number of 2.1×10^6 . This flow has been measured in separate experiments (29), (30) and was the subject of a coordinated set of investigations through the LESFOIL project (31). The flow is a useful test case since problems can arise when the grid spacing parallel to the wall ($\Delta_{||}$) becomes less than the boundary layer thickness (δ), which is possible either through grid refinement and/or boundary layer thickening. In this regime, the grid spacing is then fine enough for the DES length scale to take its LES value within the boundary layer. This lowers eddy viscosity levels below that which would be given by the RANS model. Resolved stresses that are derived from velocity fluctuations (“LES content”) may not yet have been generated or might be weak. Additionally, LES content may be lacking because the grid or time step are not fine enough to fully support it, and/or because of delays in its generation by flow instabilities. The lower total stress reduces the skin friction, which can lead to premature separation in extreme cases.

To address these deficiencies, a new version of the technique known as Delayed-Detached Eddy Simulation (23) (DDES) has been developed. In natural applications of the method, DDES over-rides the DES limiter and maintains RANS behavior in the boundary layers regardless of the grid spacing. The new version has been tested on the flow over the Aerospatiale A-airfoil. To ensure that the new version does not degrade predictions in massively separated flows, the flow over a circular cylinder at Reynolds numbers corresponding to 1.4×10^5 and 8×10^6 has also been analyzed. RANS predictions of the flow over an Aerospatiale A-airfoil at a chord-based Reynolds number of 2.1×10^6 at two lower angles of attack have also been included. The DDES results of the flow over the Aerospatiale A-airfoil are essentially grid independent and match well with the RANS results. In contrast, the DES results exhibit premature separation occurring in two of the

grids. The eddy viscosity profiles showed the depletion of modeled stresses with the use of finer grids in DES, as a result of the RANS-LES interface moving well within the boundary layer. The flow over the circular cylinder at a Reynolds number of 8×10^6 showed that the DES and DDES predictions are similar with good agreement between the statistics using the two models.

While the new method addresses natural DES applications, the other primary thrust of the current work reported in this document focuses on the transition from RANS to LES behavior in DES along the main flow direction. This can result in applications because of streamwise grid refinement as required for resolution of flow features or changes in geometry that demand streamwise grid refinement. This part of the work is further motivated by flows characterized by shallow separations where RANS models may not provide sufficient accuracy and an LES treatment is desired in order to improve accuracy.

The transition from RANS to LES has typically been studied with evolution normal to the wall, as in the wall-layer modeling work of Nikitin *et al.* (72). Whatever the mechanism, as the flow enters the LES region, a DES solution is characterized by a reduction in the modeled length scale which draws down the eddy viscosity, thereby lowering the modeled stress. This reduction in modeled stress requires a corresponding increase in the resolved stress near the transition layer in order to avoid degrading predictions of the boundary layer. One of the techniques that can be applied to quickly increase resolved stresses is to seed the near-wall flow with fluctuations in order to quickly generate three-dimensional structure. A scheme has been developed and tested that generates velocity fluctuations using a stochastic force added to the momentum equations and subsequent tuning of the amplifications based on a prescribed shear stress profile. An adaptive control scheme has been used to shape the velocity fluctuations to mimic realistic flow features and optimized to achieve realistic Reynolds shear stresses with minimal computational effort.

Before arriving at the adaptive control scheme, the control process was thoroughly investigated and an analysis of the behavior of the errors using Proportional-Integral (PI) controllers and integral controllers was carried out. These simulations also revealed that specification of controller gains that ensure stability of the system is not simple. Therefore, the main advantage of using the adaptive control scheme is that it obviates the need to specify these controller gains that ensure numerical stability. The adaptive control method is based on the MIT rule which is an adaptive control methodology proposed by Whitaker (75). Using the method, the system is initially in the open-loop configuration with no control forces being applied. The gain values are then continuously altered during the simulation in an adaptive manner. The alteration of gains is based on a law that involves approximating a gradient-descent procedure seeking the minimum of an integral-squared performance criterion. The scheme has been tested using computations of turbulent channel flow at Reynolds numbers based on friction velocity and channel halfwidth of 5000. Simulation results show that the method proposed is effective in achieving the desired results with the resolved shear stress reaching the target levels at the control planes.

Simulations were conducted using coarse and fine grids, with wall-parallel grid spacings of approximately $1/10$ and $1/20$ of the boundary layer thickness, respectively. These simulations revealed that the finer grid is able to sustain turbulence downstream of the control planes and reduces the error in the wall shear stress from 20% to less than 10% for a channel with a streamwise extent of 4π and with the controllers taking up approximately 30% of the domain extent in the streamwise direction.

Contents

Executive Summary	i
Contents	v
1 Background	1
1.1 Direct Numerical Simulations	1
1.2 Large Eddy Simulation	3
1.2.1 Subgrid Scale Models	4
1.3 Reynolds-averaged Navier-Stokes	4
1.3.1 Spalart-Allmaras One-Equation Model	6
1.3.2 Spalart-Allmaras model with rotation correction	7
1.3.3 Shear Stress Transport model	8
1.4 Detached Eddy Simulation	9
2 Delayed Detached Eddy Simulation	15
3 Flow over a Circular Cylinder using DDES	17
3.1 Predictions at $Re = 1.4 \times 10^5$	19
3.2 Predictions at $Re = 8 \times 10^6$	23
4 Flow over the Aerospatiale A-airfoil	27
4.1 Predictions at $\alpha = 13.3^\circ$	27
4.2 Approach	27
4.2.1 Flow solver and grids	28
4.2.2 Results	30
4.2.3 Tripless and Fully Turbulent solutions	30
4.2.4 Skin friction coefficient	32
4.2.5 Streamwise and wall-normal velocity profiles	34
4.2.6 Eddy viscosity ratio	35
4.2.7 Tabulations of Lift and Drag coefficients	39
4.3 Flow over the Aerospatiale A-Airfoil at $\alpha = 12.3^\circ$	39
4.4 Flow over the Aerospatiale A-Airfoil at $\alpha = 7.2^\circ$	41
5 Seeding boundary layer turbulence in WMLES	47
5.1 Introduction	47
5.2 Synthetic turbulence	50
5.3 Boundary layer stirring and control methodology	51

5.4	Simulation overview	54
5.4.1	Numerical method	54
5.4.2	Computational grid	55
5.5	Design of the controllers	56
5.5.1	Identification of a linear model	56
5.5.2	Closing the loop and obtaining the gain values	58
5.5.3	Accuracy of the linear model	60
5.5.4	Reduction of the order of the linear model using Proper Orthogonal De- composition (POD)	61
5.5.5	Method based on non-linear system response	64
5.5.6	Difference between PI controllers and integral controllers	64
5.5.7	Characterization of the terms contributing to the error	65
5.5.8	Non-linear PI controller	70
5.5.9	Effect of time-averaging in the control formulation	70
5.5.10	Adaptive control methodology to specify the controller gains	73
5.6	Flow visualizations	75
5.7	Resolved stress and wall stress	77
5.8	Influence of the stirring force	80
5.9	Synthetic turbulence generation with controlled forcing	82
6	Summary	86

1 Background

Predicting turbulent flows constitutes one of the principal challenges of physics. The non-linearity and chaotic nature of the solutions and influence of complicating features such as the Reynolds number and presence of a solid surface substantially challenge simulation strategies. As described by Spalart, there are two main challenges in the prediction of turbulence (49):

- Prediction of growth and separation of the boundary layer;
- Prediction of momentum transfer after separation.

The most commonly used simulations strategies range from solution of the steady Reynolds-averaged Navier-Stokes (RANS) equations to Large Eddy Simulation (LES) to Direct Numerical Simulation (DNS). In the recent past, a number of hybrid strategies have emerged, motivated by both the strengths and limitations RANS and LES. The most popular of these hybrid methods include Detached Eddy Simulations (DES), Very-Large Eddy Simulation (VLES), and Unsteady Reynolds Averaged Navier-Stokes (URANS) solutions.

With the obvious exception of DNS, simulation strategies for applications require empirical input. As described in Spalart (49), it appears that complex modeling strategies sometime advocated for RANS approaches offer relatively little advantage in the prediction of the growth and separation of a boundary layer, as most simple RANS models have been calibrated in thin shear layers. Predicting momentum transfer after separation is more challenging and hybrid strategies as well as complex RANS models have distinct advantages over simple schemes. While some strategies involve extensive use of empirical inputs into models, others such as LES involve much less empiricism. In some strategies, grid refinement merely improves the numerical accuracy of the solution, and in others, we could obtain richer turbulence physics by employing a finer mesh. The final selection of a turbulence strategy to predict a flowfield is inevitably a compromise between accuracy and computational efficiency.

1.1 Direct Numerical Simulations

In this approach, which is free from any empiricism, the entire range of turbulent scales are resolved. In DNS, the Navier-Stokes equations are solved without any modeling. DNS is the most fundamental technique as it provides detailed information about turbulence, which can be difficult to obtain in experiments. Since all the scales of turbulence are to be resolved using DNS, the gridding requirements are stringent, and it must be ensured that DNS grids are fine enough to resolve the smallest scales while the domain should be large enough to contain an adequate sample of the largest eddies.

In most turbulent flowfields, energy is supplied via interactions between the turbulence and mean flow gradients to the largest eddies (that have length scales L of the order of the domain),

and in turn transfer kinetic energy to the smaller scales until that energy is dissipated into heat at the smallest scales (the Kolmogorov length scale η). The large eddies are influenced by the domain and are anisotropic. This anisotropy is lost during the process of the energy cascade and the smallest eddies are assumed isotropic.

If the rate of dissipation of turbulent kinetic energy (k) is c , then it would be possible to define turbulent lengthscales and turbulent timescales on this basis. By noticing that $u = \sqrt{k}$ is a velocity scale, the large eddy length scale can be defined as:

$$L = T\sqrt{k} = \frac{k^{3/2}}{\epsilon} \quad (1)$$

where T is a timescale for energy dissipation ($T = k/\epsilon$), which is the ratio of the turbulent kinetic energy to (k) the rate of dissipation (ϵ) of turbulent kinetic energy. This quantity is also referred to as the integral timescale. Since the smallest scales of motion have little energy, it would not be logical to use k to define a timescale for these scales. As the smallest scales are diffused by viscosity, it is appropriate to form a timescale using ν (viscosity) and ϵ .

$$T_\eta = \sqrt{\frac{\nu}{\epsilon}} \quad (2)$$

T_η is referred to as the dissipative timescale. Therefore, the ratio of the timescales of the large and small eddies is,

$$\frac{T}{T_\eta} = \sqrt{\frac{k^2}{\epsilon\nu}} \quad (3)$$

Similar to the definition of the large eddy lengthscale, the lengthscales of the smallest scales of motion (η) can be defined using ν and ϵ :

$$\eta = \left(\frac{\nu^3}{\epsilon}\right)^{1/4} \quad (4)$$

The ratio of the largest lengthscale (L) to the smallest lengthscale (η) is given by:

$$L/\eta = \frac{k^{3/2}}{\epsilon^{3/4}\eta^{3/4}} \quad (5)$$

$$L/\eta = Re_L^{3/4} \quad (6)$$

This implies that a three-dimensional DNS requires the number of mesh points proportional to $(Re^{3/4})^3$ (24). Similarly, the ratio of the integral timescale (T) to the dissipative timescale (T_η) is a function of the Reynolds number ($Re_L^{1/2}$) (24). It is also important that the integration of the solution in time must be done with a time-step (Δt), small enough that a fluid particle moves only a fraction of the mesh spacing (Δx) in each step. This restriction is in the form of a Courant number (C).

$$C = \frac{u\Delta t}{\Delta x} < 1 \quad (7)$$

The total simulation time is generally proportional to the turbulence timescale given by:

$$\tau = \frac{L}{u} \quad (8)$$

Combining the above relations and because Δx should be of the order of η , the number of time-integration steps must be proportional to $L/C\eta$. Since $L/\eta = Re_L^{3/4}$, one can estimate that the number of floating point operations required to complete the simulation is proportional to the mesh points and the number of time-steps. Thus, the CPU time grows as Re_L^3 (25). Due to the prohibitive computational cost, the application of DNS to complex flows at high Reynolds numbers is problematic. However, DNS remains a useful and powerful technique to compute low Reynolds number flows, and provides pathways to understanding physical mechanisms.

1.2 Large Eddy Simulation

Large Eddy Simulation is a technique in which the time-dependent equations are solved for the large scale motions. The small scale turbulence that cannot be resolved by the mesh are approximated using model aptly referred to as a ‘‘subgrid-scale model’’. Such an approach is grounded in the realizatino that most of the energy is carried by the larger eddies and current computing capacity is sufficient to solve the time-dependent equations that can resolve these eddies. According to Chapman (22), the computational cost of LES for wall-bounded flows with near-wall resolution increases with the Reynolds number as $Re^{1.8}$. However, boundary-layer grids should still sufficiently resolved in the wall-parallel directions to accurately resolve the near-wall eddies, which are in fact the large eddies close to a solid surface. Notwithstanding the use of the best wall-layer treatment, LES, is far from affordable in complex aerodynamic calculations (49).

Subgrid scale (SGS) models are typically based on the fact that the global dissipation level is set by the largest eddies and the smaller eddies exhibit similar behavior while transmitting energy to the smallest scales (25). Therefore, the energy content carried by smaller eddies is represented statistically, using a closure model. The small scale quantities are separated from the large scale quantities by means of a spatial filtering operation,

$$\bar{f}(\vec{x}) = \int f(x')G(\vec{x} - \vec{x}'; \Delta)dx', \quad (9)$$

where G is the filter function and Δ is the filter width.

Applying the filtering operation to the momentum equations,

$$\frac{\delta \bar{u}_i}{\delta t} + \frac{\delta}{\delta x_j}(\bar{u}_i \bar{u}_j) = -\frac{1}{\rho} \frac{\delta \bar{p}}{\delta x_i} - \frac{\delta \tau_{ij}}{\delta x_j} + \nu \frac{\delta^2 \bar{u}_i}{\delta x_j \delta x_j} \quad (10)$$

where the subgrid scale stress $\tau_{ij} = \overline{u_i u_j} - \bar{u}_i \bar{u}_j$. Traditionally, the SGS stresses that are modeled are divided into three contributions (25),

- The resolvable part - Leonard stresses $L_{ij} = \overline{\bar{u}_i \bar{u}_j} - \bar{u}_i \bar{u}_j$
- The cross terms $C_{ij} = \overline{\bar{u}_i u'_j}$
- The SGS Reynolds stresses, $R_{ij} = \overline{u'_i u'_j}$

Eddy viscosity models are commonly used for closure, and these relate the anisotropic part of the SGS stress tensor to the strain rate tensor:

$$\tau_{ij} - \delta_{ij}/3\tau_{kk} = -2\nu_t \bar{S}_{ij} = -\nu_t \left(\frac{\partial \bar{u}_i}{\partial x_j} + \frac{\partial \bar{u}_j}{\partial x_i} \right) \quad (11)$$

1.2.1 Subgrid Scale Models

A number of SGS models have been developed with the most popular including the Smagorinsky model, scale similarity models, Renormalization Group models (RNG) theory models, and dynamic sub-grid scale models (20). One of the commonly used subgrid scale model based on the eddy viscosity concept is the Smagorinsky model. The model lengthscale is given by $l = C_S \Delta$ where C_S is the Smagorinsky constant and Δ being the filter width. The velocity scale is obtained by assuming that the smaller scales are in equilibrium and the energy obtained from the larger scales is dissipated instantaneously and completely to the smaller scales.

$$\nu_t = C_S^2 \Delta^2 |\bar{S}|, \quad |\bar{S}| = (2\bar{S}_{ij}\bar{S}_{ij})^{\frac{1}{2}} \quad (12)$$

1.3 Reynolds-averaged Navier-Stokes

RANS techniques are based on the Reynolds decomposition according to which a flow variable is decomposed into a mean quantity and a fluctuating quantity,

$$f(x, t) = \bar{f}(x) + f'(x, t) \quad (13)$$

where $f(x, t)$ is the flow variable, $\bar{f}(x)$ represents the mean value of the flow variable and $f'(x, t)$ represents the fluctuation from the mean. When this decomposition is applied to the Navier-Stokes equations, the result is an equation for the mean quantities containing an extra term known as the Reynolds stress tensor ($\tau = -\rho \overline{u'_i u'_j}$). The Reynolds stress tensor has nine components, and the term represents the average flux of the j-momentum along the i-direction, which is also equal to the average flux of the i-momentum along the j-direction (21). This quantity represents the transfer of momentum by the fluctuating motion into the mean flow and is subjected to closure modeling. The flow properties in a RANS calculation are typically subjected to time averaging defined by,

$$\bar{f}(\bar{x}) = \lim_{T \rightarrow \infty} \frac{1}{T} \int_t^{t+T} f(x', \tau) d\tau. \quad (14)$$

Closure modeling for the Reynolds stress term is usually accomplished by the use of simple eddy viscosity models. Most RANS models invoke the Boussinesq approximation and therefore imply an analogy between molecular and turbulent transport, linking the turbulent stress to the mean rate of strain using an eddy viscosity. This assumes that the turbulent eddies in a flow transfer momentum in much the same fashion as molecular interactions in a gas. One of the drawbacks of this analogy is that while molecular interactions occur at much smaller scales as compared to the length scales over which flow properties are changing, turbulent eddies have important interactions at scales that are comparable to the length scales of variation of the mean motion of the flow (24). In spite of this rather rough assumption, the eddy viscosity approach is widely, and often successfully, applied.

As described by Rodi (19), there are three general types of eddy viscosity models:

- Zero-equation models – ν_t is specified directly;
- One-equation models – the length scale is specified while the velocity scale is solved by a transport equation;
- Two-equation models – transport equations are used to solve for the length scale and velocity scale.

Zero-equation models are usually not preferred as they fail to take into account flow history effects and assume that turbulence is dissipated where it is generated, meaning that there is no transport of turbulence (19). One-equation and two-equation models are much more commonly employed in engineering practice.

RANS models do not work well in all cases as they are based on empiricism and calibrated in a simple pool of thin shear flows. It would be difficult to obtain accurate results for very complex flows and flows characterised by massive separation using RANS approaches (49). A number of different RANS models have been considered in the past with no particular model emerging as a superior model for all types of flows. As described by Hunt (68), in some cases the duration of a disturbance is smaller than the intrinsic time scale of the turbulence and, consequently, an erroneous turbulence model would have little effect on the mean flow. However, the turbulence model could result in inaccurate calculations for certain types of flows in which the intrinsic timescale is smaller than the distortion timescale, for example, in some shear flows (49). There is also a general agreement that the ultimate potential of eddy-viscosity models does not include separated flows over three-dimensional geometries (49).

The majority of modern models employed in practice are based on solution of transport equations for either the eddy viscosity itself (one-equation models) or equations for turbulence scales that are used to form the eddy viscosity (e.g., two-equation models such as $\mathcal{K} - \epsilon$). Some of the models which were used for predictions in the current work have been summarized in the following sections.

1.3.1 Spalart-Allmaras One-Equation Model

The Spalart-Allmaras (referred to as S-A throughout the document) model consists of a transport equation for the turbulent viscosity, developed using empiricism, dimensional analysis, Galilean invariance and selective dependence on molecular viscosity (27). The S-A model is local i.e., the equation at one point does not depend on the solution at other points, and is compatible with grids of any structure (27). Turbulence models developed prior to S-A, such as the Cebeci-Smith model (63), Baldwin-Lomax model (64) and the Johnson-King model (65) are boundary layer models in spirit, physically treating the whole boundary layer as a single tightly-coupled module, which becomes incorrect in the presence of detached and multiple shear layers. In their implementation, all of these earlier models relied on velocity and vorticity profiles varying along a smooth gridline, thus being non-local and restricted to structured grids. Further, these are algebraic models, and there are occasions such as the presence of two solid bodies in the flowfield which would require decisions that would not facilitate automation of the method. Some models such as the $k-\epsilon$ model (66) are local but lack accuracy in prediction of shock/boundary layer interactions or separations on smooth surfaces. The $k-\epsilon$ model may be suitable in predicting massively separated flows, but require finer grids near a wall, involve strong source terms that often degrade the convergence, and demand non-trivial upstream and freestream conditions for the turbulence variables. To offset the near-wall problems, wall functions are typically introduced, though which lose any justification in separated flows (27). While the Baldwin-Barth model (67) is an attractive intermediate which is local, and at the same time does not require a finer resolution than the velocity field itself.

The idea of developing the S-A model was prompted by the opinion that a one-equation model generated as a simplified version of the $k-\epsilon$ model is not optimal and that a one-equation model generated afresh, enabling fuller control over the performance of the model. For example, the Baldwin-Barth model was derived from the $k-\epsilon$ model, via assumptions and its diffusion term is constrained by virtue of the assumptions made.

The S-A model has similar properties as that of the Baldwin-Barth model in terms of compatibility with unstructured grids and near-wall behavior and is more robust. There are four versions, with the simplest applicable to free shear flows, to the most complete applicable to viscous flows past solid bodies and with laminar regions.

The S-A model solves an equation for the variable $\bar{\nu}$ which is dependent on the eddy viscosity. The model has been derived empirically rather than using transport equations, and includes a wall destruction term that reduces the eddy viscosity in the laminar sub-layer. The model also contains trip terms to provide smooth transition to turbulence if required. The model is given by:

$$\frac{D\bar{\nu}}{Dt} = C_{b1} (1 - f_{t2}) \tilde{S}\bar{\nu} + \frac{1}{\sigma} [\nabla \cdot ((\nu + \bar{\nu}) \nabla \bar{\nu}) + c_{b2} (\nabla \bar{\nu})^2] - \left[c_{w1} f_w - \frac{C_{b1}}{\kappa^2} f_{t2} \right] \left[\frac{\bar{\nu}}{d} \right]^2 + f_{t1} \Delta U^2. \quad (15)$$

The eddy viscosity is obtained via,

$$\nu_t = \tilde{\nu} f_{v1}, \quad f_{v1} = \frac{\chi^3}{\chi^3 + c_{v1}^3}, \quad \chi = \frac{\tilde{\nu}}{\nu}, \quad (16)$$

where ν is the molecular viscosity. The production term is given by,

$$\tilde{S} = S + \frac{\tilde{\nu}}{\kappa^2 d^2} f_{v2}, \quad f_{v2} = 1 - \frac{\chi}{1 + \chi f_{v1}} \quad (17)$$

where S is the magnitude of vorticity and d is the distance to the closest wall. The wall destruction function f_w is given by,

$$f_w = g \left(\frac{1 + c_{w3}^6}{g^6 + c_{w3}^3} \right)^{\frac{1}{6}}, \quad g = r + c_{w2}(r^6 - r), \quad r = \frac{\tilde{\nu}}{\tilde{S} \kappa^2 d^2}. \quad (18)$$

The trip functions in the model are given by,

$$f_{t1} = c_{t1} g_t \exp \left(-c_{t2} \frac{\omega_t^2}{\Delta U^2} [d^2 + g_t^2 d_t^2] \right), \quad g_t = \min \left(0.1, \frac{\Delta U}{\omega_t \Delta x_t} \right) \quad (19)$$

The trip function f_{t1} is specified in terms of the distance d_t from the field point to the trip, the wall vorticity ω_t at the trip and ΔU which is the difference between the velocity at the field point and that at the trip. The trip function f_{t2} is given as,

$$f_{t2} = c_{t3} e^{-c_{t4} \chi^2} \quad (20)$$

The wall boundary condition is $\tilde{\nu} = 0$. The constants are $c_{b1} = 0.1355$, $\sigma = \frac{2}{3}$, $c_{b2} = 0.622$, $\kappa = 0.41$, $c_{w1} = c_{b1}/\kappa^2 + (1 + c_{b2})/\sigma$, $c_{w2} = 0.3$, $c_{w3} = 2$, $c_{v1} = 7.1$, $c_{t1} = 1$, $c_{t2} = 2$, $c_{t3} = 1.1$ and $c_{t4} = 2$.

1.3.2 Spalart-Allmaras model with rotation correction

Spalart and Shur (52) proposed a modification to the Spalart-Allmaras model to account for streamline curvature and system rotation. The approach involves second-order derivatives of the velocity field. The S-A model with rotation correction consists of a modification to the source term ($C_{b1} \omega \tilde{\nu}$) that is multiplied by the rotation function f_{r1} , where $\tilde{\nu}$ is the modified eddy viscosity. The rotation function is defined as,

$$f_{r1}(r^*, \bar{r}) = (1 + c_{r1}) \left[\frac{2r^*}{1 + r^*} \right] [1 - c_{r3} \tan^{-1}(c_{r2} \bar{r})] - c_{r1} \quad (21)$$

where r^* and \bar{r} are nondimensional quantities given by,

$$r^* = \frac{S}{\omega}, \quad \bar{r} = \frac{2\omega_{ik} S_{jk} \left(\frac{DS_{ij}}{Dt} \right)}{D^4} \quad (22)$$

$$S_{ij} = 0.5 \left(\frac{\partial u_i}{\partial x_j} + \frac{\partial u_j}{\partial x_i} \right), \quad \omega_{ij} = 0.5 \left(\frac{\partial u_i}{\partial x_j} - \frac{\partial u_j}{\partial x_i} \right), \quad D^2 = \omega_{ij}^2 + S_{ij}^2 \quad (23)$$

1.3.3 Shear Stress Transport model

The Shear Stress Transport (SST) model was developed by Menter (74) to improve the accuracy of the k - ω model in the prediction of separated flows. The model combines k - ϵ and k - ω formulations, being identical to the k - ω model in the inner region of the boundary layer (up to approximately $\delta/2$) and gradually changes to k - ϵ model away from the walls and in the outer wake region. A blending function F_1 is introduced to bridge from k - ω near the wall to k - ϵ in the freestream. The transport equations governing k and ω take the form:

$$\frac{D(\rho k)}{Dt} = \tau_{ij} \frac{\partial u_i}{\partial x_j} - \beta \rho \omega k + \frac{\partial}{\partial x_j} \left[(\mu + \sigma_k \mu_t) \frac{\partial k}{\partial x_j} \right] \quad (24)$$

$$\frac{D\rho\omega}{Dt} = \frac{\gamma\rho}{\mu_t} \tau_{ij} \frac{\partial u_i}{\partial x_j} - \frac{\partial}{\partial x_j} \left[(\mu + \sigma_\omega \mu_t) \frac{\partial \omega}{\partial x_j} \right] + 2\rho(1 - F_1) \sigma_{\omega 2} \frac{1}{\omega} \frac{\partial k}{\partial x_j} \frac{\partial \omega}{\partial x_j} \quad (25)$$

where τ_{ij} is the modeled turbulent shear stress. The switching function F_1 is given by,

$$F_1 = \tanh(\arg_1^4) \quad (26)$$

$$\arg_1 = \min \left(\max \left(\frac{\sqrt{k}}{0.09\omega y}; \frac{500\mu}{\rho\omega y^2} \right); \frac{4\rho\sigma_{\omega 2}k}{CD_{k\omega}y^2} \right) \quad (27)$$

$$CD_{k\omega} = \max \left[2\rho\sigma_{\omega 2} \frac{1}{\omega} \frac{\partial k}{\partial x_i} \frac{\partial \omega}{\partial x_i}; 10^{-20} \right] \quad (28)$$

The switching (blending) function F_1 is also used to determine the values of the model constants. If ϕ_1 represents a generic constant in the k - ω equations and ϕ_2 represents the same constant in the k - ϵ equations, then the model constants employed in the transport equations for k and ω are obtained by,

$$\phi = F_1\phi_1 + (1 - F_1)\phi_2 \quad (29)$$

The turbulent eddy viscosity is determined by $\nu_t = k/\omega$. The SST model limits the turbulent shear stress to $\rho a_1 k$ where $a_1 = 0.31$. The expression for the eddy viscosity can therefore be obtained from,

$$\nu_t = \frac{a_1 k}{\max(a_1 \omega; \Omega F_2)} \quad (30)$$

where Ω is the absolute value of vorticity. The function F_2 is included to prevent singular behavior in the freestream where Ω goes to zero and is given by,

$$F_2 = \tanh(\arg_2^2) \arg_2 = \max \left(2 \frac{\sqrt{k}}{0.09\omega y}; \frac{400\nu}{y^2\omega} \right) \quad (31)$$

The k - ω model constants are given by $\sigma_{k1} = 0.85$, $\sigma_{\omega 1} = 0.5$, $\beta_1 = 0.0750$, $\beta^* = 0.09$, $\kappa = 0.41$, $\gamma_1 = \beta_1/\beta^* - \sigma_{\omega 1}\kappa^2/\sqrt{\beta^*}$. The values of the k - ϵ model constants are $\sigma_{k2} = 1$, $\sigma_{\omega 2} = 0.856$, $\beta_1 = 0.0828$, $\beta^* = 0.09$, $\kappa = 0.41$, $\gamma_2 = \beta_2/\beta^* - \sigma_{\omega 2}\kappa^2/\sqrt{\beta^*}$.

1.4 Detached Eddy Simulation

RANS approaches are often acceptable in the thin shear layers where the methods have been calibrated. In other regimes, especially flows in which the turbulent eddies are not “standard”, i.e., not in the calibration range of the model, the performance of RANS models is, at best, uneven. This in turn motivates other strategies, one of the primary alternatives being Large-Eddy Simulation (LES). The application of LES to prediction of turbulent flows in practical configurations is increasing, primarily in internal flows and especially to flows that include chemistry or contain more than one phase. Unfortunately, the computational cost which arises from the application of LES to a complete configuration such as an airplane, submarine, or road vehicle at practical Reynolds numbers is prohibitive. The high cost of LES arises because of the resolution requirements for the boundary layers, an issue that remains even with fully successful wall-layer modeling (49).

Hybrid methods combine RANS and LES techniques with the aim of capitalizing on the relative strengths of each approach. Perhaps the most widespread RANS-LES method in use today is Detached-Eddy Simulation (DES). DES was originally proposed by Spalart *et al.* (26) as a cost-effective and plausibly accurate approach for predicting flows experiencing massive separation. The method was originally intended to predict the entire boundary layer using a RANS model and with an LES treatment intended for the separated regions. DES has performed extraordinarily well, enabling computationally feasible predictions of a range of complex flows at high Reynolds numbers that are either difficult to model accurately using RANS or impose a computational cost that prevents the use of LES (16), (18), (17), (57). Given the successful applications of the technique to date, there is now strong interest in expanding the range of applications which may be accurately predicted using DES.

In the 1997 version of the method, DES and for that matter most other hybrid RANS-LES methods, the strategy is modification of the turbulence model to ensure a RANS treatment of the (thin) attached boundary layers and LES treatment of the detached boundary layers. The original formulation of the model proposed by Spalart *et al.* (26) achieved this behavior by modifying the length scale, d (the wall distance in the case of S-A), that enters the turbulence model and controls the eddy viscosity. The S-A-based DES formulation is achieved by re-defining the length scale in the S-A RANS model (shown here without the trip terms) from d to \tilde{d} in the destruction term of the model:

$$\frac{D\tilde{\nu}}{Dt} = c_{b1}\tilde{S}\tilde{\nu} - c_{w1}\left[\frac{\tilde{\nu}}{\tilde{d}}\right]^2 + \frac{1}{\sigma_\nu}\left[\nabla((\nu + \tilde{\nu})\nabla\tilde{\nu}) + c_{b2}|\nabla\tilde{\nu}|^2\right]. \quad (32)$$

If the production and destruction terms of the model are dominant, then

$$c_{b1}\tilde{S}\tilde{\nu} = c_{w1}\left(\frac{\tilde{\nu}}{\tilde{d}}\right)^2 \quad (33)$$

and consequently,

$$\tilde{\nu} \propto \tilde{S}\tilde{d}^2. \quad (34)$$

In the Smagorinsky model the eddy viscosity is proportional to the local rate of strain and filter width, i.e., $\nu_{sgs} = (C_s \Delta)^2 |\bar{S}|$ and the subgrid length scale is $l_{sgs} = C_s \Delta$ where C_s is the Smagorinsky constant and Δ is the filter width, typically taken as some measure of the local grid spacing. Equation (34) shows that a Smagorinsky-like form is achieved if \tilde{d} is made proportional to the grid spacing. In particular, the DES formulation is achieved by prescribing the model length scale as,

$$\tilde{d} \equiv \min(d, C_{DES} \Delta), \quad \Delta \equiv \max(\Delta x, \Delta y, \Delta z), \quad (35)$$

$$F_{DES} = \frac{\tilde{d}}{d} \quad (36)$$

where again d is the distance to the nearest wall, C_{DES} is a model constant to be determined, and Δ is a measure of the local grid spacing taken as the largest of the three grid spacings in each of the coordinate directions. Note also that the length scale should be changed from d to \tilde{d} everywhere it appears in the S-A model. Near a solid surface the wall-parallel grid spacings determine Δ (for RANS-type boundary layer grids) and are larger than the distance to the wall d . Thus, within the boundary where $d \ll \Delta$ boundary layer properties are predicted using the S-A RANS model. Away from the wall where $C_{DES} \Delta < d$, a Smagorinsky-like SGS model is obtained. The constant C_{DES} was set by Shur *et al.* (56) in computations of homogeneous and isotropic turbulence. The parameter F_{DES} 36 is defined as the ratio of the turbulent lengthscale to the wall-distance and is exactly equal to 1 at the RANS-LES interface.

As shown above, DES is based on a single turbulence model and is not zonal, i.e., with explicit declarations of zones as RANS or LES. The change in the length scale from the RANS form to that used in DES leads to a model that becomes region-dependent. In most cases a RANS model is active in the entire boundary layer with a subgrid-scale model active away from solid surfaces. A key feature that is common to classical LES is incorporation of the grid spacing, through the appearance of Δ . This is analogous to the foundation of LES in which there is a filter width that controls the end of the energy cascade, and can be reduced in order to increase the range of scales and therefore improve the physics of the simulation (49).

The RANS and LES regions are separated by an interface that corresponds to the location where the model length scale becomes proportional to Δ . This interface is dictated by the grid and can result in degradation of DES predictions. In the natural DES applications envisioned by Spalart *et al.* (26), the entire boundary layer is in ‘‘RANS mode’’, i.e., with a RANS model active, the RANS-LES interface is outside the boundary layer, and there are no adverse effects of the interface on boundary layer predictions. Grid refinement in the wall parallel directions (both streamwise and spanwise) will cause the RANS-LES interface to move closer to the wall and possibly within the boundary layer. This can activate the length scale switch to the LES branch ($\tilde{d} = C_{DES} \Delta$) and reduce eddy viscosity levels below that which would be obtained from the RANS model. The natural applications summarized in the next section focus on flows that experience massive separation. The flow around a circular cylinder, for example, is representative in that a boundary

layer thinned by acceleration along the body detaches into a region of massive separation. On grids that are typical for RANS prediction of the boundary layers in these and other flows, errors resulting from the RANS-LES interface are not encountered. A major issue in a DES is that a separating shear layer needs to generate random eddies which it did not possess in the boundary layer. This process of generating three-dimensional structures (“LES content”) is more easily accommodated by a thin shear layer rapidly departing from a wall. In massively separated flows at high Reynolds numbers instabilities in the detaching shear layers are rapidly amplified and three-dimensional structures quickly fill the wake.

Recently, Spalart *et al.* (23) have addressed the issue for natural DES applications where it is preferable to over-ride the DES limiter and maintain RANS behavior in the boundary layers, independent of Δ_{\parallel} relative to δ . This ensures that the eddy viscosity levels would be given by the RANS model in flows with thick boundary layers and shallow separation, thereby maintaining the correct levels of the total stress and skin friction. The issue addressed by Spalart *et al.* (23) is illustrated using Figure 1. Shown in the figure are three boundary layer grids. Figure 1a shows a “Type I” grid and is typical of RANS and of DES with a thin boundary layer where the wall-parallel spacings Δx or Δz set the length scale Δ , i.e., $\Delta = \max(\Delta x, \Delta y, \Delta z)$ and the DES length scale $\tilde{d} = d$ throughout the boundary layer since $C_{DES}\Delta > d$ for the Type I grid. This in turn implies that the RANS model is maintained throughout the boundary layer and DES functions as intended, i.e., an LES treatment is bypassed in large areas of thin boundary layers.

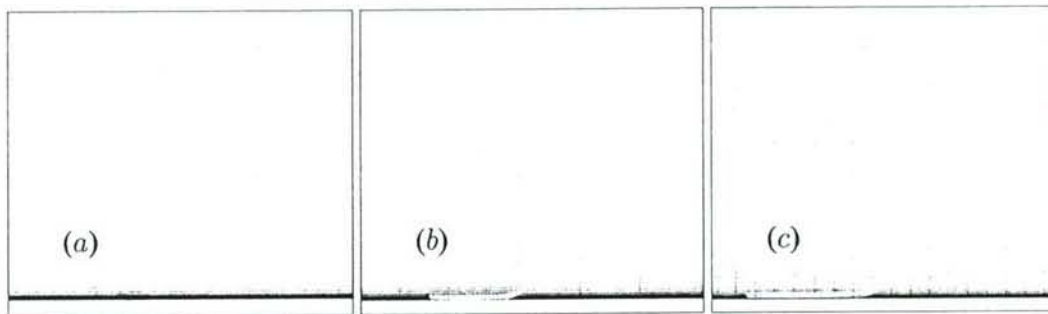


Figure 1: Boundary layer grids. (a) Type I grid for natural DES; (b) Type II ambiguous grid; (c) Type III grid for wall-layer modeling in LES.

The other extreme is Figure 1c which shows a “Type II”, grid with the wall-parallel grid spacings much smaller than δ ($\Delta \approx \delta/20$ is a reasonable value for wall-modeled LES (72)). In the Type III grid, the closure is a subgrid model throughout the bulk of the boundary layer ($\tilde{d} = C_{DES}\Delta$), and a RANS-like wall-layer model very close to the surface. Between the RANS-modeled-region and LES region is a grey area which has been the subject of significant attention (72). Type III grids are created by design for wall-modeled LES applications and related studies have been reported by Nikitin *et al.* (72) and Piomelli *et al.* (40).

Problems arise on the “ambiguous” Type II grid shown in Figure 1b. The grid resolution is sufficient to activate the DES limiter (i.e., cause $\tilde{d} = C_{DES}\Delta$) within the boundary layer though mesh spacings are not fine enough to support resolved velocity fluctuations (i.e., LES content). In this case the DES limiter reduces the eddy viscosity, and the modeled Reynolds stress, without the generation of any sizable resolved stress to restore the balance. Spalart *et al.* (23) refer to this as “Modeled Stress Depletion”, or MSD. This occurs when the grid is gradually refined starting from Type I, e.g., when the user is seeking grid convergence, or when geometry features demand a fine wall-parallel grid. The regime represented by the Type II grid also occurs when a boundary layer thickens and nears separation.

Figure 2 shows the effect of the adverse interactions of ambiguous grids in DES of the turbulent flow over a flat plate with zero pressure gradient. The Reynolds number of the flow based on the momentum thickness of the boundary layer at the end of the flat plate was approximately 9000 and the flow conditions corresponded to a Mach number of 0.2. The two-dimensional flow was computed on structured grids of different mesh densities using Cobalt (36). The baseline grid consisted of 100×108 points in the streamwise and wall-normal directions respectively and was typical of a Type I grid discussed above. The baseline grid was improved upon by increasing the mesh density in the streamwise direction to yield grids consisting of 300×108 , 500×108 and 700×108 points. Additionally, the wall-normal spacing was altered on one of the grids to yield the finest grid consisting of 500×200 points. The initial wall-normal distance on all of the grids, corresponded to an average y_+ of less than unity.

Figure 2a shows the location of the RANS-LES interface on each of the grids in relation to a RANS boundary layer and RANS eddy viscosity distribution at the edge of the plate. The parameter F_{DES} refers to the ratio of $\min(C_{DES}\Delta, d)$ to d and assumes a value of unity at the interface. The interface is located well within the boundary layer for all of the grids except the baseline grid for which it is approximately at the edge of the boundary layer. This has a marked effect on the coefficient of skin friction, mean velocity, and eddy viscosity ratio which are plotted in Figure 2b,c and d respectively. These plots indicate the effect of the lengthscale switch occurring well within the boundary layer in DES, leading to a drop in the levels of the eddy viscosity and modeled stresses as compared to the RANS levels, thereby altering the growth of the boundary layer and resulting in a poor prediction of the skin friction coefficient.

The issue of MSD exists in any hybrid RANS-LES method such as Limited Numerical Scales (LNS) (43), which also introduces the grid spacing into the turbulence model in order to achieve an LES treatment. It is to be noted that two recently proposed methods, Scale-Adaptive Simulations (SAS) (42) and Turbulence-Resolving RANS (TRRANS) (41) are based purely on RANS models and do not incorporate an explicit dependence of the mesh into the turbulence model though computations performed using these methods exhibit some LES properties (e.g., a range of eddies captured on the grid). However, these methods are not yet completely understood and have not, in

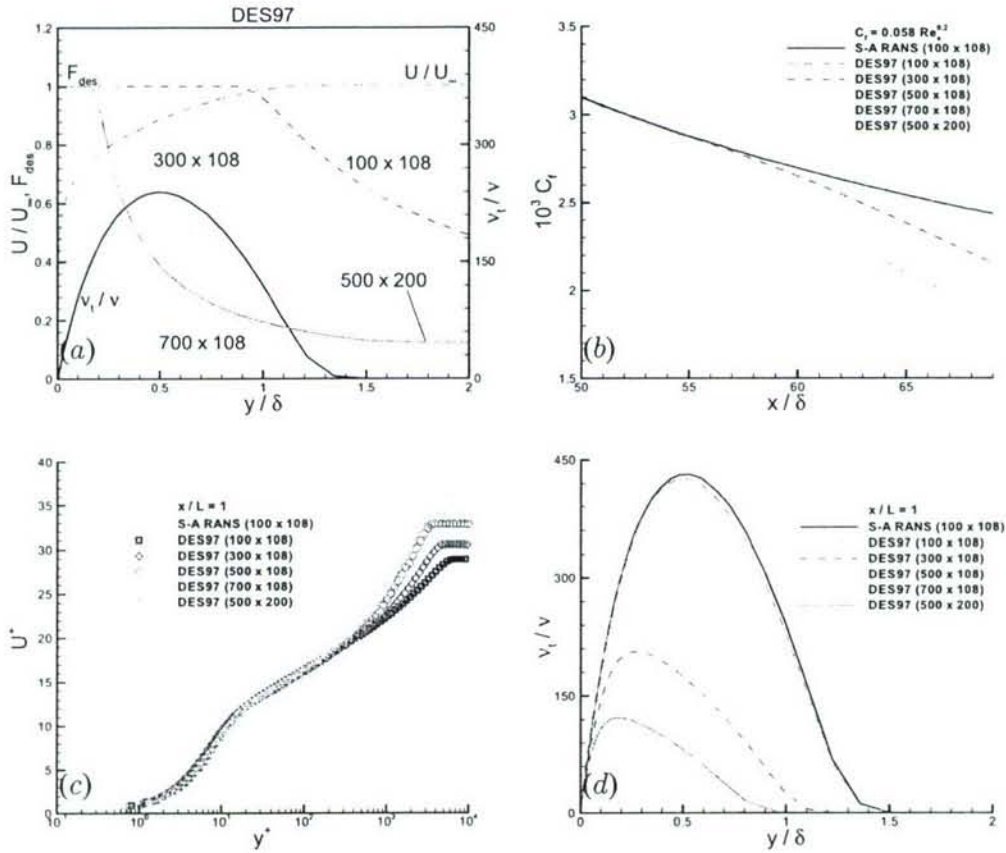


Figure 2: DES97 of a flat plate boundary layer. (a) F_{DES} along with profiles of the RANS velocity profile and eddy viscosity ratio; (b) skin friction coefficient; (c) mean velocity; (d) eddy viscosity ratio.

the case of SAS, been able to produce LES content in channel flow. Similarly, TRRANS fails to sustain unsteadiness over a backward facing step (41). Solutions to MSD have been proposed that make DES “zonal” by disabling the DES limiter in selected regions where an attached boundary layer is expected. This user intervention is adequate in simple geometries though defining such regions in complex, three-dimensional configurations is difficult and could be prone to errors. Other solutions to MSD have attempted to use additional information from the mesh, such as using the aspect ratio of the grid cells in order to dictate the location where the model switches from RANS to LES. Boundary-layer grid cells are characterized by relatively large aspect ratios and in these approaches an aspect ratio much larger than 1 is used to indicate the boundary layer and the length scale \tilde{d} is biased to maintain its RANS value.

A drawback of this approach is that in the case of unstructured grids, there might be abrupt transitions from high-aspect-ratio hexahedral cells near the walls to low-aspect-ratio tetrahedral cells away from the walls. This could in turn lead to relatively abrupt switching between RANS and LES modes and possibly large changes in the DES length scale across such an interface. Conversely, structured grids often have regions with rather fine, high-aspect ratio grid cells outside boundary layers, which in turn further complicates this approach.

Forsythe, Fremaux and Hall (44) implemented a method in which the DES lengthscale, $\min(d, C_{DES}\Delta)$ was modified to extend RANS behavior for most of the boundary layer when thicker boundary layers were encountered. This was done by replacing the DES lengthscale, $\min(d, C_{DES}\Delta)$ by a function that has the same limiting behaviors when $d \ll C_{DES}\Delta$ and when $d \gg C_{DES}\Delta$, but follows d when it is only somewhat larger than $C_{DES}\Delta$. The specific form of the lengthscale switching function was $\tilde{d} \equiv \min(C_{DES}\max(n^2C_{DES}\Delta^2/d, \Delta), d)$ with $n = 3$. The shortcoming of this method is that the use of $d/C_{DES}\Delta$ to identify boundary layers is not significantly robust as compared to the use of cell aspect ratios. It would be difficult for users to anticipate the thickness of the boundary layer at the time of grid generation, especially in flows that are on the verge of separation. Grid-adaption should improve the situation, but the present algorithms produce strong local variations of cell size and aspect ratio. Menter and Kuntz (37) proposed a solution within the framework of DES with the F_1 or F_2 functions of the SST two-equation RANS model employed to delay the switch to LES within the boundary layer. Spalart *et al.* (23) recently presented a newer version of DES based on the S-A RANS model which delays the switch from RANS to LES within the boundary layer. This is discussed in the following section.

2 Delayed Detached Eddy Simulation

The new version of the model, Delayed Detached Eddy Simulation (DDES), modifies the length scale \tilde{d} in order to preserve RANS treatment of the boundary layer irrespective of the grid spacings. Essentially, the spirit of the modification is to utilize information concerning the length scale of the turbulence as predicted by the model, in addition to the wall distance and local grid spacing to determine the location of the interface. To obtain the DDES formulation the parameter r_d is introduced,

$$r_d \equiv \frac{\nu_t + \nu}{\sqrt{U_{i,j}U_{i,j}}\kappa^2 d^2}, \quad (37)$$

where $U_{i,j}$ are the velocity gradients. Similar to r in the S-A model, this parameter equals 1 in a logarithmic layer, and falls to 0 gradually towards the edge of the boundary layer. The addition of ν in the numerator corrects the very-near-wall behavior by ensuring that r_d remains away from 0. The quantity r_d is used as an argument to the function,

$$f_d \equiv 1 - \tanh([Cr_d]^n), \quad (38)$$

which is designed to be 1 in the LES region, where $r_d \ll 1$, and 0 elsewhere (and to be insensitive to r_d exceeding 1 very near the wall). Values of 8 and 3 were selected for C and n based on intuitive shape requirements for f_d , and on tests of DDES in the flat-plate boundary layer (23). The DES length scale \tilde{d} is then re-defined as,

$$\tilde{d} \equiv d - f_d \max(0, d - C_{DES}\Delta). \quad (39)$$

Setting f_d to 0 yields RANS ($\tilde{d} = d$), while setting it to 1 gives DES97. For DES based on most of the possible RANS models, DDES will consist in multiplying by f_d the term that constitutes the difference between RANS and DES.

The two-dimensional flow over a flat plate with zero pressure gradient was computed using DDES with the same flow parameters as those used in the DES study 2. DES97 and DDES predictions of the flow over an Aerospatiale A-airfoil at an angle-of-attack of 13.3° were obtained on different grids to focus on the aspect of grid-dependence of the solutions. These tests also enabled to reinforce the suitability of the model constants (C and n in equation 38) in DDES. Based on the investigations, the mean velocity profiles at locations normal to the airfoil surface are essentially grid-independent in the DDES predictions, contrary to the trend indicated by DES97. Figure 3a shows the distribution of $1 - f_d$ for different values of the coefficients $((10, 4), (8, 2)$ and $(8, 3))$ along with the destruction term in the S-A model for the boundary layer flow over a flat plate. The distribution of $1 - f_d$ for the case with coefficients 8 and 3 indicate the suitability of the chosen values. Figure 3b shows the distribution of $1 - f_d$ for different values of the coefficients $((10, 4), (8, 2)$ and $(8, 3))$ along with the destruction term in the S-A model for the flow over the A-airfoil at $Re = 2 \times 10^6$ and at an angle-of-attack of 13.3° . Figure 3c and d show the variation in the profiles

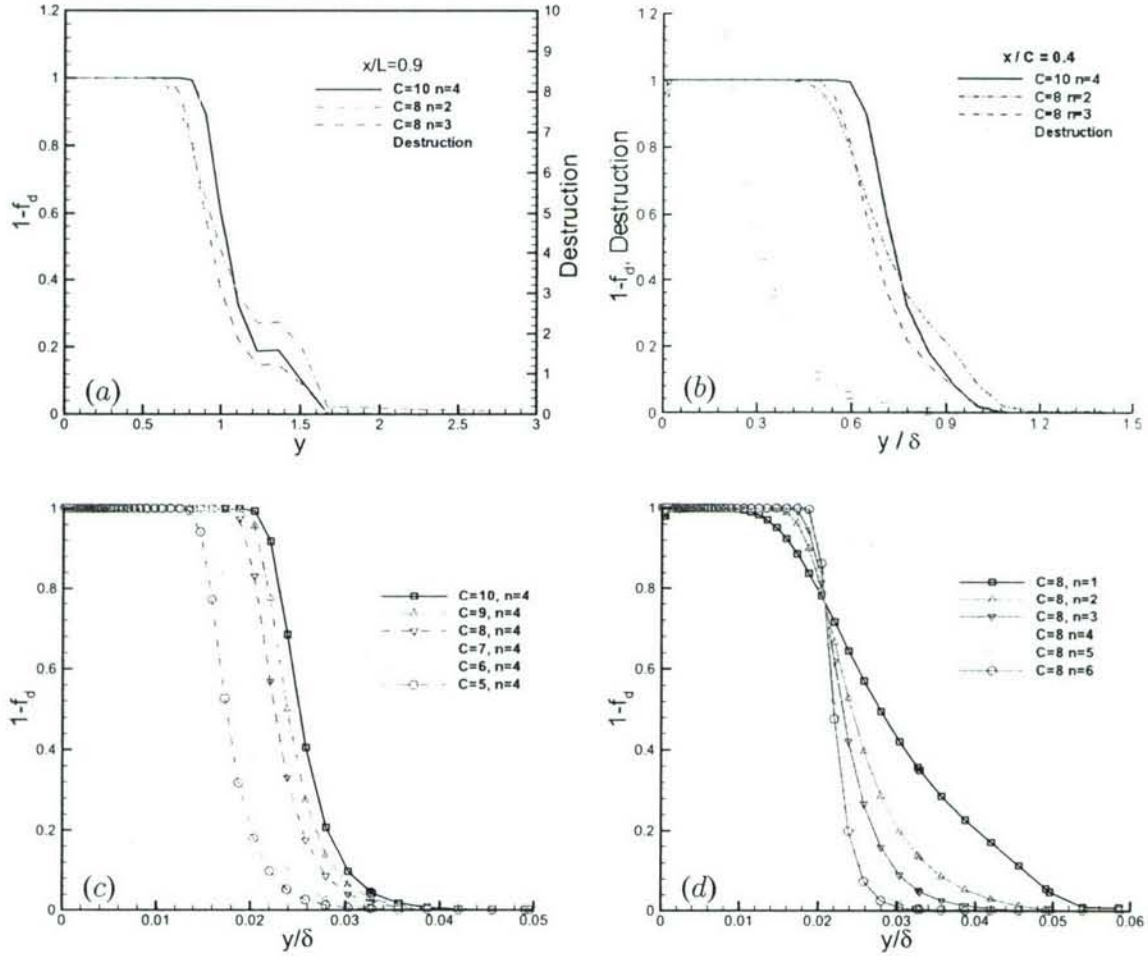


Figure 3: (a) Model parameter $1 - f_d$ along with the destruction term in the S-A model for a flat plate boundary layer; (b) Model parameter $1 - f_d$ along with the destruction term in the S-A model for the flow over an airfoil at $Re = 2 \times 10^6$ at an angle-of-attack of 13.3° ; (c) model parameter $1 - f_d$ from the flow over an airfoil at $Re = 2 \times 10^6$ at an angle of attack of 13.3° with $n = 4$ and C varied; (d) model parameter $1 - f_d$ from the flow over an airfoil at $Re = 2 \times 10^6$ at an angle of attack of 13.3° with $C = 8$ and n varied.

of $1 - f_d$ for various values of C and n for the flow over the A-airfoil at $Re = 2 \times 10^6$ and at an angle-of-attack of 13.3° . A larger value of C ensures that f_d is equal to zero for a longer extent of the boundary layer, while a larger n increases the sharpness of the function, ensuring that f_d quickly changes from 1 to zero at the interface. Figure 4a and b show contours of the model parameter $1 - f_d$ for the flow over a cylinder at $Re = 8 \times 10^6$ with $C = 8$ and $n = 2$ and 3. It can be seen from the contour plot that with $C = 8$ and $n = 2$, the transition region where f_d changes from 0 to 1 is wider as compared to the case with $C = 8$ and $n = 3$. Figure 4c and d show the same effect when n is varied for the flow over the A-airfoil at $Re = 2 \times 10^6$ and at an angle-of-attack of 13.3° .

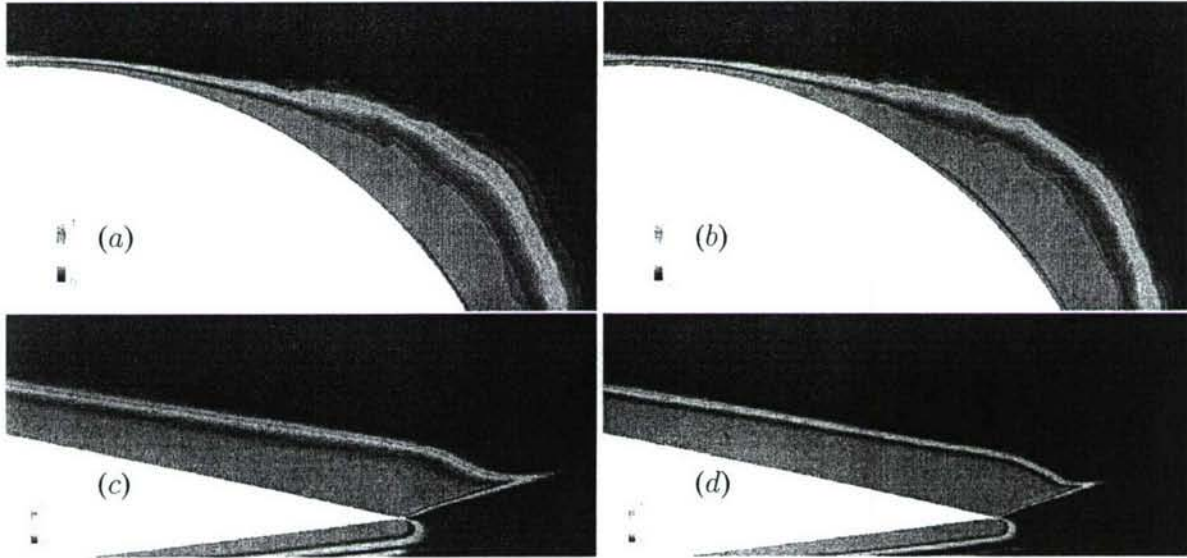


Figure 4: Contours of the model parameter $1 - f_d$ from the flow over a cylinder at $Re = 8 \times 10^6$: (a) $C = 8, n = 2$; (b) $C = 8, n = 3$; Contours of the model parameter $1 - f_d$ from the flow over an airfoil at $Re = 2 \times 10^6$ at an angle of attack of 13° : (c) $C = 8, n = 2$; (d) $C = 8, n = 3$.

Figure 5 shows distributions of the skin friction coefficient and the mean velocity at the end of the plate. The results show grid independence and compare well with the RANS on all the grids except for the 700×108 grid for which there is only a slight mismatch with the RANS. Figure 6 shows profiles of the parameters F_{DES} and $1 - f_d$ in relation to a RANS boundary layer streamwise velocity and RANS eddy viscosity distribution at the end of the flat plate. The parameter F_{DES} is the ratio of the turbulent length scale in DDES to the wall distance(d).

3 Flow over a Circular Cylinder using DDES

An application of DDES to the flow over a circular cylinder provides an opportunity to assess the new method in a flow for which DES97 is a very powerful and accurate approach. While

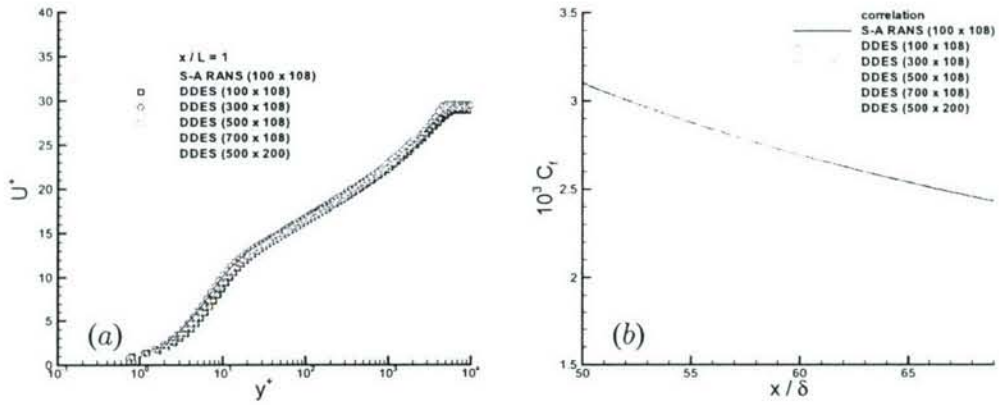


Figure 5: DDES of a flat plate boundary layer. (a) mean velocity; (b) skin friction coefficient.

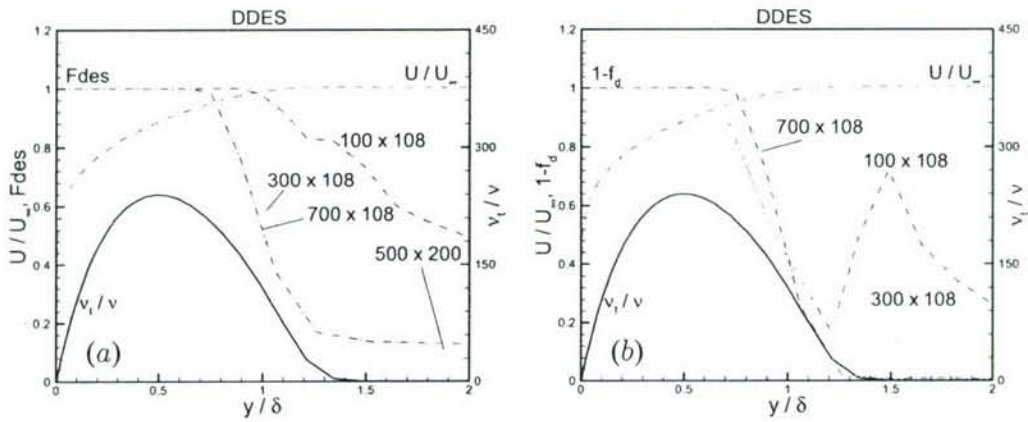


Figure 6: Turbulent model properties along with RANS mean streamwise velocity and eddy viscosity ratio. (a) F_{DES} ; (b) $1 - f_d$.

the cylinder is not a candidate that should be prone to MSD (boundary layers prior to separation are thin and mesh spacings on typical grids will not locate the RANS-LES interface within the boundary layer), predictions should not be degraded using DDES compared to those using DES97.

Computations are presented at a Reynolds number based on the freestream velocity and cylinder diameter D of 1.4×10^5 and 8×10^6 . The lower Re predictions are assessed against previous simulations while experimental measurements were used to evaluate the higher Re predictions. For $Re = 1.4 \times 10^5$, the DES predictions obtained by Travin *et al.* (57) and Hansen and Forsythe (28) were available for assessment and comparison. Mesh refinement was investigated at a higher Reynolds number, $Re = 8 \times 10^6$, the results of which were compared with experimental measurements (70), (71). The compressible Navier-Stokes equations were solved on unstructured grids using *Cobalt*. The spanwise coordinate of the domain along which periodic boundary conditions were applied was $4D$ for both Reynolds numbers. The calculations at $Re = 1.4 \times 10^5$ were performed using a mesh that consisted of 1.434×10^6 cells (the same grid as that used by Hansen and Forsythe (28)) and characterized by a spanwise grid spacing of $\Delta_z/D = 0.10$. The calculations at $Re = 1.4 \times 10^5$ were used to provide an initial assessment of DDES against DES97 results. The influence of mesh refinement was investigated at the higher Reynolds number using three grids having 1.46×10^6 , 3.71×10^6 , and 9.83×10^6 cells and are referred to as “coarse grid” or “cg”, “medium grid” or “mg”, and “fine grid” or “fg”. The medium grid was created by refining in all directions the coarse mesh by a factor of $\sqrt{2}$. The finer grid had another factor of $\sqrt{2}$ refinement in each coordinate direction. The corresponding spanwise grid spacings, which determined Δ in DES97, were $\Delta_z/D = 0.10$, $\Delta_z/D = 0.071$, and $\Delta_z/D = 0.05$ for the coarse, medium, and fine grids, respectively. Figures 7a and b show the cross-sections of the mesh in the vicinity of the cylinder. The grid was created using VGRIDns (55) and is comprised of prisms near the cylinder surface and tetrahedra away from the wall. For all of the grids, the initial wall normal distance was within one viscous unit on average and a stretching rate of 1.2 was applied to the wall-normal grid within the boundary layer. The domain extended approximately 20 cylinder diameters from the cylinder surface. For both Reynolds numbers, the super-critical flow is approximated by computing fully-turbulent solutions. At the inlet of the computational domain a small level of eddy viscosity (corresponding to $\chi = 3$) is prescribed that is sufficient to ignite the turbulence model as the fluid enters the boundary layers. For all of the simulations reported here, the time step was fixed at $0.01D/U_\infty$ where U_∞ is the freestream velocity.

3.1 Predictions at $Re = 1.4 \times 10^5$

Shown in table 1 are averaged quantities from DES97 and DDES predictions of the flow at $Re = 1.4 \times 10^5$: the drag coefficient C_d , rms lift coefficient $C_{l,rms}$, shedding Strouhal number St , base pressure coefficient C_p and separation angle θ_{sep} . Also included are the DES97 predictions of Travin *et al.* (57) and Hansen and Forsythe (28) along with the experimental measurements

reported in Roshko (70). The spanwise grid spacing for the current computations and those of Hansen and Forsythe (28) is 10 nodes per cylinder diameter while the structured mesh for the fully-turbulent solution summarized in the table from Travin *et al.* (57) employed a spanwise resolution of 15 grid points per diameter. In general, the table shows that there is good agreement between the present DES97 and DDES predictions and the corresponding results from Travin *et al.* (57) and Hansen and Forsythe (28). The drag coefficient C_d from all of the simulations is on the low end of the measurements summarized by Roshko (70), that correspond to a higher Reynolds number range ($3.5 \times 10^6 < Re < 8.4 \times 10^6$). Table 1 also shows that the back pressure is slightly more negative for the DDES which is not inconsistent with the slightly higher rms lift that is predicted compared to the DES97 results (and also Travin *et al.* (57), which have the same rms lift as in the current DES97). An additional contributor to the differences in table 1 is the difference in sampling periods.

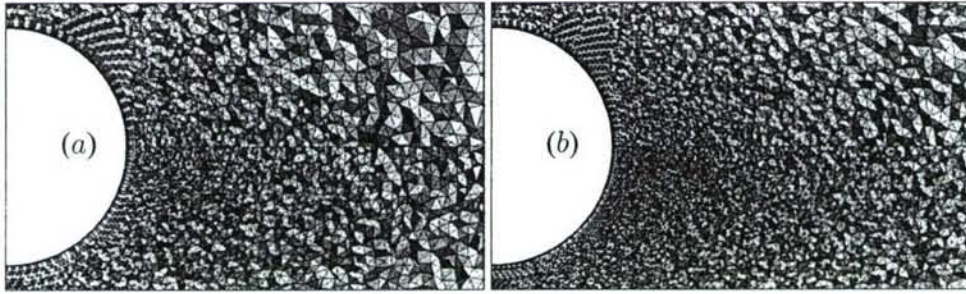


Figure 7: Cross-section of the grids in the vicinity of the cylinder. (a) coarse (upper half plane) and medium (lower half plane) grids; (b) medium (upper half plane) and fine (lower half plane).

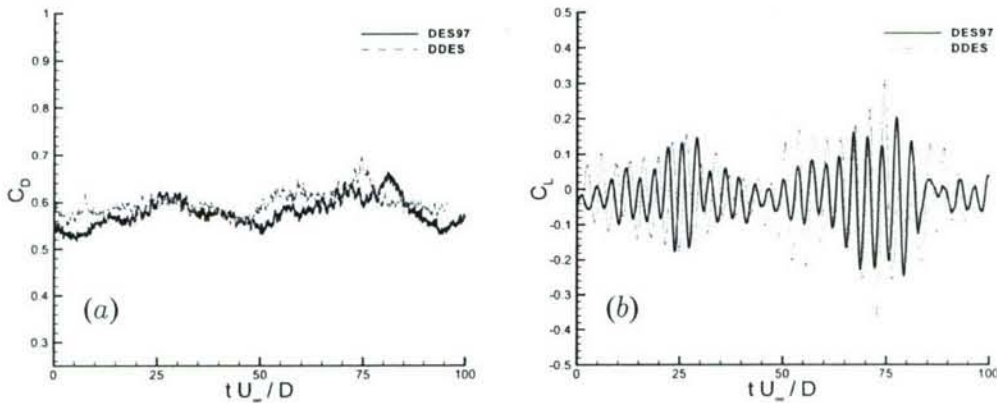


Figure 8: Time history of the drag (in a) and lift (in b) force coefficients, $Re = 1.4 \times 10^5$.

Time histories of the drag and lift coefficients for each model are plotted in Figure 8a and b, respectively. Each figure shows comparable behavior for the two models, including the significant

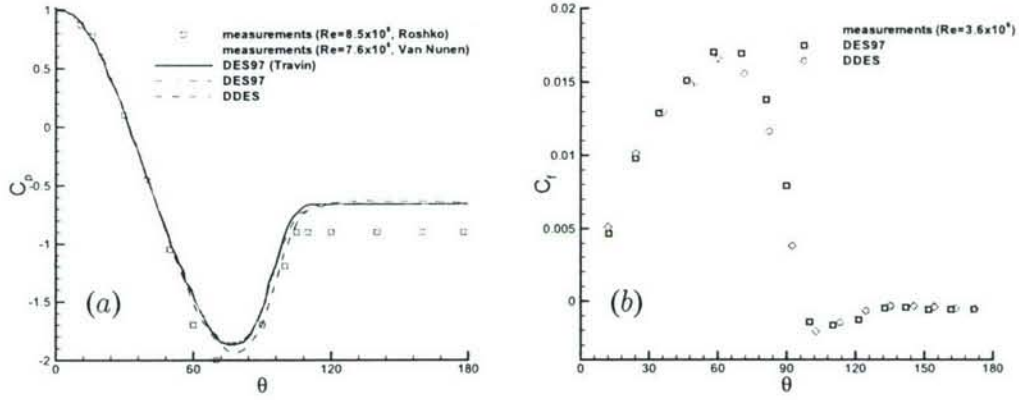


Figure 9: Coefficient of pressure and skin friction coefficient on the cylinder surface, $Re = 1.4 \times 10^5$.

	C_d	$C_{l,rms}$	St	$-C_{pb}$	θ_{sep}
DES97	0.58	0.08	0.29	0.64	98°
DDES	0.60	0.11	0.28	0.69	99°
Travin <i>et al.</i>	0.57	0.08	0.30	0.65	99°
Hansen <i>et al.</i>	0.59	-	0.29	0.72	-
Roshko	0.62-0.74	-	0.27	-	-

Table 1: Lift and Drag co-efficients for the cylinder computations at $Re = 1.4 \times 10^5$

modulation in the lift force as also reported in Travin *et al.* (57) and Hansen and Forsythe (28). These modulations require very long sample periods for convergent statistics, probably longer than those shown in figure 8, which again contributes to the differences in statistics summarized in table 1.

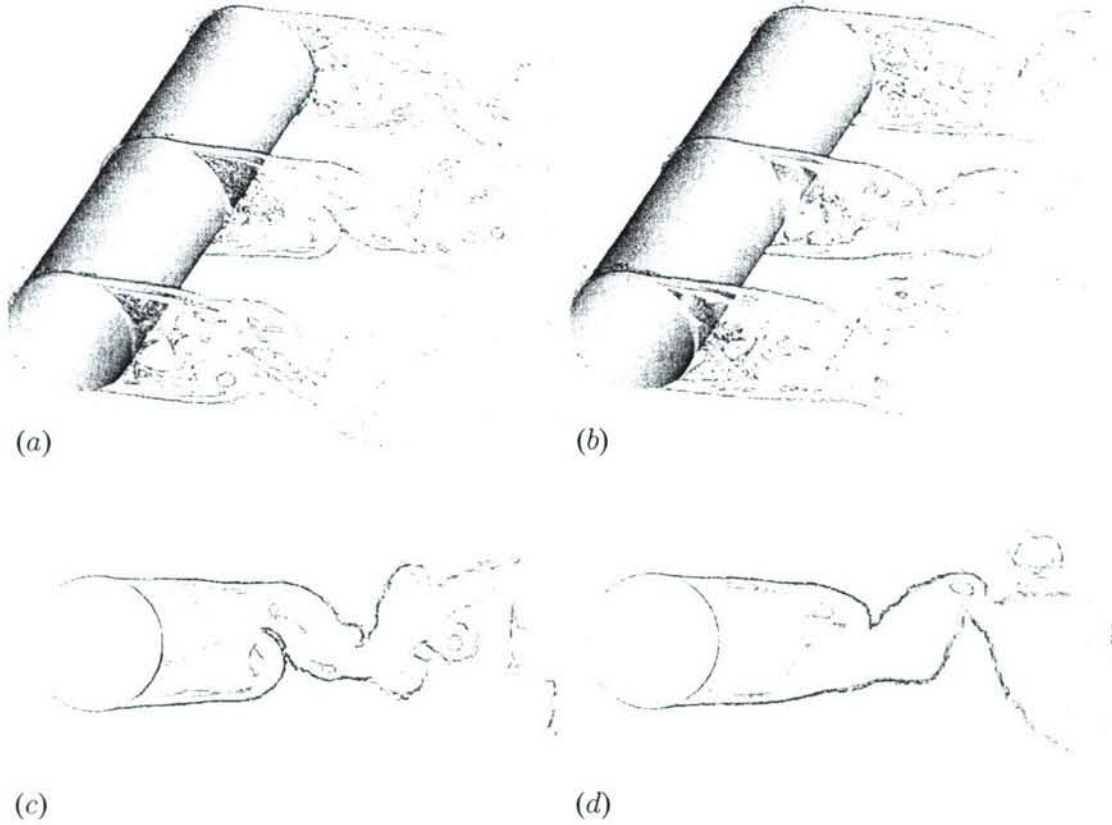


Figure 10: Contours of the instantaneous vorticity from the fine-grid solutions, $Re = 8 \times 10^6$, (a) DES97, (b) DDES; Contours of the instantaneous eddy viscosity ratio from the fine-grid solutions, $Re = 8 \times 10^6$, (c) DES97 (d) DDES.

Figure 9 shows good agreement of the pressure coefficient from the two models along with the results of Travin *et al.* (57) and experimental measurements from Roshko (70) and van Nunen (71). The experiments were performed at a higher Reynolds number (8.4×10^6 in Roshko (70) and 7.6×10^6 in van Nunen (71)) than the computations. However, the fully turbulent treatment of the flow can be considered a model of the high Reynolds number experiment so long as transition occurs far upstream of separation. The C_f plot indicates that the simulation results are far from the measurements prior to separation. While the simulations are of a fully turbulent boundary layer prior to separation, the experiments indicate the boundary layer was laminar even close to the separation line.

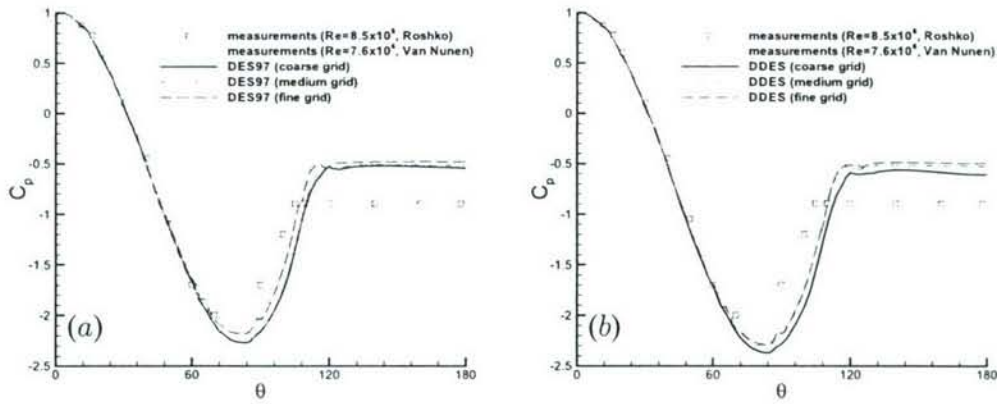


Figure 11: Coefficient of pressure on the cylinder surface, $Re = 8 \times 10^6$, (a) DES97, (b) DDES

3.2 Predictions at $Re = 8 \times 10^6$

Contours of the instantaneous vorticity magnitude in three planes along the span of the cylinder are shown in Figure 10. The visualizations shown in the figure are from the fine grid DES97 and DDES predictions. Characteristic of a natural DES application in a flow experiencing massive separation, the figure shows that the eddy content in the wake develops rapidly following boundary layer detachment. Contours of the instantaneous eddy viscosity ratio, ν_t/ν in a single spanwise plane of the cylinder are also shown in Figure 10. Both DES97 and DDES show similar levels of eddy viscosity in the wake.

The pressure coefficient for both models and each grid is compared to the experimental measurements of Roshko and van Nunen in Figure 11. Comparison of the frames shows that the models predict similar pressure distributions, consistent with the close agreement observed in the drag coefficient. The figure shows the pressure recovery in the aft region for both DES models is in closer agreement to the measurements of van Nunen and that the computations exhibit a lower minimum in the vicinity of 90 degrees than measured in either experiment.

Time histories of the drag and lift force coefficients on all three grids, averaged over the spanwise dimension, are shown in Figure 12. The histories shown in the figure were subsequently averaged over 80 time units to obtain the values summarized in table 2. The lift coefficient exhibits very large modulations on the coarse grid, which are not observed on the finer meshes. The large modulations on the coarse grid are indicative of very weak three-dimensionality due to inadequate resolution. The lift flatness factor, which provides a measure of the irregularity of the signal with respect to the mean (larger excursions from the mean imply a larger lift flatness factor) is 2.21, 2.16 and 2.04 for the coarse, medium, and fine grids, respectively. These values are in reasonable agreement with the value of 2.1 reported by Travin *et al.* (57) in DES of the flow around a cylinder at $Re = 3 \times 10^6$.

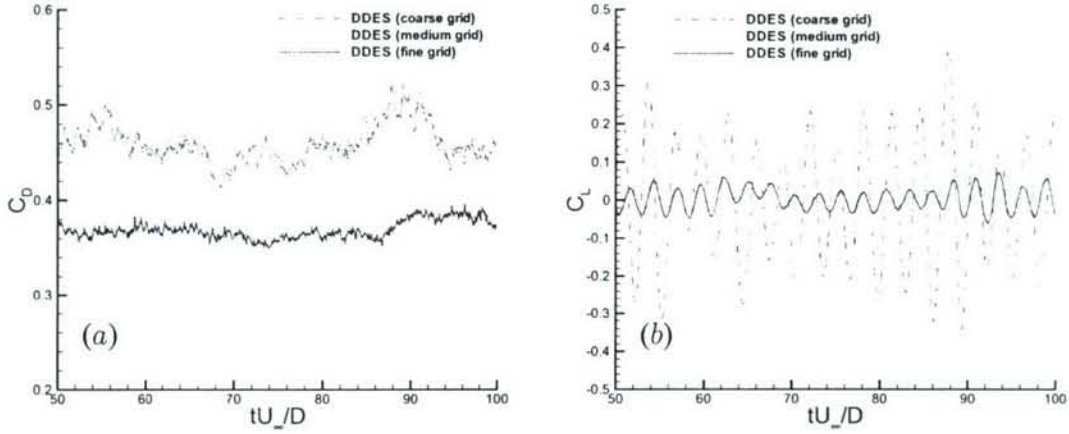


Figure 12: Time histories of the drag and lift coefficients for DDES of the cylinder, $Re = 8 \times 10^6$.

The averaged drag coefficient, shedding Strouhal number, and separation angle for each of the grids and both DES97 and DDES models are summarized in Table 2. With the exception of the DDES prediction using the coarsest grid, the averaged properties predicted by the two models are in quite good agreement. In general, the drag coefficient is around 0.4, which agrees well with the value of 0.41 reported in Travin *et al.* (57) from DES97 predictions at $Re = 3 \times 10^6$. And with the exception of the coarsest grid, the shedding Strouhal numbers are 0.36 – 0.37, also close to the value of 0.35 in Travin *et al.* (57), again at $Re = 3 \times 10^6$. The table also shows that on the finer meshes, boundary layer separation occurs at 114° , slightly more aft than the value of 111° in the fully turbulent DES97 prediction at $Re = 3 \times 10^6$.

DES97	C_d	St	θ_{sep}
Coarse grid	0.43	0.34	114°
Medium grid	0.40	0.36	114°
Fine grid	0.37	0.37	114°
DDES	C_d	St	θ_{sep}
Coarse grid	0.46	0.33	115°
Medium grid	0.40	0.37	114°
Fine grid	0.38	0.37	114°

Table 2: Drag co-efficient, Strouhal number and angle of separation for the cylinder computations at $Re = 8 \times 10^6$

Figure 13 shows the skin friction coefficient over the surface of the cylinder for the DDES cases. The skin friction predictions in all cases show good agreement with each other but are far above the simulation results of Travin *et al.* (57) at $Re = 3 \times 10^6$. Figure 13 also shows the streamwise velocity distribution in the wake of the cylinder with a crinkle-cut view of the grid. For

a dimensionless time step of 0.01, the figure shows CFL numbers of $O(1)$ at different locations in the wake of the cylinder.

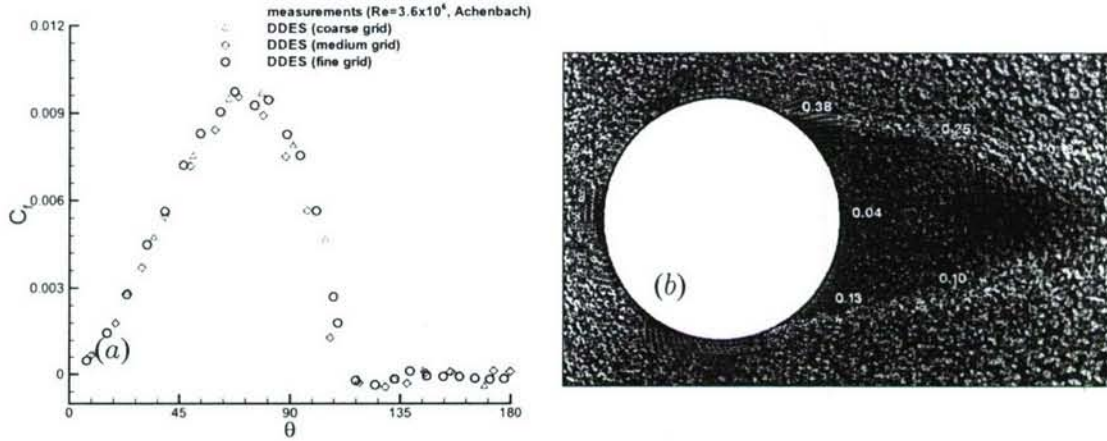


Figure 13: Time histories of the drag and lift coefficients for DDES of the cylinder, $Re = 8 \times 10^6$.

Properties of the turbulence model are shown in Figure 14. Plotted in figure 14(a) and (b) are radial profiles of the mean velocity, eddy viscosity ratio, and \bar{d}/d at $\theta = 75^\circ$ and $\theta = 90^\circ$. The quantities shown in the figure are DDES predictions for each of the grids. Note that the mean velocities are averaged, the profiles of the eddy viscosity and \bar{d}/d are not averaged. Though not shown here, the results from the DES97 cases are virtually identical. For both locations, Figures 14(a) and (b) show that the RANS-LES interface (the location where \bar{d} becomes less than d) moves closer to the wall as the grid is refined, though for this natural application - thin boundary layers into a region of massive separation - the interface remains well outside of the boundary layer. Figures 14(c) and (d) show the radial profiles of the mean velocity, eddy viscosity ratio, and $1 - f_d$ which is designed to go to zero in a region where LES behavior is desired. When massive separation occurs, f_d quickly rises from zero very close to the wall enabling the growth of instabilities in the LES region. Figure 14(e) and (f) show the distribution of r_d along with the radial mean velocity profiles and eddy viscosity profiles. The behavior of r_d is based upon the behavior of f_d , quickly dropping to zero well-within the boundary layer for all three grids.

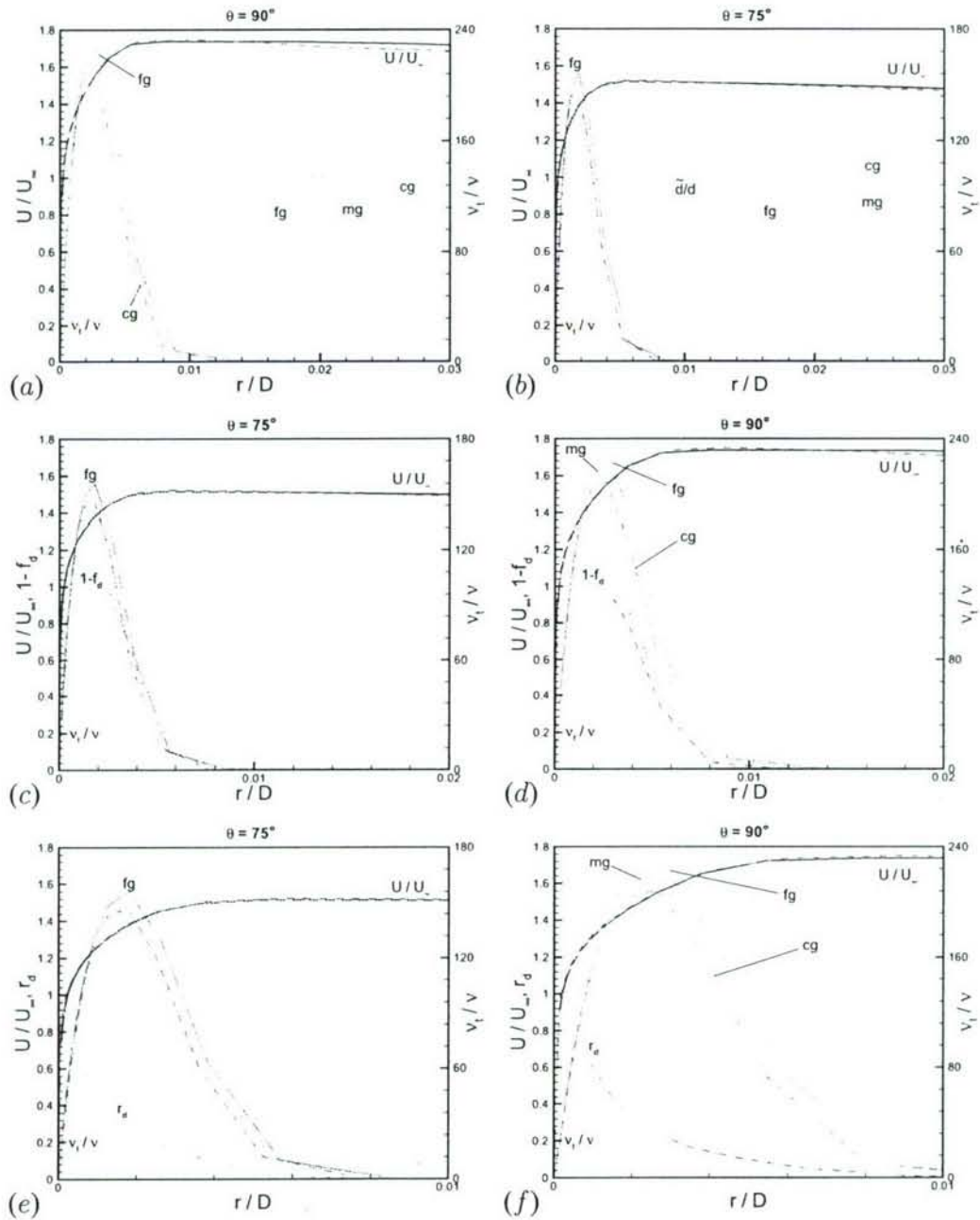


Figure 14: Turbulence model properties: \bar{d}/d , (a) $\theta = 75^\circ$, (b) $\theta = 90^\circ$; Turbulence model properties: $1 - f_d$, (c) $\theta = 75^\circ$, (d) $\theta = 90^\circ$; Turbulence model properties: r_d , (e) $\theta = 75^\circ$, (f) $\theta = 90^\circ$

4 Flow over the Aerospatiale A-airfoil

The predictions of the flow around the Aerospatiale A-airfoil at a chord-based Reynolds number of 2×10^6 are presented in this manuscript. The flow at an angle-of-attack of $\alpha = 13.3^\circ$ is the major focus of the investigation, with a few predictions of the flow at angles-of-attack $\alpha = 7.2^\circ$ and $\alpha = 12.2^\circ$ also included.

4.1 Predictions at $\alpha = 13.3^\circ$

The RANS predictions of the two-dimensional flow were computed using the Spalart-Allmaras (S-A) (with and without rotation correction) and Shear Stress Transport (SST) turbulence models. Solutions of the fully-turbulent flow were computed using both RANS models in addition to prediction of the flow with laminar separation near the leading edge using the triplex approach within the Spalart-Allmaras model. For the triplex case, transition from laminar-to-turbulent flow along the lower (pressure) surface was fixed by tripping the boundary layer at $x/C = 0.3$. The pressure coefficient in the RANS solutions are in reasonable agreement with measurements prior to trailing edge separation. The triplex solution cases using the Spalart-Allmaras model predict laminar separation close to $x/C = 0.10$ with turbulent reattachment close to $x/C = 0.12$ and followed by separation of the turbulent boundary layer near the trailing edge close to $x/C = 0.90$. Trailing edge separation in the fully turbulent solutions is invariably closer to the experimental value of $x/C = 0.83$. Comparison of the mean velocity predictions to measurements shows a behavior consistent with the mismatch in separation location compared to measurements in the triplex cases. The rotation-correction does not improve the results appreciably and produces similar results as the case without the correction. DES97 and DDES predictions were obtained on different grids to focus on the aspect of grid-dependence of the solutions. Based on the investigations, the mean velocity profiles at locations normal to the airfoil surface are essentially grid-independent in the DDES predictions, contrary to the trend indicated by DES97.

4.2 Approach

The flow over the Aerospatiale A-airfoil at an angle-of-attack of 13.3° and at a chord-based Reynolds number of 2.1×10^6 was studied in great detail through the LESFOIL project (31). The main advantage of using LES for such a case include the reduced sensitivity to modeling errors occurring in RANS methods and the use of grid refinement to obtain richer flow physics. One of the major findings of the LESFOIL project (31) is that even a narrow section of the airfoil (at a moderately high Reynolds number and unswept), poses an extreme challenge to LES in terms of computational cost. It was also noted that other aspects such as the numerical method, grid generation and mesh resolution requirements, especially in the near-wall region, coupled with considerations of the spanwise period in three-dimensional eddy-resolving computations stress the

capabilities of any simulation strategy. The general characteristics of this flow are illustrated in

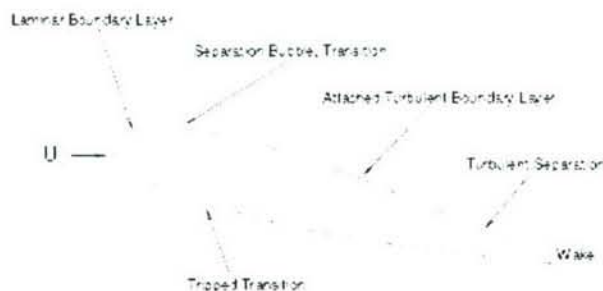


Figure 15: Flow regimes on the Aerospatiale A-airfoil (31)

figure 15. As the flow moves along the upper (suction) surface of the airfoil, the laminar boundary layer experiences a free transition in a small laminar separation bubble with turbulent reattachment at around $x/C = 0.12$. The turbulent boundary layer grows along the suction surface of the airfoil, separating at about $x/C = 0.83$, resulting in a shallow separation bubble that extends to the trailing edge. Measurements indicate a reverse-flow region extending to roughly a wall-normal location $y/C = 0.016$ where y defines the coordinate normal to the suction surface and that the location of maximum reverse flow occurs at $y/C = 0.003$. Along the lower (pressure) surface of the airfoil, the boundary layer was tripped at $x/C = 0.3$, enabling transition from laminar-to-turbulent flow. The measurements acquired included the airfoil lift and drag, skin friction, pressure distributions as well as the mean velocity and Reynolds stress profiles at several stations along the airfoil and in the near-wake (29), (30).

4.2.1 Flow solver and grids

The compressible Navier-Stokes equations are solved on unstructured grids using *Cobalt*. The numerical method used consists of a cell-centered finite volume approach applicable to arbitrary cell topologies (36). The spatial operator uses the exact Riemann solver of Gottleib and Groth (60), least-squares gradient calculations using QR factorization to provide second order accuracy in space, and TVD flux limiters to limit extremes at cell faces. A point implicit method using analytic first-order inviscid and viscous Jacobians is used for advancement of the discretized system. For time-accurate computations, a Newton sub-iteration scheme is employed, the method is second-order accurate in time. The domain decomposition library ParMETIS (73) is used for parallel implementation and provides optimal load balancing with a minimal surface interface between zones. Communication between processors is achieved using Message Passing Interface. The working of the solver has been explained in greater detail in the Appendix section.

The grids used in the study were structured and C-type grids, generated using Gridgen (32). The grids are referenced as 'coarse grid 1', 'coarse grid 2', 'medium grid' and 'fine grid' in table 3. For 'coarse grid 1', the ratio of cell size in the streamwise direction to the RANS boundary layer thickness at $x/C = 0.5$ is approximately 0.68, for the 'fine grid', the corresponding value is approximately 0.61. These values serve as average measures of the grid density, indicating the absence of a marked difference between 'coarse grid 1' and 'fine grid'. It must be noted that 'coarse grid 2' was formed by extruding 'coarse grid 1' in the spanwise direction with $\Delta_z = 0.005$ and a spanwise extent of 0.01, a fictitious value that does not have a marked effect on altering the location of the RANS-LES interface in DES97. Figure 16 shows 'coarse grid 1' close to the surface of the airfoil and the spanwise extent of 'coarse grid 2'.

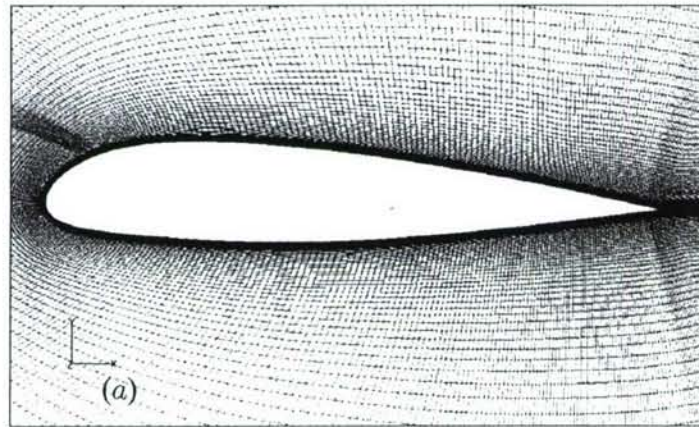


Figure 16: (a) Coarse grid 1; (b) Spanwise extent of coarse grid 2

grid	2D/3D	Δ_z	number of cells
coarse grid 1	2D	-	76,000
coarse grid 2	3D	0.005	$76,000 \times 2$
medium grid	2D	-	85,000
fine grid	2D	-	98,000

Table 3: Grid sizes used to study the flow over the Aerospatiale A-airfoil at an angle-of-attack of 13.3° and at a chord-based Reynolds number of 2.1×10^6

4.2.2 Results

Measurements show that the flow over the Aerospatiale A-airfoil experiences a laminar separation in the vicinity of the leading edge region, just downstream of the peak negative pressure along the suction side. Transition occurs in the separated shear layer with the reattached turbulent boundary layer evolving further along the suction side prior to a subsequent separation near the trailing edge. The laminar separation and transition is accounted for using the tripless approach outlined by Travin (57). The tripless approach provides a means to accommodate the laminar separation and transition in the separated shear layer, in the present calculations represented by an activation of the turbulence model. The eddy viscosity upstream of the airfoil is zero, non-zero values are seeded into the suction side of the airfoil using a boundary layer trip.

4.2.3 Tripless and Fully Turbulent solutions

The suction side trip was location was varied to be at $x/C = 0.08$, $x/C = 0.12$, $x/C = 0.13$ or $x/C = 0.20$. A second boundary layer trip is located at $x/C = 0.3$ along the pressure surface, the same location as used in the experiments. Predictions of the fully-turbulent flow are also obtained using the S-A and SST turbulence models. The fully turbulent solutions are computed by seeding a small level of eddy viscosity into the upstream flow, sufficient to ignite the turbulence model as the fluid enters the boundary layers. The initial (laminar) separation near the leading edge does not occur in the fully turbulent solutions. Other aspects such as the results close to the trailing edge of the airfoil are also different in the fully-turbulent solutions as compared to the tripless solutions. In the tripless runs, there is laminar separation followed by turbulent reattachment close to $x/C = 0.10$. A second separation is predicted near the trailing edge of the airfoil. The RANS separation locations are shown in table 4. The separation locations in the fully turbulent runs are closer to the experimental value of $x/C = 0.83$. Among the fully turbulent runs, the SST model predicts a value of 0.82, closest to the experimental results, while S-A and S-A RC models predict earlier separation (at $x/C = 0.79$ and $x/C = 0.77$ respectively).

While the fully turbulent runs predict the location of turbulent separation to be close to the experimental value of $x/C = 0.83$, they fail to shed light on the laminar separation that occurs

grid	RANS model	Top Trip (x/C)	Transition (x/C)	Turbulent Separation (x/C)
medium grid	S-A FT	-	-	0.79
	S-A RC FT	-	-	0.77
	SST FT	-	-	0.82
	S-A tripless	0.2	0.106-0.118	0.91
	S-A RC tripless	0.2	0.102-0.118	0.89
fine grid	S-A FT	-	-	0.79
	S-A RC FT	-	-	0.77
	SST FT	-	-	0.82
	S-A tripless	0.2	0.093-0.128	0.91
	S-A RC tripless	0.2	0.102-0.118	0.90
	S-A tripless	0.08	-	0.88
	S-A tripless	0.13	0.10-0.125	0.91
	S-A tripless	0.12	-	0.91
coarse grid 1	S-A tripless	0.08	-	0.89

Table 4: Summary of the RANS computations for $\alpha = 13.3^\circ$

on the forward part of the suction surface, motivating the need to employ trips on the suction surface. Preliminary investigations involved the placement of the top trip at a location corresponding to $x/C = 0.2$. In these cases, during the initial stages of the simulations, the eddy viscosity drifted upstream from the location of the trip, inducing transition at a location approximately corresponding to $x/C = 0.11$. More runs were conducted with the location of the top trip changed to $x/C = 0.13$, $x/C = 0.12$ and $x/C = 0.08$. Application of the top trip at $x/C = 0.13$ gave a similar transition location, with no laminar separation bubble present when the top trip was located at $x/C = 0.12$ and $x/C = 0.08$. The main shortcoming of the tripless runs is that they predict a location of turbulent separation further downstream of the experiment and of the fully turbulent runs. The separation locations obtained using DES97 and DDES are compared with S-A RANS predictions in table 5, with the location of the top trip fixed at $x/C = 0.08$. The DES97 predictions show a large variation in the results using the fine grid and either of the coarse grids. The results obtained with ‘coarse grid 1’ and ‘coarse grid 2’ hardly show any variation indicating that the spanwise extent of ‘coarse grid 2’ hardly changes the location of the RANS-LES interface, the location of which alters the separation point. The DDES predictions on all grids are in good agreement among themselves and very close to the S-A RANS results.

The pressure coefficient over the airfoil on both the pressure and suction sides using RANS is shown in figure 17. The figures show that compared to the experimental measurements, the overall pressure distribution is adequately captured by both fully turbulent solutions over the pressure side and for the suction side downstream of the region strongly influenced by laminar-to-turbulent transition at the leading edge ($x/C < 0.13$). The tripless S-A results yield a larger peak pressure

grid	RANS model	Top Trip (x/C)	Transition (x/C)	Turbulent Separation (x/C)
fine grid	S-A tripless	0.08	-	0.88
	DES97	0.08	-	0.75
	DDES	0.08	-	0.86
coarse grid 1	S-A tripless	0.08	-	0.89
	DES97	0.08	-	0.83
	DDES	0.08	-	0.87
coarse grid 2	DES97	0.08	-	0.82
	DDES	0.08	-	0.87

Table 5: Comparison of S-A RANS, DES97 and DDES for $\alpha = 13.3^\circ$

near the leading edge of the suction side as shown in figure 17c as compared to the fully turbulent runs. The larger peak suction is similar to the behavior observed in the previous computations which also showed larger suction pressures in predictions with delayed trailing edge separation, a result attributed to changes in the airfoil circulation (31). A notable difference between the fully turbulent and tripless predictions is apparent for the suction-side pressure distribution near the airfoil leading edge. In the vicinity of $x/C = 0.1$, the tripless prediction results (cases with the top trip at $x/C = 0.2$ and $x/C = 0.13$), show a slight plateau in the pressure distribution, a result of the laminar separation bubble captured in this calculation, not captured in the fully turbulent runs. Previous LES calculations of the flow were also able to resolve the laminar separation, in addition to details of the transition process, though at a substantially increased cost (33).

The DES97 and DDES pressure coefficients are compared with the S-A RANS tripless results in figure 18. The DDES results on different grids match relatively well with the S-A RANS tripless results. While DES97 results on ‘coarse grid 1’ and ‘coarse grid 2’ seem to be closer to S-A RANS, the DES97 run on the fine grid produces a lower peak pressure on the suction side of the airfoil.

4.2.4 Skin friction coefficient

Figure 19 shows the skin friction coefficient over the suction side of the airfoil for the RANS cases. The skin friction coefficient over the suction side of the airfoil show that the fully turbulent calculations yield similar predictions of the skin friction, both S-A and SST in reasonable agreement with measurements for chordwise stations past $x/C = 0.4$. The tripless S-A results predict a laminar boundary layer prior to separation and yields a substantially lower C_f compared to the fully turbulent runs upstream of $x/C = 0.1$. The negative region in C_f near $x/C = 0.1$ identifies the separation point and length of the reverse-flow region. For the case in which the top trip is located at $x/C = 0.08$, despite the drop in C_f , the flow does not separate in this region. Following reattachment, the skin friction in the tripless solution sharply increases to values slightly higher than in the fully turbulent predictions. The trailing edge results show a better agreement between the fully

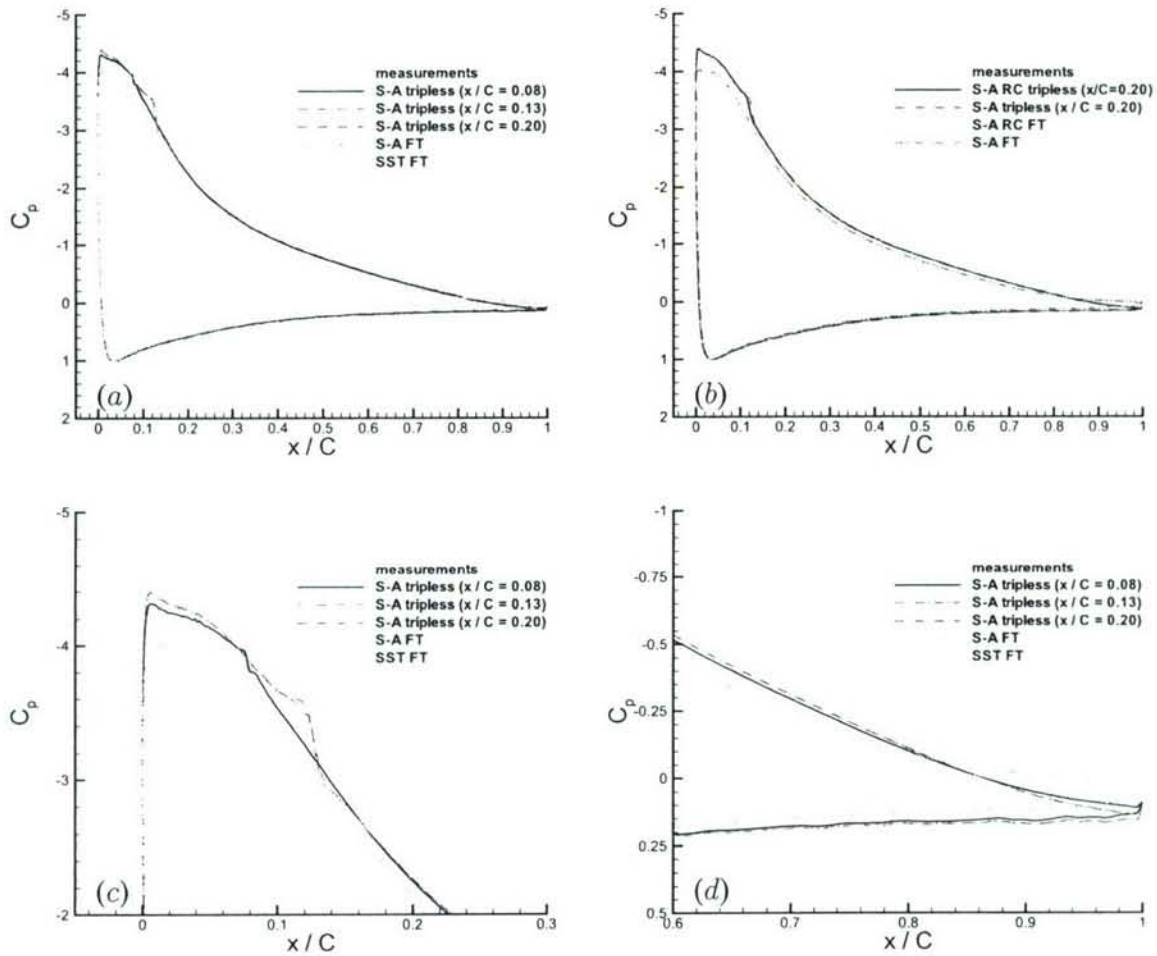


Figure 17: (a) Pressure coefficient predictions comparing tripless and fully turbulent results; (b) Comparison of pressure coefficient predictions using S-A and S-A RC models; (c) Zoomed view of the pressure coefficient at the leading edge region; (d) Zoomed view of the pressure coefficient at the trailing edge region

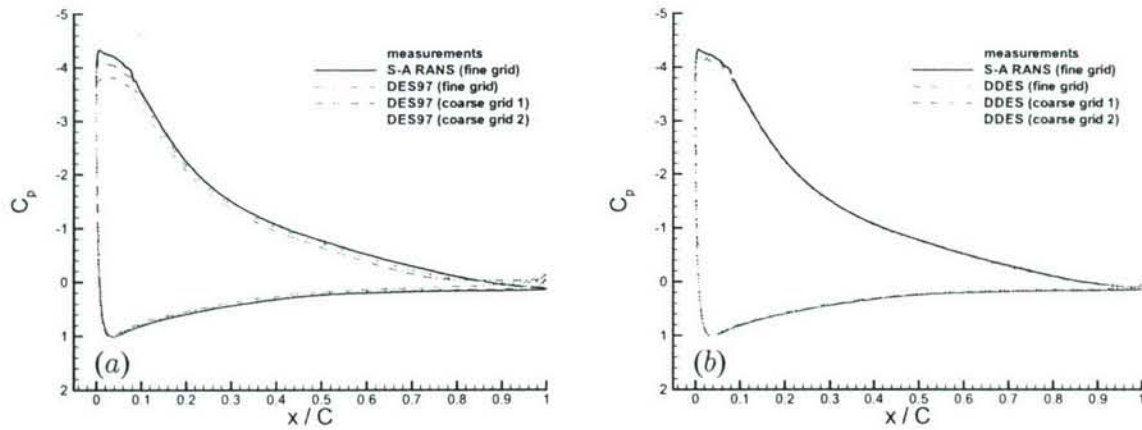


Figure 18: Pressure coefficient: (a) Comparison of S-A RANS and DES97; (b) Comparison of S-A RANS and DDES.

turbulent predictions and the measurements as compared to the tripless cases. Figure 20 shows the comparison of DES97 and DDES C_f distributions with S-A RANS tripless results. DES97 results show grid dependency with the separation point moving further upstream in the fine grid case while DDES results are grid independent and in good agreement with S-A RANS.

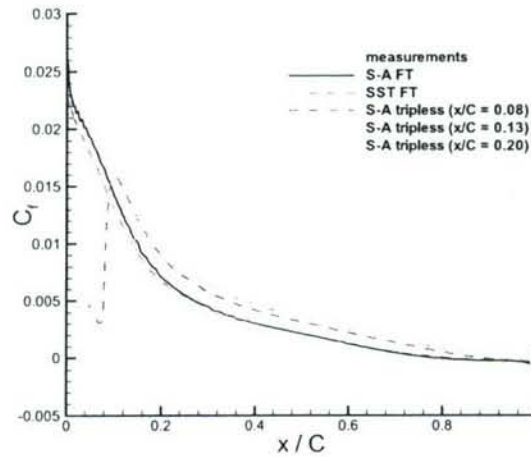


Figure 19: Skin friction coefficient from the RANS cases

4.2.5 Streamwise and wall-normal velocity profiles

The mean velocity components in locations normal to the airfoil surface were measured in the experiments (30). Figures 21 show the comparison of the velocity profiles (experiments, tripless and fully-turbulent RANS) at various stations on the airfoil. The predictions show the fully-turbulent S-

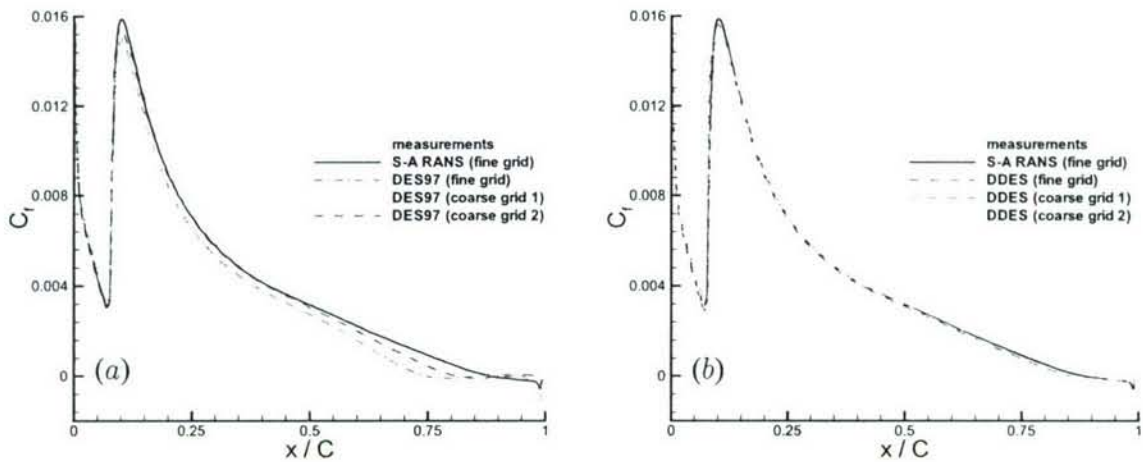


Figure 20: Skin friction coefficient: (a) Comparison of S-A RANS and DES97; (b) Comparison of S-A and DDES.

A and SST results to be in reasonable agreement with the experimental measurements at $x/C = 0.4$ and $x/C = 0.5$, with larger differences visible between the experimental measurements and the results closer to the trailing edge ($x/C = 0.775$ and $x/C = 0.87$). The figures also show that the mean streamwise velocity predicted in the tripless calculations lead that of the fully turbulent solutions.

Figure 22 show the comparison of the streamwise velocity profiles (experiments, S-A RANS, DES97 and DDES) at various stations on the airfoil. The predictions show that the DES97 profiles near the trailing edge (at $x/C = 0.775$ and $x/C = 0.87$) show discrepancies when compared with the RANS. Further, the DES97 results on the ‘fine grid’ do not match with the results on either coarse grid. In contrast, DDES results show no grid dependence and match well with S-A RANS. Figure 23 show the comparison of the streamwise velocity profiles (experiments, S-A RANS, DES97 and DDES) at various stations on the airfoil. These predictions indicate a similar trend with the DES97 profiles near the trailing edge (at $x/C = 0.775$ and $x/C = 0.87$) showing discrepancies when compared with the RANS, while DDES results are essentially grid-independent.

4.2.6 Eddy viscosity ratio

The eddy viscosity ratio at two streamwise locations ($x/C = 0.775$ and $x/C = 0.87$) are shown in figure 24. At $x/C = 0.775$, the peak level of the eddy viscosity ratio corresponds to about 300 in the RANS as well as the DDES cases. The DES97 peak levels are much lower with the peak level as low as 125 in the fine grid simulation. This reduction in the levels of the eddy viscosity ratio leads to MSD. The contrast between the DDES and DES97 levels is even more stark in the eddy viscosity profiles near the trailing edge of the airfoil at $x/C = 0.87$. In the DDES cases,

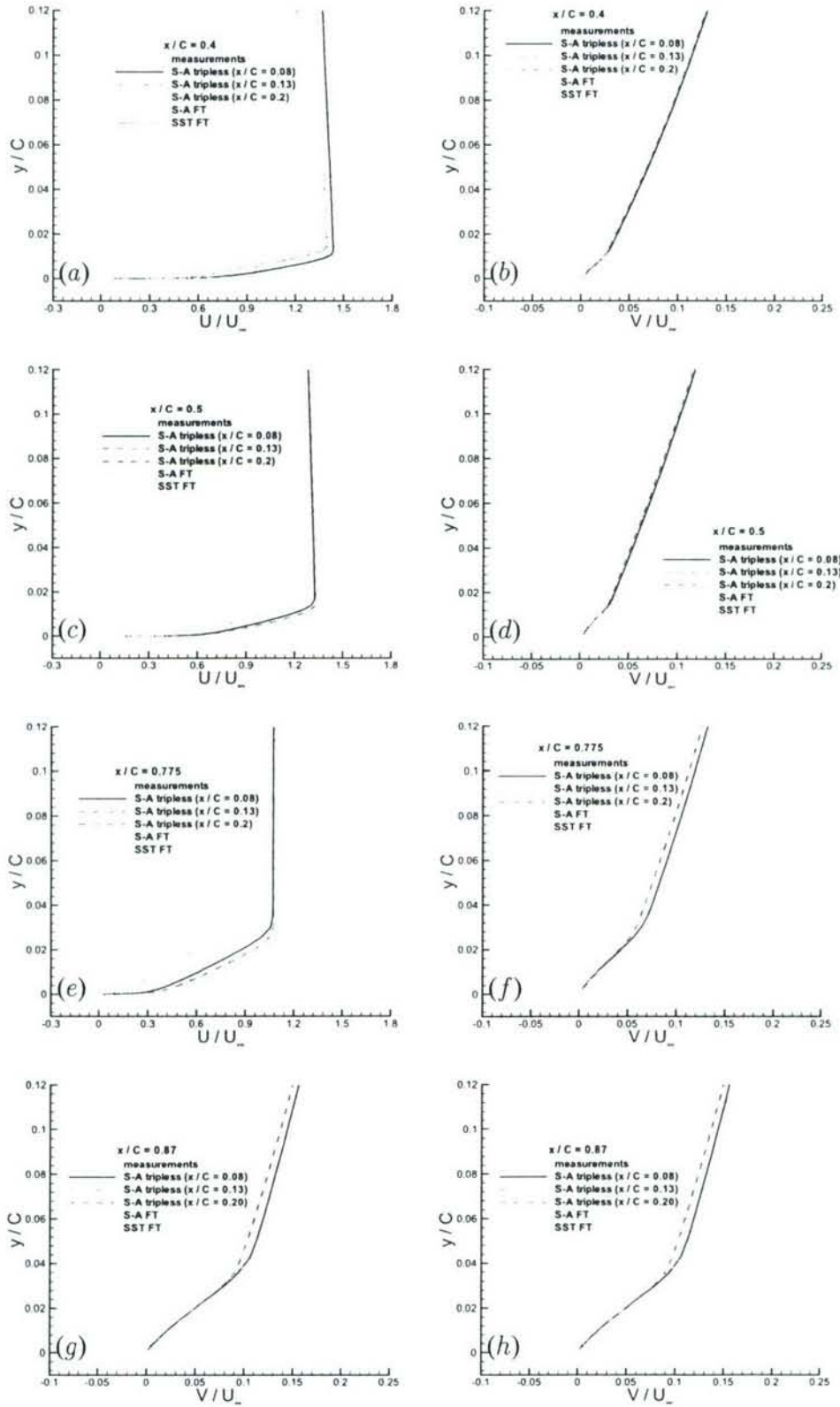


Figure 21: Streamwise and wall-normal velocity profiles at various wall-normal locations (RANS predictions)

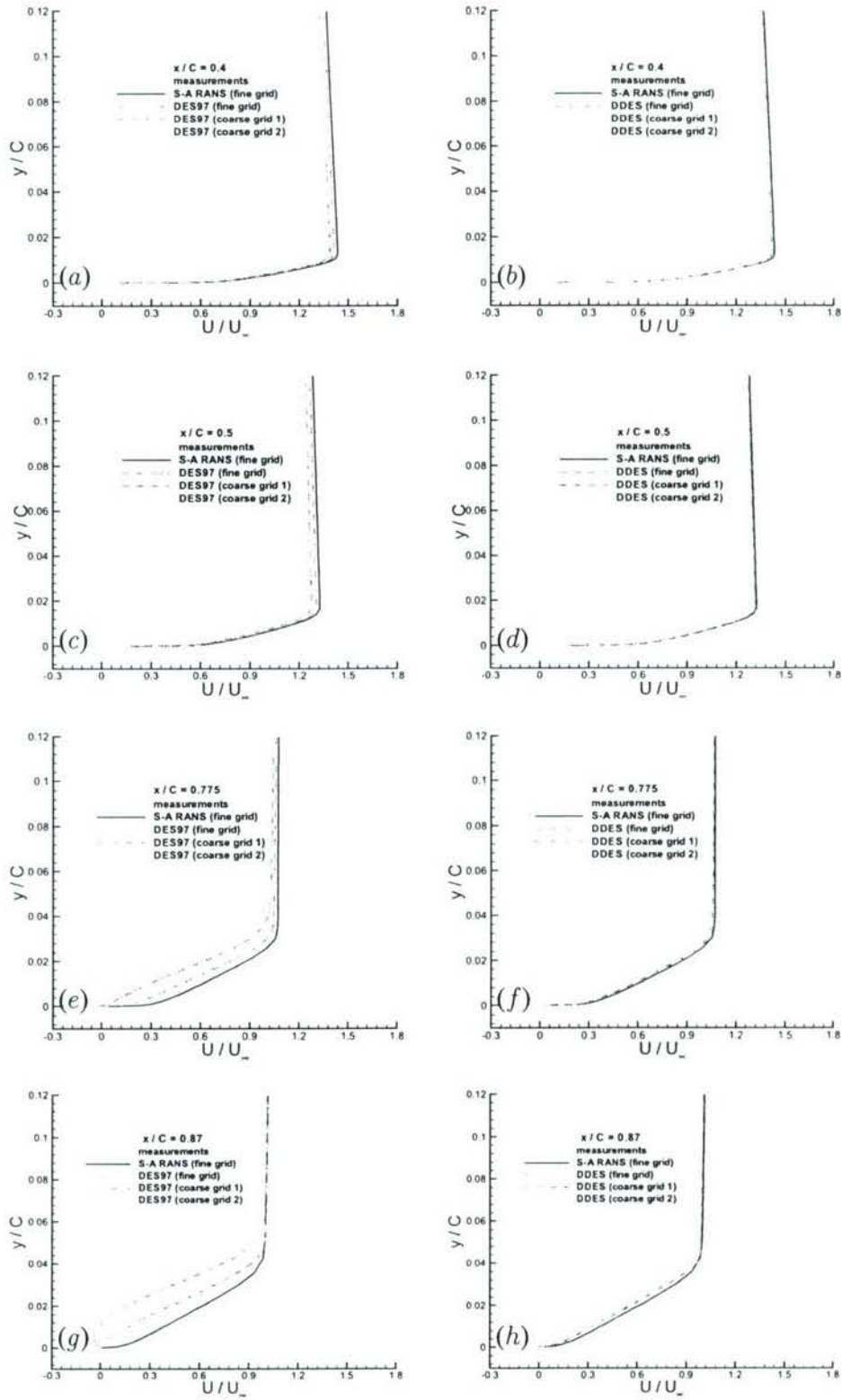


Figure 22: Streamwise velocity profiles at various wall-normal locations comparing S-A RANS, DES97 and DDES

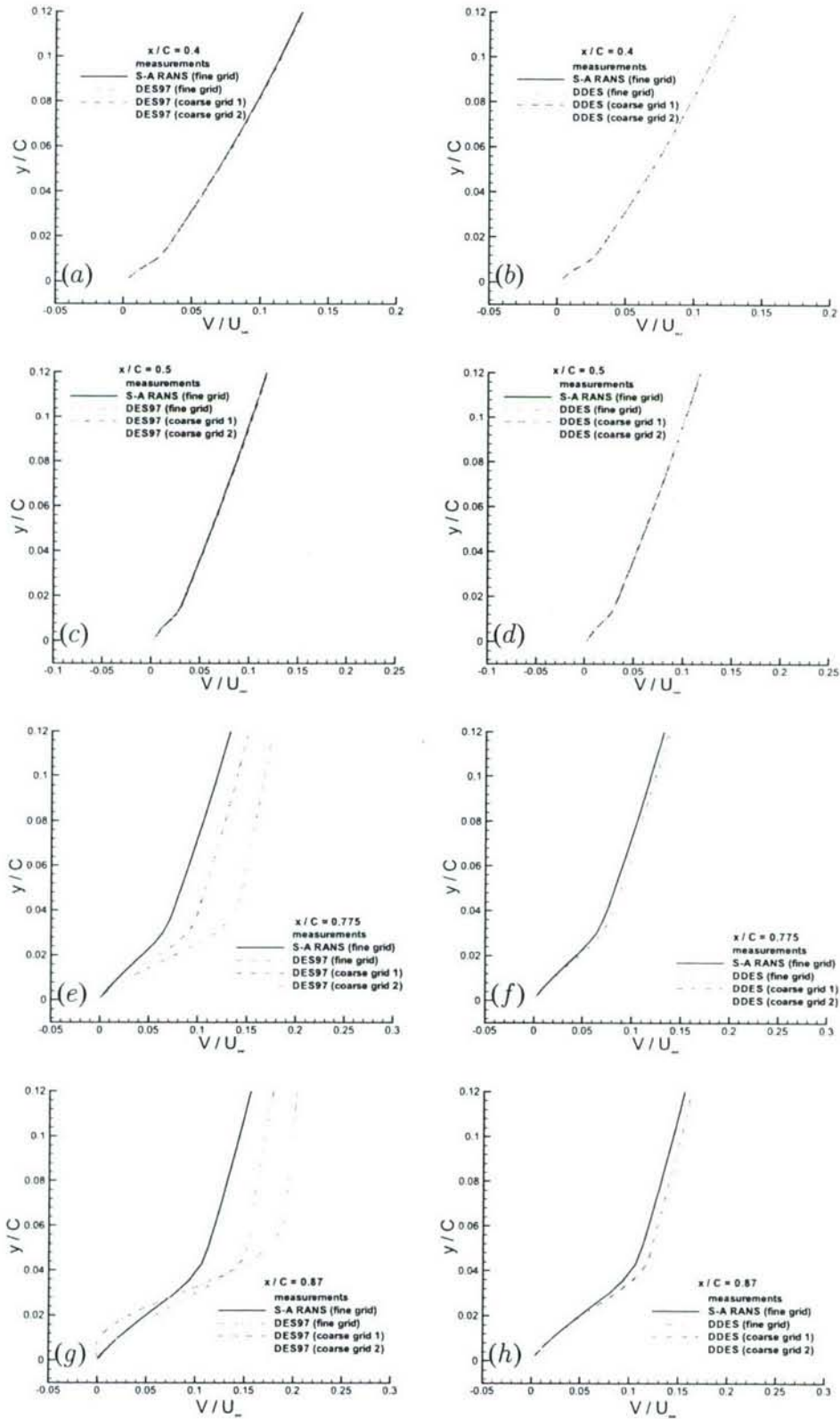


Figure 23: Wall-normal velocity profiles at various locations comparing S-A RANS, DES97 and DDES

the boundary layer has been effectively shielded with RANS being maintained throughout the boundary layer, resulting in no reduction of eddy viscosity and no MSD. This has implications on the separation point predicted by the DDES which does not feel the effect of modifying the grid.

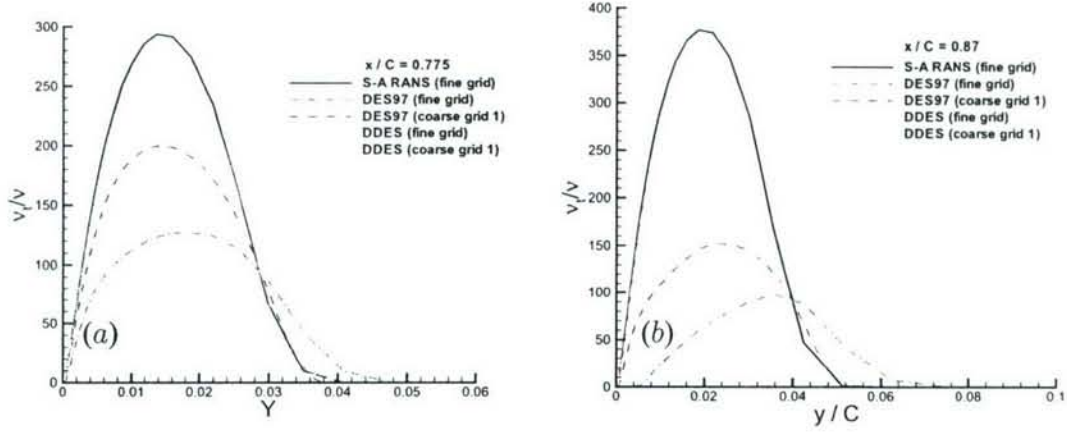


Figure 24: Eddy viscosity ratio at locations corresponding to (a) $x/C = 0.775$; (b) $x/C = 0.87$.

4.2.7 Tabulations of Lift and Drag coefficients

The summary of all the computations of the airfoil for a 13.3° angle of attack are tabulated in tables 4 and 6. In the experiment, the turbulent separation location on the suction side of the airfoil was reported as $x/C = 0.83$, and the lift and drag coefficients were 1.56 and 0.0204 respectively. The table shows that the lift coefficient is higher in general in the tripless runs than in the fully turbulent runs. Among the RANS results involving fully turbulent runs, the S-A RANS lift coefficients appear to be closer to the experiments than the SST. One of the key points to note is that DES97 produces a lift coefficient of 1.40 with the fine grid and values of 1.52 and 1.51 with coarse grids 1 and 2. In contrast to the DES97 results, the DDES lift coefficients are essentially grid-independent and also very close to the experimental values.

4.3 Flow over the Aerospatiale A-Airfoil at $\alpha = 12.3^\circ$

The RANS predictions of the two-dimensional flow were computed using the Spalart-Allmaras (S-A) (with and without rotation correction) and Shear Stress Transport (SST) turbulence models. In this case, only the solutions of the fully-turbulent flow were computed using both RANS models. Even though the pressure coefficient in the RANS solutions are in reasonable agreement with measurements, the peak suction pressure is underpredicted by both models. The summary of all the computations of the airfoil for a 12.3° angle of attack are tabulated in tables 7 and the lift and drag coefficients in table 8. At this angle-of-attack, all the simulations conducted were fully

grid	RANS model	Top Trip location (x/C)	C_L	C_D
medium grid	S-A FT	-	1.51	0.032
	S-A RC FT	-	1.52	0.032
	SST FT	-	1.43	0.033
	S-A tripless	0.2	1.62	0.024
	S-A RC tripless	0.2	1.62	0.024
fine grid	S-A FT	-	1.51	0.033
	S-A RC FT	-	1.52	0.032
	SST FT	-	1.45	0.033
	S-A tripless	0.2	1.62	0.024
	S-A RC tripless	0.2	1.62	0.024
	S-A tripless	0.08	1.60	0.026
	S-A tripless	0.13	1.62	0.024
	S-A tripless	0.12	1.62	0.024
	DES97	0.08	1.40	0.0225
	DDES	0.08	1.55	0.025
coarse grid 1	S-A tripless	0.08	1.60	0.026
	DES97	0.08	1.52	0.0274
	DDES	0.08	1.57	0.0246
coarse grid 2	DES97	0.08	1.51	0.0226
	DDES	0.08	1.57	0.0248

Table 6: Lift and Drag co-efficients for the computations for $\alpha = 13.3^\circ$

turbulent RANS. The results obtained by the S-A RANS, S-A RANS with rotation correction and SST RANS were compared with the experimental results. The location of turbulent separation predicted by the S-A RANS and S-A RANS with rotation correction are very close to each other (at $x/C = 0.84$ and $x/C = 0.83$ respectively), while SST RANS predicts a turbulent separation point further aft, corresponding to $x/C = 0.88$. The lift and drag coefficients predicted are all close to each other and compare reasonably with the experimental values. Figure 25 shows plots of the pressure coefficient distribution over the suction and pressure side of the airfoil. Figure 26 shows the streamwise and wall-normal velocities at points perpendicular to the wall at various chordwise stations on the airfoil. The plots show that all three models predict the velocity profiles adequately at locations corresponding to $x/C = 0.4$ and $x/C = 0.5$, with slight differences cropping up further aft, near the location of turbulent separation. It appears that the SST RANS predicts the wall-normal velocity with greater accuracy than either of the S-A RANS at $x/C = 0.775$ and $x/C = 0.87$.

grid	RANS model	Top Trip location (x/C)	Transition location (x/C)	Turbulent Separation (x/C)
Medium grid	S-A FT	-	-	0.84
	S-A RC FT	-	-	0.83
	SST FT	-	-	0.88
Fine grid	S-A FT	-	-	0.84
	S-A RC FT	-	-	0.83
	SST FT	-	-	0.88

Table 7: Summary of the RANS computations for $\alpha = 12.3^\circ$

grid	RANS model	Top Trip location (x/C)	C_L	C_D
Medium Grid	S-A FT	-	1.42	0.028
	S-A RC FT	-	1.44	0.028
	SST FT	-	1.38	0.029
Fine grid	S-A FT	-	1.44	0.029
	S-A RC FT	-	1.45	0.028
	SST FT	-	1.39	0.029

Table 8: Lift and Drag co-efficients for the RANS computations for $\alpha = 12.3^\circ$

4.4 Flow over the Aerospatiale A-Airfoil at $\alpha = 7.2^\circ$

The summary of all the computations of the airfoil for a 7.2° angle of attack are tabulated in tables 9 and the lift and drag coefficients in table 10. At this angle-of-attack, all the simulations conducted

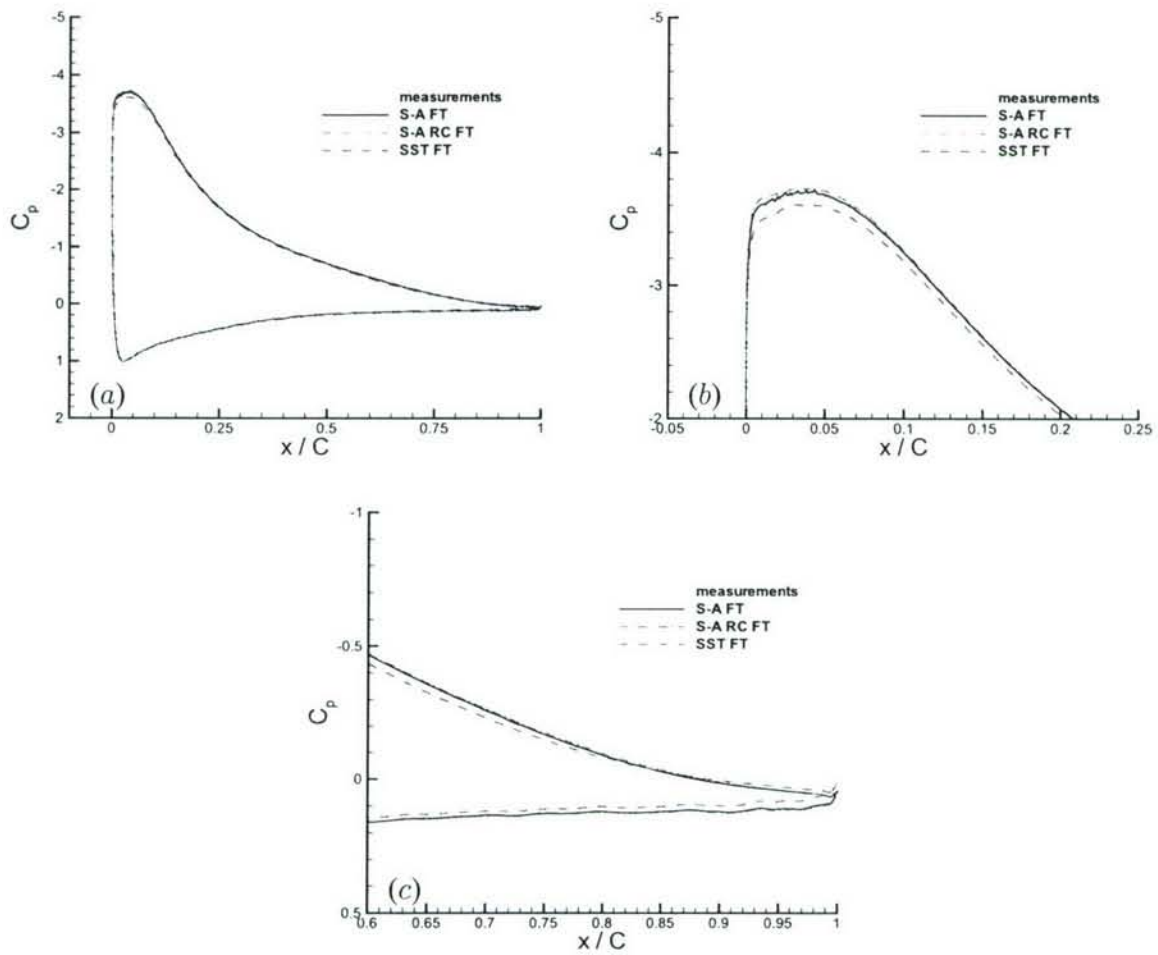


Figure 25: (a) Comparison of pressure coefficient predictions using S-A and S-A RC models; (b) Zoomed view of the pressure coefficient at the leading edge region; (c) Zoomed view of the pressure coefficient at the trailing edge region

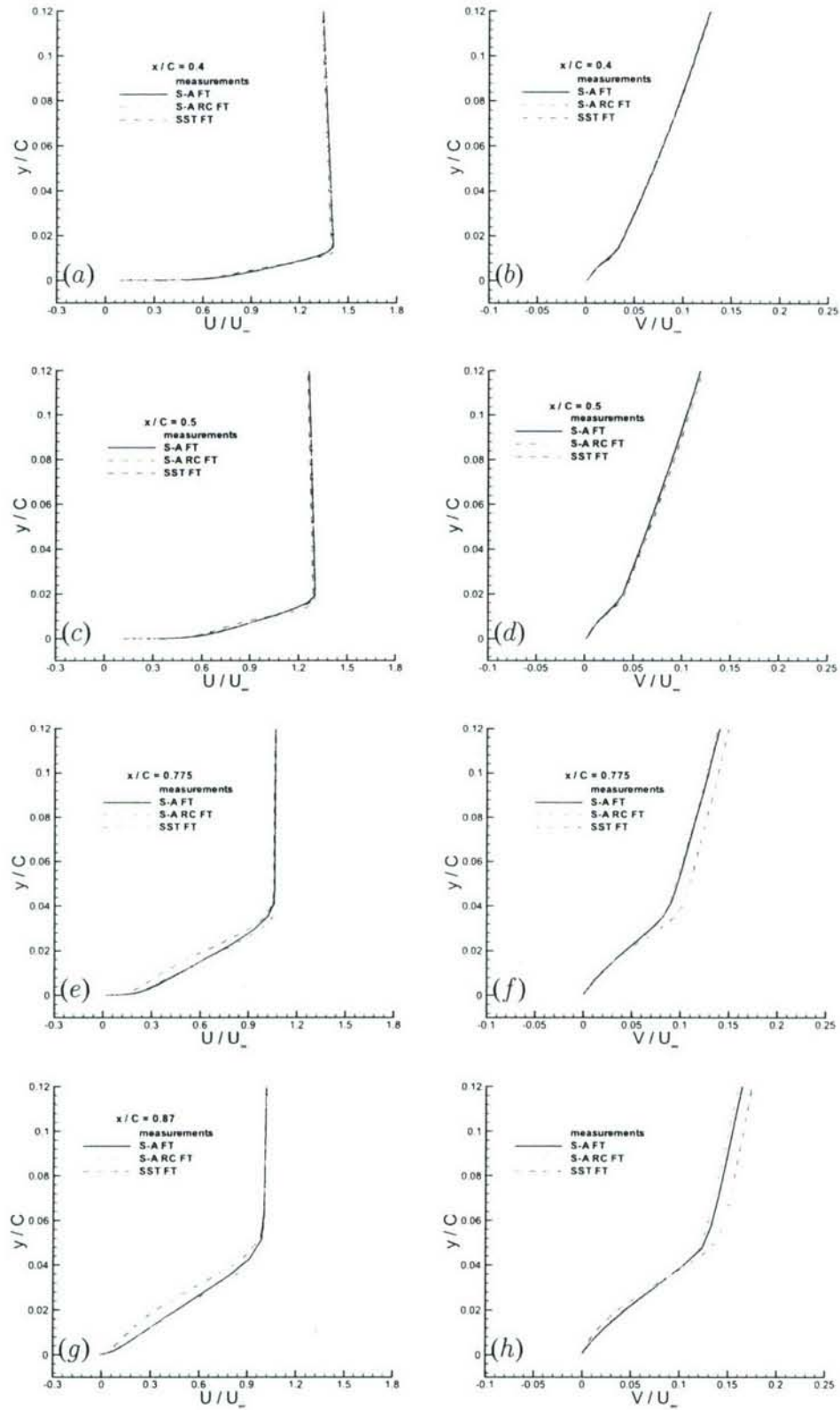


Figure 26: Streamwise and wall-normal velocity profiles at various wall-normal locations

were fully turbulent RANS. The S-A RANS and S-A RANS with rotation correction both predict the same value of the point of turbulent separation ($x/C = 0.97 - 0.98$), while the SST RANS fails to predict any turbulent separation on the surface of the airfoil. The lift and drag coefficients predicted by all models are close to each other and the experimental values.

grid	RANS model	Top Trip location (x/C)	Transition location (x/C)	Turbulent Separation (x/C)
Medium grid	S-A FT	-	-	0.98
	S-A RC FT	-	-	0.97
	SST FT	-	-	-
Fine grid	S-A FT	-	-	0.97
	S-A RC FT	-	-	0.97
	SST FT	-	-	-

Table 9: Summary of the RANS computations for $\alpha = 7.2^\circ$

grid	RANS model	Top Trip location (x/C)	C_L	C_D
Medium grid	S-A FT	-	0.98	0.018
	S-A RC FT	-	0.98	0.017
	SST FT	-	0.96	0.017
Fine grid	S-A FT	-	0.98	0.017
	S-A RC FT	-	0.98	0.017
	SST FT	-	0.96	0.017

Table 10: Lift and Drag co-efficients for the RANS computations for $\alpha = 7.2^\circ$

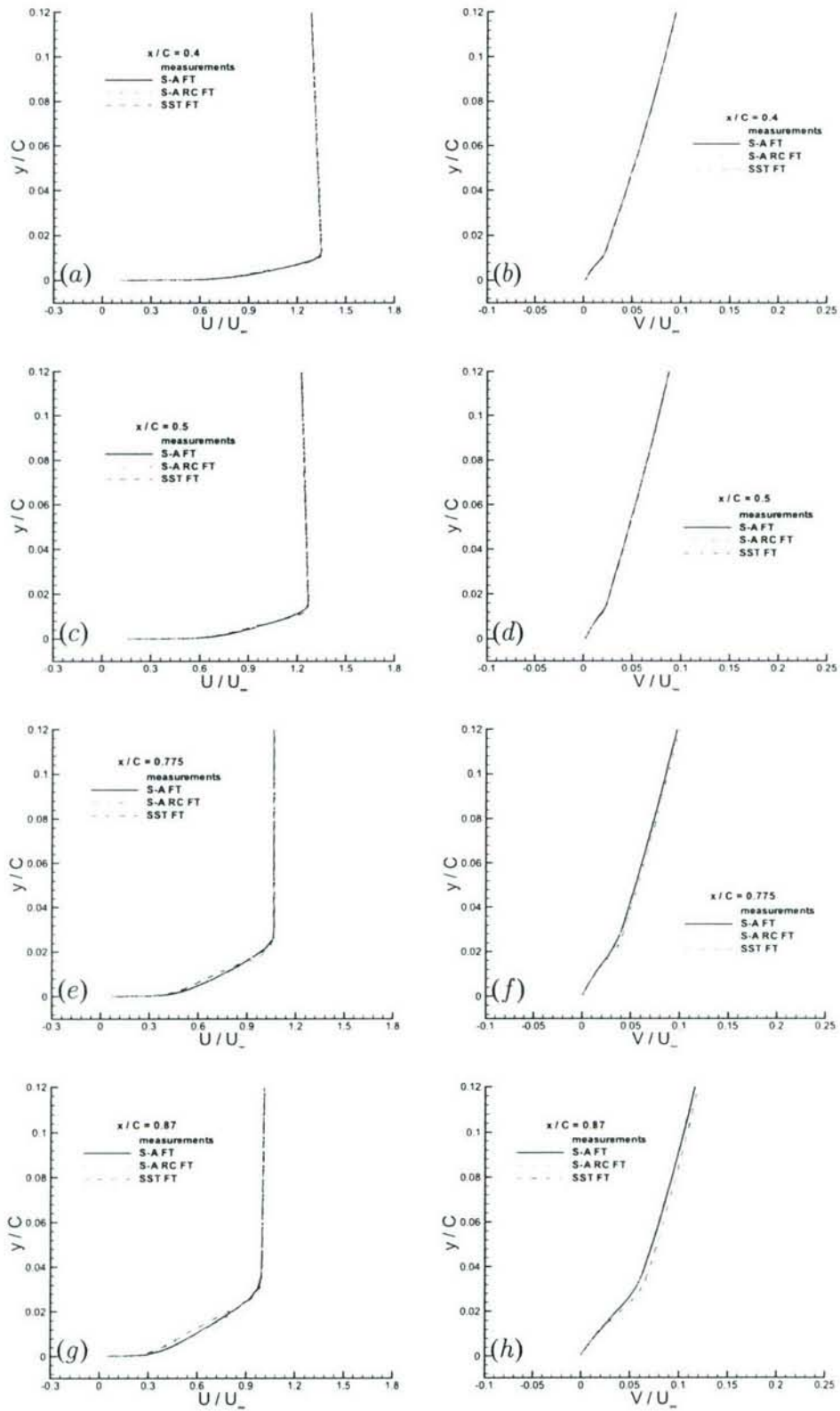


Figure 27: Streamwise and wall-normal velocity profiles at various wall-normal locations

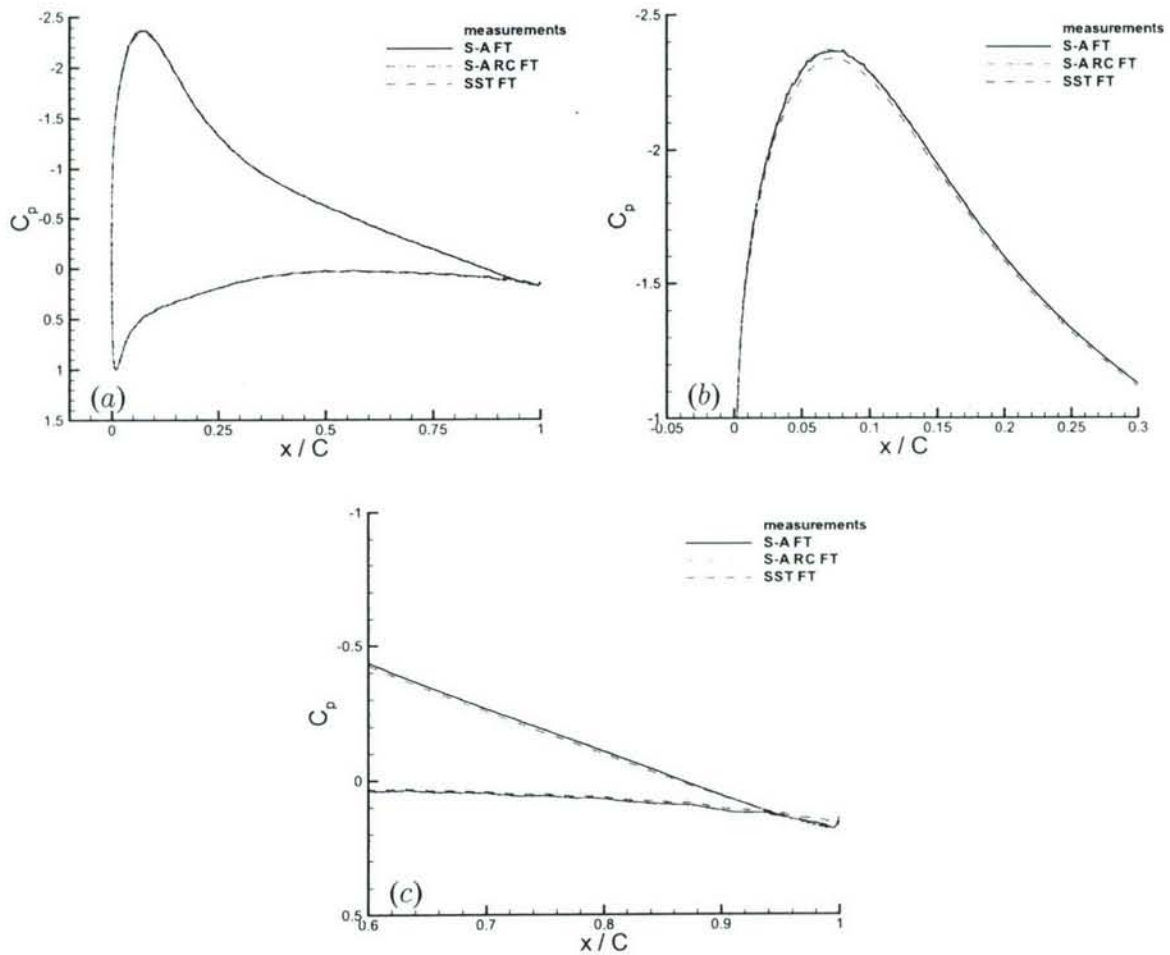


Figure 28: (a) Comparison of pressure coefficient predictions using S-A and S-A RC models; (b) Zoomed view of the pressure coefficient at the leading edge region; (c) Zoomed view of the pressure coefficient at the trailing edge region

5 Seeding boundary layer turbulence in WMLES

5.1 Introduction

Wall-layer modeling was born out of the need to avoid the high cost incurred by conducting LES of high Reynolds number turbulent flows, wherein, a high computational cost results due to the need to accurately represent the near-wall eddies. In wall-layer modeling, the effects of the eddies (small and large) present in the near-wall region are modeled in a statistical sense. This makes the number of grid points required by the calculation of a boundary layer proportional to $Re^{0.4}$ (40) (much lower than the grid requirement for a conventional LES).

Wall-layer models can be generally classified into two types: equilibrium laws and zonal models (40). Equilibrium laws assume the existence of some generalized law-of-the-wall. The wall stress is computed using this general law, which is applied at some distance from the wall. Even though Equilibrium laws have been used with considerable success in simple attached flows, they suffer from major limitations. For example, they cannot be applied easily in complex geometries or on fully-unstructured grids. A case in point is the calculations of the flow in a rotating chaneel, simulated with the use of equilibrium laws by Balaras *et al.* (4). The method adopted failed to predict the quasi-relaminarization observed on one side of the channel.

Zonal approaches are hybrid RANS/LES methods that solve the unsteady RANS equations in the near-wall region and the filtered Navier-Stokes equations away from the wall. In any zonal approach, there is an explicit solution of a different set of equations in the inner layer and the outer layer. For example, Two layer model (TLM) is a zonal approach, proposed by Balaras and Benocci (5) and Balaras *et al.* (4). The method involved the solution of filtered Navier-Stokes equations in the core of the flow and a simplified set of equations solved in the wall-layer (consisting of a fine grid embedded under a coarser, LES mesh. The method was subsequently used by Cabot (6) and Diurno *et al.* (7) to obtain the solution of the flow over a backward facing step and by Wang and Moin (8) in the calculations of the trailing edge of the airfoil. Conventionally, DES has been used in such a way that the entire boundary layer is modeled by RANS. Nikitin *et al.* (72), however, used DES as a wall-layer model in the calculations of plane channel flow. This involved the solution of the URANS equations in the inner layer with the Reynolds shear stress in this region being provided entirely by the turbulence model. In the outer flow, the model was modified to yield a much lower eddy viscosity as compared to a pure RANS model, which allowed the formation of turbulent eddies capable of supporting most of the Reynolds shear stress. Nikitin *et al.* (72) performed calculations with different numerical schemes and grids, over a wide range of Reynolds numbers ($Re_\tau = 180$ to $Re_\tau = 80000$). In this study, it was found that the coefficient of skin friction was underpredicted by approximately 15%. The results also featured the presence of unphysical elongated wall streaks in the RANS region and at higher Reynolds numbers, a logarithmic region with the correct intercept developed in the quasi-steady RANS region and an LES region

characterized by an excessively high intercept of the logarithmic region. Grid refinement only moved the transition region towards the wall without eliminating it. This discrepancy between the log-law intercepts in the inner and outer layer is due to the transition between the LES and RANS regions. This region is characterized by a lower eddy viscosity while the resolved motions are yet to develop. In order to reach the equilibrium value of the shear stress, there needs to be a velocity gradient that balances the reduction in eddy viscosity (40). Another method to alleviate this problem involves the use of a stochastic backscatter model in the inner layer. Baggett (9) opined that the stochastic backscatter had the effect of breaking up the elongated streaks in the RANS region, effectively de-correlating the velocities that enabled a rapid growth of resolved content. Piomelli *et al.* (40) employed a stochastic backscatter model to improve the predictions of the mean velocity profiles and skin friction coefficient.

The use of Detached Eddy Simulation (DES) as a wall-layer model requires a transition between the RANS and LES regions. While this transition from RANS to LES behavior has typically been studied with evolution normal to the wall (4), (6), (40). Of current interest is the transition from RANS to LES along the main flow direction, which can result in applications because of streamwise grid refinement. In either scenario, a DES solution is characterized by a reduction in the modeled length scale which draws down the eddy viscosity, thereby lowering the modeled stress. This reduction in modeled stress requires a corresponding increase in the resolved stress near the transition layer in order to avoid degrading predictions of the skin friction and the mean velocity profile.

The early calculations of temporally developing flows (homogeneous isotropic decay, shear layers, mixing layers, and plane channels) involved the use of periodic boundary conditions in the flow direction. These conditions supply a realistic turbulent field at the inflow, where physically realistic turbulence can be introduced by recycling the outflow plane. In spatially developing flows, on the other hand, inflow conditions must be assigned in a manner consistent with the basic requirements and properties of LES. The early efforts in specifying inflow boundary conditions involved the modification of periodic conditions to supply the inflow velocity. Spalart (45) performed DNS of sink-flow boundary layers and flat-plate boundary layers using periodic boundary conditions. To take into account the variable boundary layer thickness, source terms were used in the equations to transform them into a selfsimilar coordinate flow in which the flow was periodic. Spalart and Watmuff (10) modified this method to include a “fringe” region appended to the end of the domain, in which forcing terms were added to the momentum equations to decrease the boundary layer thickness and re-establish an equilibrium boundary layer. Periodic boundary conditions were then used to reintroduce the outlet velocity field at the inlet. Lund *et al.* (11) proposed a technique developed for flat plate boundary layers, in which a plane of data from a location several boundary-layer thicknesses d downstream of the inflow plane was manipulated by rescaling the inner and outer layers of velocity profiles separately, to account for the different scaling laws

observed in these regions. The rescaled profiles were then re-introduced at the inlet.

Inflow conditions can also be generated by running a separate precursor calculation of an equilibrium flow in which periodic boundary conditions can be used. The velocity field in one plane normal to the streamwise direction can be stored at each time-step. The sequence of planes is then read in as inflow data for a separate calculation. This method has been used with considerable success in the studies of Li *et al.* (11) and Piomelli *et al.* (12). Another class of methods that do not involve recycling are generally based on the generation of synthetic turbulence with assigned moments and spectra, generated using the manipulation of random sequences. Le *et al.* (13) performed calculations of a backward facing step in which a mean velocity profile was assigned at the inflow plane to which random fluctuations were superposed. To determine the random fluctuations, they used the method proposed by Lee *et al.* (14). In this study, it was found that the turbulence levels decayed rapidly (13) because of the lack of phase information of the real turbulent eddies.

Batten *et al.* (69) proposed a new method to generate synthetic turbulence, that takes into account the anisotropy of the flow. The method is based on the superposition of sinusoidal modes with random frequencies and wavenumbers, with given moments and spectra. The approach involved the modification of wavenumbers to yield eddies that are more elongated in the direction of larger Reynolds stresses, thereby introducing more realistic anisotropic eddies into the flowfield. A summary of the synthetic turbulence method is provided below: These investigators applied their method to a hybrid RANS/LES simulation of turbulent channel flow and found that resolved Reynolds shear stress decreased downstream of the inflow. While the shear stress levels subsequently increased with continued downstream evolution, the expected levels were lower than anticipated even ten channel half-heights downstream of the inlet boundary. This discrepancy was attributed to an incorrect behavior of the pressure-strain term in the Reynolds stress budget (69), responsible for rapid decay of the wall-normal ($\langle v'v' \rangle$) velocity variance, resulting in lower values of resolved Reynolds shear stresses. To more quickly re-establish the correct Reynolds shear stress levels, Spille-Kohoff and Kaltenbach (50) proposed a method in which a synthetic turbulent field is prescribed at the inflow plane and a number of control planes are employed downstream of the inlet. These control planes amplify the wall-normal velocity fluctuations in order to drive the resolved shear stress towards a target profile. Piomelli *et al.* (47) applied this scheme to simulations of a spatially-developing channel flow.

In this study (47), Proportional-Integral (PI) controllers were used to increase the resolved stress levels towards the target profile. A PI controller is a generic control loop feedback mechanism widely used in industrial control systems. It attempts to correct the error between a measured process variable and a desired setpoint (desired output), by calculating and then initiating a corrective action that can adjust the process accordingly. The PI controller algorithm involves the interplay between two values: the proportional values and the integral values. The proportional value determines the reaction to the current error while the integral value determines the reac-

tion based on the sum of recent errors. The weighted sum of these two actions is used to adjust the controlled variable. PI controllers with proportional and integral gains corresponding to 1 and 50, respectively, were used to amplify the wall-normal fluctuations downstream of the inflow plane (47). The study (47) found that the error in the Reynolds shear stress was reduced to acceptable levels within five channel half-heights while the skin friction coefficient required longer recovery lengths (around 15 channel half-heights downstream of the inflow plane) (47). Keating *et al.* (61) incorporated a similar synthetic turbulence method to supply inflow boundary data, but with reduced information in the assignment of moments, and assessed the effect on the flow field predictions. These investigators modified the forcing method, by gradually increasing the force over a number of planes upstream of each control plane, ensuring that the resolved Reynolds shear stress reached target levels using two control planes, spaced 1.3 boundary layer thicknesses apart. The transient period for the controllers was significantly reduced (without adverse effects on other parameters) by using values of proportional and integral gains corresponding to 1 and 30 respectively (61). A description of the synthetic turbulence method is provided in the following section.

5.2 Synthetic turbulence

The use of synthetic turbulence requires the specification of complete statistical data (full Reynolds-stress tensor and dissipation rate). Typically when the S-A model is used as the RANS model, these details are not available and this section describes the use of the synthetic turbulence method to generate the inflow condition in the presence of reduced information (61). The method consists of the manipulation of sines and cosines with random phases and amplitudes to obtain an intermediate velocity field:

$$v_i(x_j, t) = \sqrt{\frac{2}{N}} \sum_{n=1}^N \left[p_i^n \cos(\hat{d}_j \hat{x}_j + \omega^n \hat{t}) + q_i^n \sin(\hat{d}_j \hat{x}_j + \omega^n \hat{t}) \right] \quad (40)$$

where,

$$\hat{x}_j = 2\pi x_j / L_b \quad (41)$$

$$\hat{t} = 2\pi t / \tau_b \quad (42)$$

are spatial coordinates normalized by the length- and timescale of turbulence; $\tau_b = k/\epsilon$ and $L_b = \tau_b V_b$ are the turbulence timescale and turbulence lengthscale, and V_b is given by $k^{1/2}$ where k is the turbulent kinetic energy. The random frequencies $\omega^n = N(1, 1)$ are taken from a normal distribution $N(\mu, \sigma^2)$ with a mean and variance of 1. The amplitudes are given by,

$$p_i^n = \epsilon_{ijk} \zeta_j^n d_k^n \quad (43)$$

$$q_i^n = \epsilon_{ijk} \xi_j^n d_k^n \quad (44)$$

where ζ_j^n and ξ_j^n are given by $N(0, 1)$, and,

$$\hat{d}_j^n = d_j^n \frac{V}{c^n} \quad (45)$$

are modified wavenumbers obtained by multiplying the wavenumbers d_i^n by V_b/c^n , where c^n is given by,

$$c^n = \sqrt{\frac{3}{2} \langle u_l' u_m' \rangle \frac{d_l^n d_m^n}{d_k^n d_k^n}}. \quad (46)$$

The isotropic distribution of wavenumbers d_j is thus transformed into an anisotropic one, resulting in eddies stretched in the directions of greatest Reynolds stress. The wave-numbers $d_i^n = N(0, 1/2)$ are chosen from a normal distribution with variance $1/2$. A tensor scaling is used to reconstruct the synthetic turbulent fluctuation field,

$$u_i' = a_{ik} v_k \quad (47)$$

where a_{ik} is the Cholesky decomposition of the Reynolds stress tensor. When only reduced information is available, the method can be implemented as described below. When the S-A RANS turbulence model is used, the eddy viscosity is related to the turbulent kinetic energy using the experimental result of Bradshaw *et al.* (1).

$$|-\langle u'v' \rangle| = \nu_t \left| \frac{\partial u}{\partial y} \right| = a_1 k \quad (48)$$

where $a_1 = \sqrt{c_\mu}$ and $c_\mu = 0.09$. To obtain the individual stresses $\langle u'u' \rangle$, $\langle v'v' \rangle$ and $\langle w'w' \rangle$, the ratio of the above three stresses for a nominal boundary layer is obtained (from experimental observations or Direct Numerical Simulations (DNS)). In the current study, the ratio of the three stresses were obtained from DNS of a channel flow at $Re_\tau = 180$ (3). Once these ratios are obtained, the levels of the individual stresses that add up to form k , calculated using 48 can be obtained. To obtain the timescale, the definition of eddy viscosity from the $k - \epsilon$ two-equation turbulence model can be used,

$$\epsilon = c_\mu \frac{k^2}{\nu_t} \quad (49)$$

$$\tau_b = \frac{k}{\epsilon} = \frac{1}{\sqrt{c_\mu} \left| \frac{\partial U}{\partial y} \right|} \quad (50)$$

5.3 Boundary layer stirring and control methodology

As discussed earlier, the use of DES as a wall-layer model results in a transition zone between the RANS and the LES regions, characterized by a lower modeled stress and requiring an increase in the resolved stress near the transition layer. The resolved Reynolds stress could be increased by

providing realistic fluctuations in the transition layer, by seeding the boundary layer with three-dimensional content, to achieve a result similar to that accomplished by the use of inflow boundary conditions. In the current effort, resolved stresses are generated by seeding the near-wall flow with fluctuations in order to generate three-dimensional structure in the boundary layer. Downstream of the streamwise location at which the fluctuations are seeded, control planes are employed to amplify the wall-normal velocity fluctuations in order to tune the resolved shear stress levels based on a target profile. In this part of the study, a stochastic force added to the momentum equations is used to generate velocity fluctuations. These fluctuations are subsequently amplified based on a prescribed shear stress profile at a number of control planes downstream of the stochastically stirred region. Velocity fluctuations were seeded into the near-wall flow using a stochastic force formed from Gaussian random numbers scaled such that the magnitude of the force is maximum near the location of the RANS-LES interface. Equation (51) shows one of the forms of the stirring force used to generate fluctuations:

$$f_{s,i} = \frac{A_s(\lambda y)^4}{1 + (\lambda y)^2} \eta_{s,i}. \quad (51)$$

In (51), λ is a constant that ensures that the amplitude of the stirring force is maximum near the RANS-LES interface; A_s represents the amplitude of the stirring force. Preliminary investigations were also conducted using different forms for the stirring force based on the values of A_s (in each of the three directions) and λ in order to assess the influence on the resulting velocity fluctuations.

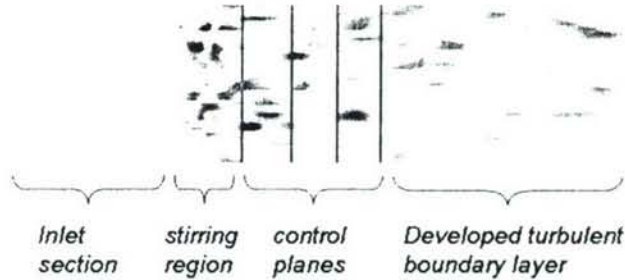


Figure 29: Schematic depicting the inlet, stirring region, and controllers. The stirring region is applied over a streamwise distance of 0.5δ and four control planes are spaced δ apart. The distance between the end of the stirring region and the first control plane is 0.2δ .

The controller uses the error in the Reynolds shear stress as its input parameter. The error is obtained by a comparison of the Reynolds shear stress to a prescribed set point (47):

$$e(y, t) = \langle u'v' \rangle (x_0, y) - \langle u'v' \rangle^{z,t} (x_0, y, t) \quad (52)$$

where $\langle u'v' \rangle (x_0, y)$ is the target Reynolds stress at streamwise reference location $x = x_0$, and $\langle u'v' \rangle^{z,t} (x_0, y, t)$ is the current value, averaged over the spanwise direction and over time using a

short backward time average,

$$\langle u'v' \rangle^{z,t}(t + \Delta t) = \frac{\Delta t}{T_{avg}} \langle u'v' \rangle^z + \left(1 - \frac{\Delta t}{T_{avg}}\right) \langle u'v' \rangle^{z,t}(t). \quad (53)$$

In (53), $T_{avg} = 2\delta/U_c$, the superscripts z and t indicate averaging over the spanwise direction and time, and U_c refers to the velocity at the center of the channel. As described in Piomelli *et al.* (47) and Kaltenbach *et al.* (50), the forcing aims at the enhancement or damping of local events that contribute to the Reynolds shear stress. This is achieved by the formula,

$$f_c(x_0, y, z, t) = r(y, t) (u(x_0, y, z, t) - \langle u \rangle^{z,t}(x_0, y)), \quad (54)$$

where the magnitude is controlled by the error according to,

$$r(y, t) = K_p e(y, t) + K_I \int_0^t e(y, \alpha) d\alpha, \quad (55)$$

where K_p and K_I are the proportional and integral gains of the controllers, respectively. Piomelli *et al.* (47) reported that unrealistically high shear stress events were prevented by applying the control force only when $|u'| < \gamma_u U_b$ and $|v'| < \gamma_v U_b$, where $\gamma_u = 0.6$, $\gamma_v = 0.4$, and U_b is the bulk velocity. Further, forcing employed (47) was concentrated on more energetic events by applying the force only when the additional criterion $|u'v'| > 0.00015U_b^2$ was satisfied (47). These additional conditions were not used in the control schemes implemented in the current work as discussed below. The most significant issue in the application of the method is that the use of controllers (i.e., body forces) requires the specification of gain values that dictate the rate of convergence of the resolved shear stress to the target values and also ensure that the forcing applied is not too large or unphysical. If chosen incorrectly, the gain values induce instabilities in the control process, resulting in an output that diverges. Even though this can be rescinded by the use of saturations which deactivate the control commands and ensure that the forcing is not applied whenever a predefined criterion is not satisfied, this is not desirable as it has implications on the control process. The primary focus of the current effort is to investigate the control process and to analyse the effect of different control methodologies (use of Proportional-Integral controllers, use of integral controllers, use of non-linear Proportional-Integral controllers based on non-linearities in the system and adaptive controllers) in achieving the desired levels of resolved shear stress at the specific control planes.

As described below, early stages of the investigation involved the system identification process, with the objective of identifying a linear model formed from the open loop response of the resolved shear stress using random inputs at the control planes. Optimal gains for the controller are specified based on the location of the poles of the linear model in the closed-loop configuration. The shortcomings of this method are explained in detail later in this chapter.

During the next stage of the investigation, the response of the non-linear system to preset gain values was measured during a precursor simulation. These gain values were then incremented

until the onset of numerical instabilities. The value of gain obtained prior to the onset of numerical instabilities can then be used in the final simulations. It is to be noted that such a method is used to arrive at the gain for an integral controller and has been described in greater detail in the later sections. This method was not found to work accurately despite the use of very small increments of the gain values (of the order of 10^{-6}) in the precursor simulation. It was found that during the initial stages of the simulation, due to the absence of any fluctuations the gain values would increase and reach higher values compromising the stability of the precursor simulation. These values of gains were not small enough to ensure the stability of the simulation of interest. Subsequently, a deep investigation of the control process and the effect of the use of different controllers on the system was conducted. In this part of the work, the behavior of the error in the system for various controllers was thoroughly investigated. It was found that the wall shear stress and resolved Reynolds stress levels are independent of the type of controller used in the method, implying that there is little to be gained in the use of a PI controller over an integral controller. However, the specification of optimal gains that keep the system stable is a key issue and to make the process less ad-hoc, an adaptive integral controller was developed. This adaptive controller adjusts the integral gain value during the simulation ensuring that the stability of the system is not compromised.

The use of integrator-based controllers to achieve target resolved stress levels has also been tested in channel flow with the use of the ‘synthetic turbulence’ inflow condition of Batten *et al.* (69). In this case, the three-dimensional content is supplied by the inflow condition, and the use of the stochastic force in the momentum equations is obviated. Some of these predictions have also been included in this report. Other issues involved in the method, such as the effect of the form and magnitude of the stirring force on the rms values of the velocity fluctuations, the effect of grid refinement, and number of controllers used on the wall shear stress are also discussed.

5.4 Simulation overview

5.4.1 Numerical method

Spatial derivatives in the governing equations were discretized using second-order central differences on a staggered grid. In the momentum equations, the diffusion terms are advanced using Crank-Nicolson, while the remaining terms are advanced explicitly using a second-order Adams-Bashforth method. For the transport equation for the variable \bar{v} in the S-A model equation, the diffusion term is treated implicitly while all other terms are treated explicitly. The equations are advanced in time using a semi-implicit fractional step method. The Poisson equation for pressure is solved using a direct approach based on Fourier transforms. No-slip boundary conditions are applied at the lower and upper walls of the channel. Periodic boundary conditions were used in the spanwise direction and the inlet boundary condition was fixed with a RANS profile making-up

the specified variables. A convective boundary condition was employed at the outlet of the domain with the outflow velocity corrected at every time step to ensure mass conservation.

5.4.2 Computational grid

Computations were performed at Reynolds numbers of 400 and 5000, based on friction velocity and channel half-width δ . The grid sizes used for all the simulations are summarized in Table 11. The spanwise extent of the channel was fixed at π for all the cases. For the coarse grid with $\Delta_z = 0.1$, the RANS-LES interface was located at a wall-normal distance $y/\delta = 0.065$ from the channel walls (corresponding to $y^+ = 26$ when $Re_\tau = 400$ and $y^+ = 325$ when $Re_\tau = 5000$). For the fine-grid runs with the grid size $129 \times 75 \times 65$, the number of controllers and the spacing between the controllers was also varied to study their effect on the wall shear stress. The runs conducted have been summarized in Table 12.

Re_τ	grid	Method	Δ_x	Δ_z	Streamwise extent
400	$129 \times 75 \times 33$	Boundary layer stirring with controlled forcing	0.1	0.1	4π
	$129 \times 75 \times 33$	Synthetic turbulence with controlled forcing	0.1	0.1	4π
	$259 \times 75 \times 33$	Synthetic turbulence with controlled forcing	0.1	0.1	8π
5000	$129 \times 75 \times 33$	Boundary layer stirring with controlled forcing	0.1	0.1	4π
	$129 \times 75 \times 65$	Boundary layer stirring with controlled forcing	0.1	0.05	4π
	$195 \times 75 \times 65$	Boundary layer stirring with controlled forcing	0.1	0.05	6π
	$259 \times 75 \times 65$	Boundary layer stirring with controlled forcing	0.1	0.05	8π

Table 11: Grid sizes used for the channel flow investigations.

Number of controllers	Spacing between controllers
5	$x/\delta = 1.0$
5	$x/\delta = 0.5$
10	$x/\delta = 0.5$

Table 12: Runs conducted with the fine grid with the grid size $129 \times 75 \times 33$ cells in the streamwise, wall-normal, and spanwise directions, respectively.

5.5 Design of the controllers

PI controllers have widespread applications in process control, particularly when the mathematical model of the system is unknown and analytical methods for system design are not applicable. The PI controller shown in (55), applied by Piomelli *et al.* (47) has the standard form, consisting of a proportional term and an integral term. The proportional term ensures that the controller output ($r(y, t)$) is proportional to the error ($e(y, t)$) of the system while the integral term ensures that the error accumulated over a period of time is taken into account by multiplying this quantity to a constant and then added to the controlled quantity ($r(y, t)$).

The open loop transfer function (ratio of the Z -transform of the output to the Z -transform of the input) of the PI controller in the discretized form is given by (56), where K_p represents the proportional gain and K_i represents the integral gain.

$$C(z) = K_p \left(1 + \frac{z}{\frac{K_p}{K_i}(z-1)} \right) \quad (56)$$

The PI controller described above forms a part of a non-linear system, the solution of which can be considered to be the whole-integration scheme of the Navier-Stokes equations (inclusive of the body forces).

A detailed analysis of the control process has been carried out with the goal of maximizing the rate of convergence of the resolved stress to the desired values and also ensure the stability of the closed loop system without the use of any ad-hoc adjustments in order to prevent the numerical method from diverging. ‘Stability’ in this case implies that the output shear stress remains bounded over any amount of time for a bounded input control force.

Prior to the discussion on system identification of a linear model, results showing that the a purely integral controller is sufficient in achieving the desired results are shown. Figure 30 shows the responses of the system, i.e., time development of $\langle u'v' \rangle^{z,t}$, at the third control plane. Shown are time histories at two wall-normal locations between the wall and RANS-LES interface, $y/\delta = 0.0321$ ($y^+ = 161$) and $y/\delta = 0.0168$ ($y^+ = 84$) along with the set point for a case with $K_p = 0$ and $K_i = 0.5$. In the figures, filtered response refers to a low pass filtered form of the output that confirms that the mean of the output is very close to the set point. The mean of the response matches the set point very closely, showing that the integral controller is effective in eliminating the steady state error.

5.5.1 Identification of a linear model

Initial efforts were focused on the identification of a linear model, and arriving at integrator gain values based on the model poles. During the identification step, controller parameters are chosen so as to produce outputs (i.e., resolved shear stress) that are of the same order of magnitude as the desired outputs; this ensures that the system operates in the vicinity of the set point (the target

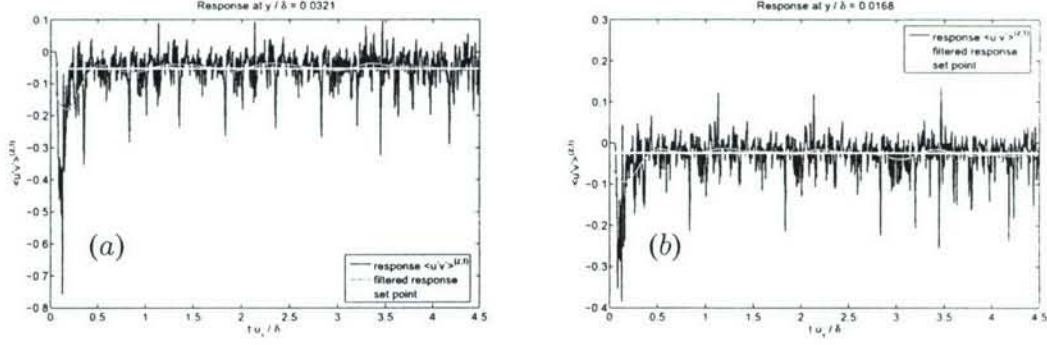


Figure 30: System response at wall-normal locations $y/\delta = 0.0321$ ($y^+ = 161$) and $y/\delta = 0.0168$ ($y^+ = 84$) at the third control plane $x/\delta = 2.15$.

Reynolds shear stress). In this first step, Gaussian-distributed noise (χ) is added by each controller instead of the control force, and the inputs and corresponding outputs (resolved shear stress) are recorded. A linear model is fit to these data, and since the data have been collected in the vicinity of the desired set point for the system, the resulting model can be considered as an approximation of the linearization of the numerical scheme around the set point. With such a setup, the system is said to be in open-loop mode as there is no control action that determines the inputs that are added. The state space representation of the linear model is given below:

$$x_{t+1} = Ax_t + B\chi \quad (57)$$

where,

- x_t represents the difference between the output of the system - $\langle u'v' \rangle^{z,t}(t)$ and the setpoint;
- χ represents the input to the system - the noise added in the open loop system;
- A and B are the state matrix and input matrix respectively, with A representing the state of the system (matrix that represents the dynamics of the system, that summarizes the effect of past inputs on future outputs of the system).

Studying the dynamics of the system in the open-loop configuration give insights on the underlying structure of the system, accomplished by examining the eigenvalues of the dynamic matrix A . These eigenvalues represent the poles of the system under consideration. Equation 57 can be manipulated to obtain the matrices A and B ,

$$X = [A \ B][X_s \ \chi]^T \quad (58)$$

$$X[X_s \ \chi] = [A \ B][X_s \ \chi]^T[X_s \ \chi] \quad (59)$$

$$[A \ B] = X[X_s \ \chi] \left([X_s \ \chi]^T[X_s \ \chi] \right)^{-1} \quad (60)$$

where,

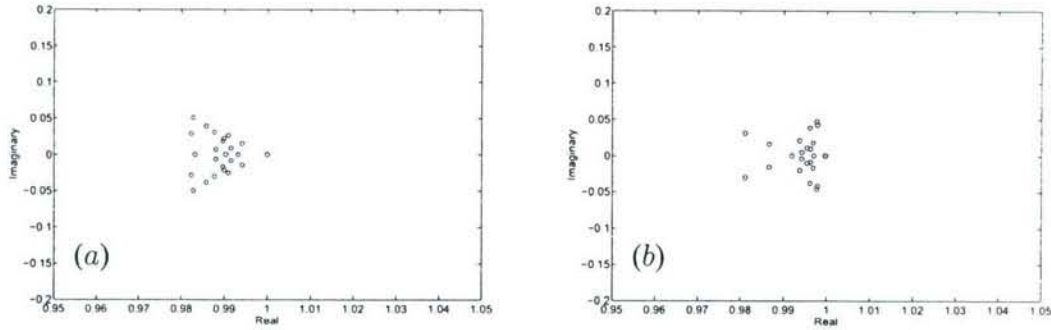


Figure 31: eigenvalues of the open-loop configuration (a) with η approximately 700% of the output of the controller; (b) with η approximately 10% of the output of the controller.

- X represents a vector that contains the difference between the output of the system - $\langle u'v' \rangle$ and the set point at time level $n + 1$ (from data collected during the identification step);
- X_s represents a vector that contains the difference between the output of the system - $\langle u'v' \rangle$ and the set point at time level n (from data collected during the identification step).

Figures 31a,b show the eigenvalues of the dynamic matrix (A) for two cases in the open-loop configuration. Figure 31a shows the eigenvalues of the dynamic matrix for a case in which the standard deviation of the noise η was approximately 700% of the output resolved shear stress. Such a large magnitude of the standard deviation of the noise η enables a more robust characterization. Figure 31b shows the eigenvalues of the dynamic matrix for a case in which the standard deviation of the noise χ was approximately 10% of the output of the controller. The figures show that the eigenvalues of the dynamic matrix A are invariably close to the edges of the unit circle. Thus, system identification can be accomplished using χ that has a much higher standard deviation than the term $r(y, t)$ in equation 55, increasing the robustness of the characterization.

5.5.2 Closing the loop and obtaining the gain values

A system is said to be in a closed-loop configuration when there is an active feedback control loop that acts to control the output of the system. The closed loop response of the system depends upon the location of the poles of the linear model in a closed loop configuration. Poles and zeros of a transfer function are the frequencies for which the transfer function becomes infinity and zero respectively. The values of the poles and zeros of a system determine if the system is stable and the response of the system. Control systems can be designed by assigning specific values to the poles and the zeros of the system. The loop can be closed by the placement of a pole at the edge of the unit circle corresponding to $z = 1$ and arriving at an appropriate gain value for the integral controller. Since it is desired to have the system output match the set point exactly, and since

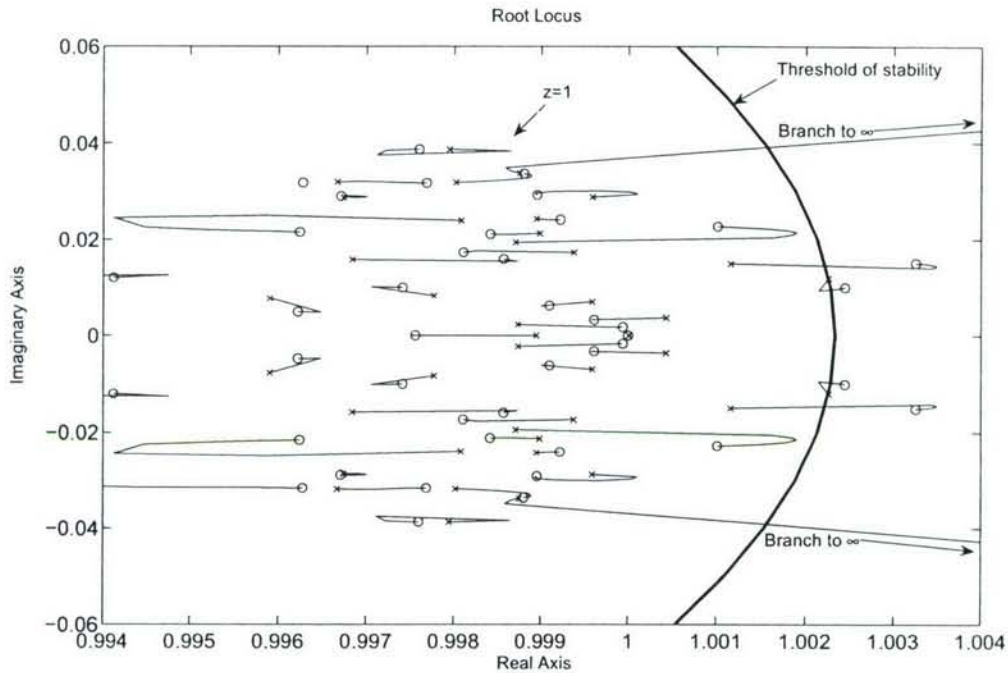


Figure 32: Root Locus Plot for a particular combination of output and input. In this diagram, \circ represents the zeros of the system and x represents the poles of the system.

the set point is constant with time, then the integral controller itself is sufficient for this purpose. The proportional term is therefore not useful, thus it can be set to zero. The results shown below confirmed this conclusion, by comparing the effect of a controller using the integral term only with other controllers using different values of K_p . An attempt was made to find the optimal value of the integrator gain by studying the locus of the poles of the transfer function of the system in closed-loop as the integrator gain is varied. To arrive at the optimal gain, the MIMO (Multiple-Input Multiple-Output) model was split into a number of SISO (Single-Input Single-Output) systems and the smallest value of the gain for which the model remains stable was selected. The optimal gain is the minimum value among the gains arrived at for all the sets of individual inputs and outputs that ensures that the system remains stable.

The threshold of stability for the system is defined on the basis of the location of the poles of the model. The definition of the threshold is justified because the corresponding system is stable in the open-loop configuration despite the model having poles outside the unit circle. This is not a contradiction, because the linear model approximates the behavior of an underlying nonlinear system, which is the numerical integration scheme. Therefore, we can consider the circular boundary marked by the outermost linear model poles as a “safety region”, in the sense that we know that the corresponding nonlinear system is stable for that given location of the outermost linear

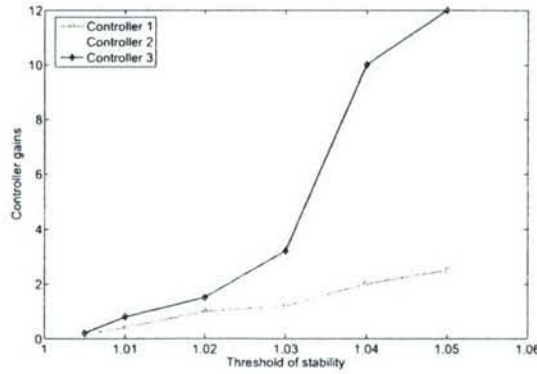


Figure 33: Variation in the gain values as the threshold of stability is varied.

model poles. We can also assume that if the poles of the controlled linear model remain within that region, then the corresponding controlled nonlinear system will also be stable. On the other hand, since the poles of the controlled model are farther from the origin and closer to the edges of the unit circle, the controlled system will have a more rapid response, i.e., faster convergence of the resolved shear stress towards the desired values. Figure 32 shows a representative plot of the root locus for a particular combination of output and input. The plot also shows the threshold of stability defined on the basis of the location of the poles of the subsystem under consideration.

In spite of altering the location of the threshold of stability of the linear model, it was found that the non linear system remained stable with gains much higher than those found by the root locus method. The optimal gains obtained by using the above procedure were of the order of 10^{-10} , much smaller than gain values that kept the non-linear system stable. To determine and confirm that the location of the threshold of stability resulted in very small gain values, the root locus analysis was repeated with the location of the threshold of stability varied. A test case with three controllers spaced 0.5δ apart, and with the first controller 0.2δ downstream the stirring region was used to analyse the variation in gains with respect to the variation in the threshold of stability. Figure 33 indicates that as the threshold of stability is moved farther away from unity, the root locus paths remain inside the defined stable region for a longer time, and higher gains are obtained as a result of the application of the methodology. This confirms the conclusion that the threshold of stability of the linear model does not match well with the region of stability of the non-linear system.

5.5.3 Accuracy of the linear model

To check the accuracy of the linear model, the following tests were carried out:

- The poles of the linear model were obtained for two different timesteps to see if the model is accurate. Figure 34 shows the location of the poles of the linear model in the open-loop configuration for two cases in which the system identification was carried out at timesteps

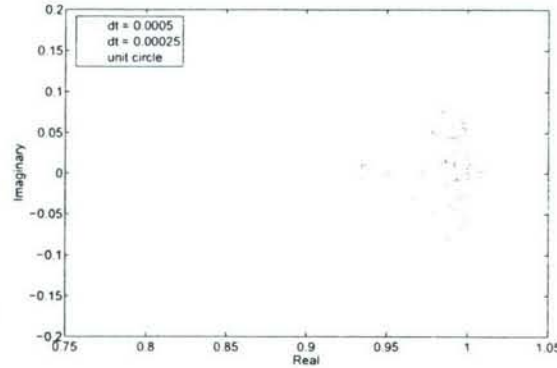


Figure 34: Location of the poles of the linear model in the open-loop configuration for two cases with $dt = 0.0005$ and $dt = 0.00025$.

of $dt = 0.0005$ and $dt = 0.00025$. It is seen from the distribution of the poles of the linear model that there are only slight differences between the two cases, which confirms the accuracy of the linear model.

- The poles of the dynamic matrix A were obtained for a conventional DES97 run to check if the distribution of the poles of the linear model is similar to the distribution obtained with the precursor simulation with stirring and with the system in open-loop. Note that in this case, there was no random force being added during the system identification step. It was found that the poles of the linear model so obtained had a similar distribution to the earlier cases.
- The linear model was used to predict future data (of the resolved shear stress) and this data obtained was compared with data obtained from the non-linear system. Figure 35 shows that the data obtained from the linear model compares favorably with the data obtained from the non-linear system, further confirming the accuracy of the linear model.

5.5.4 Reduction of the order of the linear model using Proper Orthogonal Decomposition (POD)

Proper Orthogonal Decomposition (POD) is a technique that can be used to simplify a data set to a lower dimension for ease of analysis. This can be accomplished in a manner that the dimensionality of a data set is reduced, but the dataset still retains those characteristics of the data set that contribute most to its variance.

The main reasons for generating reduced models include:

- Lower order models reduce the computational effort to obtain the desired results.
- Lower order models facilitate or ease controller design with the resulting controller having a simpler structure that is easier to understand and parameterize.

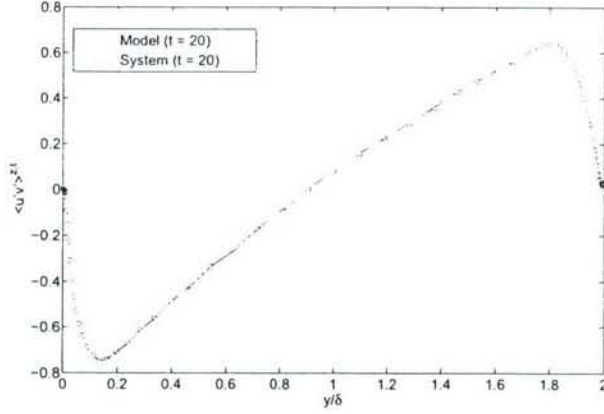


Figure 35: Comparison of the output of the linear model with the output of the system.

In the current work, the previous section described the problem with root locus analysis of the linear model, wherein it becomes impossible to correctly define the region of stability so that the threshold of stability of the linear model matches with the region of stability of the non-linear system. One of the ways to ameliorate this situation is to ensure that the root locus analysis yields simpler paths, that can facilitate a more straightforward analysis by reducing the order of the data collected during the system identification step. The application of POD to reduce the order of the linear model is described in detail below. The following set of equations show the derivation of the dynamic matrices A and B using the linear model.

$$X = [A \ B] [X_s \ \eta]^T \quad (61)$$

$$X [X_s \ \eta] = [A \ B] [X_s \ \eta]^T [X_s \ \eta] \quad (62)$$

$$[A \ B] = X [X_s \ \eta] \left([X_s \ \eta]^T [X_s \ \eta] \right)^{-1} \quad (63)$$

From the above equations, matrices X and X_s contain the data recorded during the system identification step. The first step is to transform the given data sets X and X_s into alternative data sets of smaller dimensions. The method of Sirovitch is used to calculate the POD basis vectors. Accordingly, matrices B and B_s are formed using X and X_s in the following way:

$$B = X^T X \quad (64)$$

$$B_s = X_s^T X_s \quad (65)$$

Next, the eigenvalues and eigenvectors of the matrices B and B_s are obtained. The eigenvector corresponding to the highest eigenvalue is used to calculate the POD basis vector. If y and y_s denote the eigenvectors corresponding to the highest eigenvalues, the POD basis vectors are calculated as,

$$V = X y \quad (66)$$

$$V_s = X_s y_s \quad (67)$$

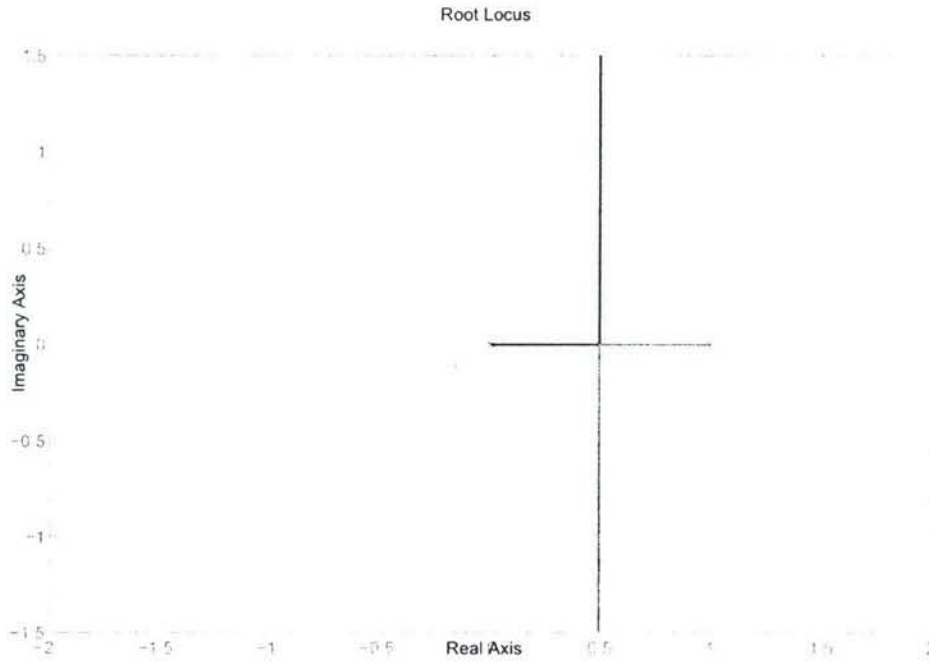


Figure 36: Root locus plot using the reduced order data. In this diagram, x represents the poles of the system.

The new data set that is of reduced order is recalculated as,

$$X_{new} = V^T X \tag{68}$$

$$X_{s,new} = V_s^T X_s \tag{69}$$

The new data set of reduced order can then be used to calculate the dynamic matrices A and B accordingly. Figure 36 shows the root locus plot made with the reduced order data. In this case the order of the data has been reduced to 1, since the eigenvector that corresponds to the highest eigenvalue has been retained in the data set. The reduction of order can be also accomplished by considering a few of the eigenvectors that correspond to the largest eigenvalues. In this case, a single eigenvector corresponding to the largest eigenvalue was retained. To close the loop a pole is placed at $z = 1$. It is now seen that there are two poles for the linear model in figure 36, one pole at the center of the unit circle and the second pole corresponding to $z = 1$. With such a pole distribution, the root locus remains within the unit circle for a longer time, resulting in higher gain values. It was found however, that the gain values thus obtained are too high and do not ensure the stability of the non-linear system.

5.5.5 Method based on non-linear system response

During the next stages of the investigation, the response of the non-linear system to preset gain values was measured during a precursor simulation. In the precursor simulation, gain values are increased starting from zero until there are numerical instabilities. The gain values are increased on the basis of a parameter ϕ that is related to the response of the system where ϕ is defined by (70),

$$\phi(t) = \frac{1}{M} \sum_1^M \left| \frac{\bar{y}_{t,M} - \bar{y}_{t-N,M}}{\bar{y}_{t-N,M}} \right|, \quad \bar{y}_t = \frac{1}{N} \sum_1^N \langle u'v' \rangle^{z,t} \quad (70)$$

The parameter $\phi(t)$ is measured at each control plane. The controller gain is increased only when $\phi(t)$ is less than a threshold (5%), set to ensure numerical stability. This approach determines optimal gain values for each control plane and is similar to a root locus method for a non-linear system since the gain values ensure stability of the system based on the response to the actual inputs. To ensure the accuracy of the gains predicted using this approach, the gain values must be increased in small increments. In the above formulation, the parameter M refers to the number of points in the wall-normal direction at which the control force is applied. Since the method is based upon the frequency of the response measured via the parameter $\phi(t)$, and the gains are incremented only when the response has a low frequency, N is a parameter similar to a time-averaging window and was set to a value of 100 in the simulations conducted. With the increment set to 10^{-6} , the simulation takes approximately 15 time units to determine the optimal gain values. Despite the use of the small increment, the method was not found to be successful in ensuring the stability of the system. This necessitated a deeper study of the errors during the control process to possibly arrive at simpler alternatives and possibly eliminate the necessity of a precursor simulation.

5.5.6 Difference between PI controllers and integral controllers

Here, results that show that a purely integrator based controller is as effective as a PI controller in increasing the resolved stress to target levels are presented. The results shown below confirm this conclusion, by comparing the effect of a controller using the integrator only with other controllers using different values of K_p .

Various values were used for the proportional and integral gain in a number of simulations conducted to assess the effect of these parameters on the system. Figure 37 shows plots that indicate the effect of K_p and K_I on the resolved stress values at the third control plane after two time units. Both plots indicate that the controller is effective even if $K_p = 0$ with a purely integral controller acting on the system. The figures also show that the simulations with smaller values of K_I exhibit the slowest response. These findings indicate that a purely integrator-based controller would suffice for this system, obviating the need to choose two constants (K_p and K_I). From a consideration of steady-state operation only, integrator-based control systems are preferable to proportional

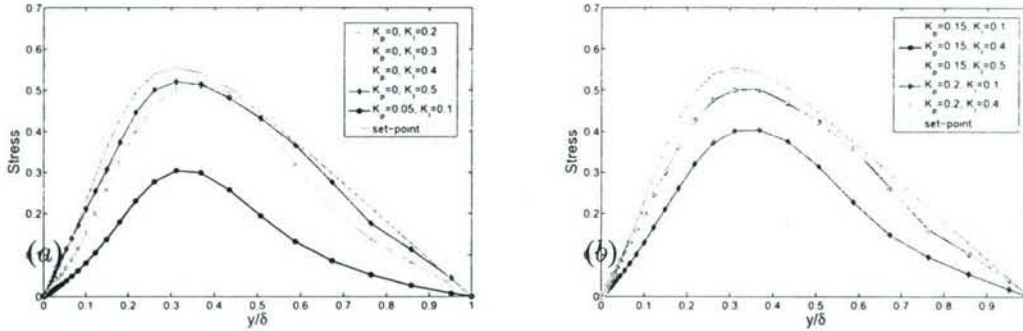


Figure 37: Resolved stresses at the third control plane for various values of K_P and K_I .

systems. However, it is generally easier to achieve good transient behavior (lower standard deviation of the error about a mean) with a proportional-based control system than an integrator-based control system. The action of a proportional plus integral controller in response to a change in the input or external disturbance is initially similar to that of a proportional controller, but as the new equilibrium point is reached, the control action becomes the same as that of an integral controller. A proportional plus integral controller combines the desirable transient characteristics of a proportional controller and the feature of no steady-state error. From the point of view of eliminating the mean error in the simulation, an integral controller is sufficient in achieving the desired result.

5.5.7 Characterization of the terms contributing to the error

Figure 38a,b,c and d show the effect of various values of the proportional and integral gains on the time histories of the mean of the error 52 obtained at various wall-normal locations. The simulations were performed with a fixed inlet condition obtained from a RANS solution at the corresponding Reynolds number. The boundary layer stirring force $f_{s,i}$ is then applied at a single stirring plane ($x/\delta = 1.0$). The simulation featured the use of three control planes. Note that these plots have been obtained using data from the third control plane of the simulations in a simulation conducted at a Reynolds number of 5000 and with the single stirring plane spaced 0.2δ upstream of the first control plane. The four locations shown correspond to $y/\delta = 0.0321$ ($y^+ = 160$), $y/\delta = 0.1344$ ($y^+ = 672$), $y/\delta = 0.3383$ ($y^+ = 1692$), and $y/\delta = 0.7177$ ($y^+ = 3589$). The figures show that as time increases, the mean of the errors goes towards zero at all of the locations. In the cases with $K_P = 0$ (Figures 38b and c), it can be seen that the mean error at locations corresponding to $y/\delta = 0.3383$ and $y/\delta = 0.1344$ hardly decrease at the start of the simulation, up to a time of approximately 0.5 – 1.0 units, and then decrease rapidly tending towards zero as time increases. In contrast, the cases with the proportional and integral terms contributing to the error show steady reduction in the mean values of the error over time beginning from the start of the simulation.

Figure 39 shows the error histories at the third control plane at two wall-normal locations corresponding to $y/\delta = 0.1344$ and $y/\delta = 0.3383$. As shown in the figure, the local errors are of higher magnitude when a purely integral controller is used. Despite this, the errors at these locations have a zero mean which eventually ensure that the resolved stresses reach the target values and also ensure that the quantity r does not increase in magnitude as time increases. Figure 40 shows the comparison of the rate of reduction of the mean of the error for all simulations at the same two locations. Figure 40a shows that there are no marked differences in rate of reduction of the mean of the error for all the simulations. Figure 40b shows that the addition of the proportional term affects the rate of reduction of the error at the start of the simulation, but as the simulation proceeds, the rate of reduction of the errors is almost the same for all the cases shown.

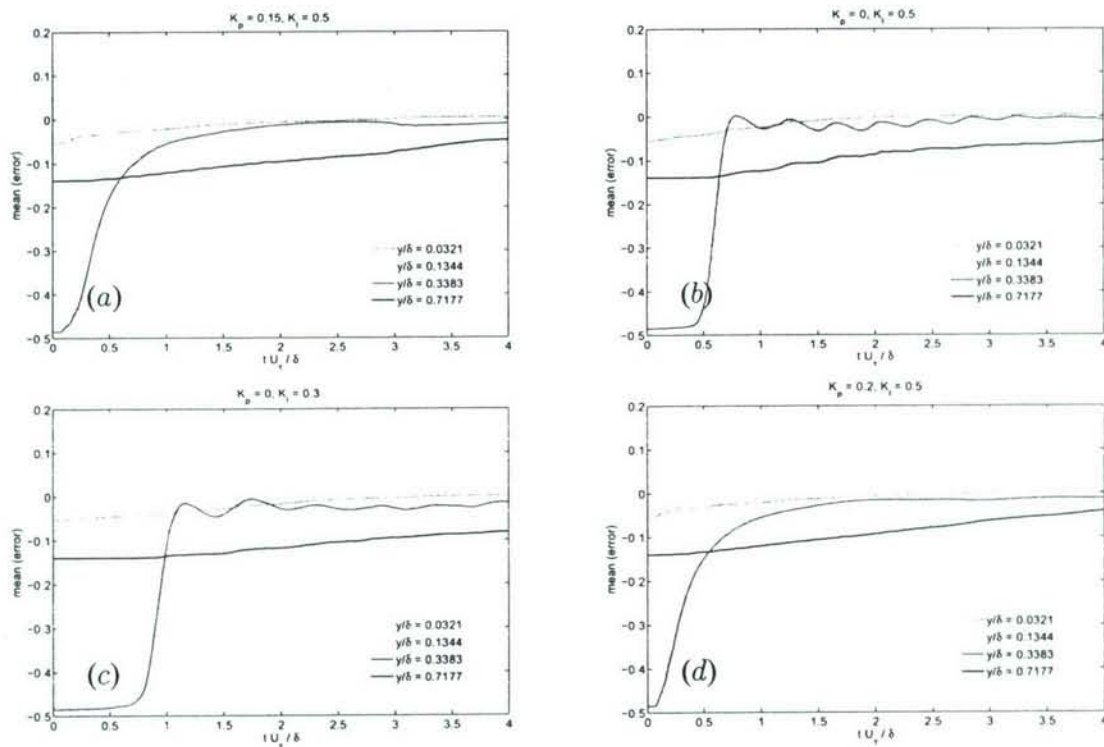


Figure 38: Mean values of the error over time at various wall-normal locations at the third control plane.

With an integral controller, whenever the error has higher frequencies, the sum of the error may not take this into account, especially when the sum of the errors is very large due to a long period of low frequency errors. At the initiation of the simulation, the error is more or less constant and shows low frequency content due to which the sum of the errors increases monotonically. When the sum of the errors becomes sufficiently large, the errors begin to decrease and the resolved stress moves towards the set point. With larger values of the integral gain, K_I , the term r becomes larger during the initial stages of the simulation, resulting in a larger overshoot of the resolved stress

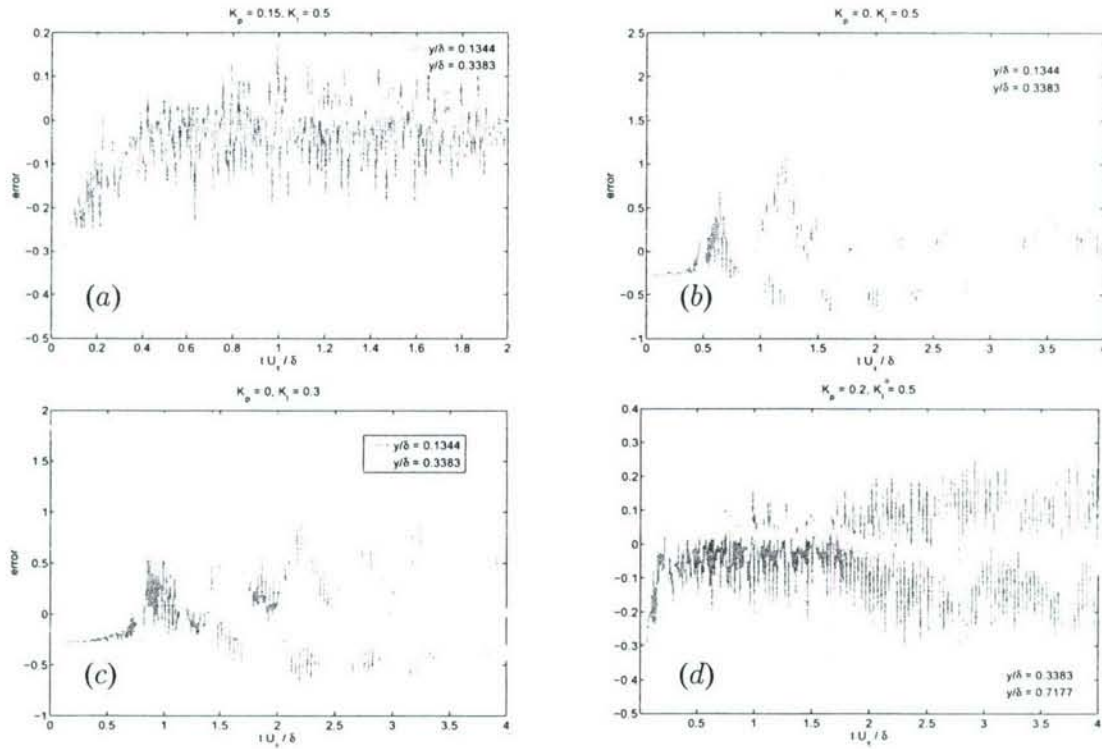


Figure 39: Error histories at the wall-normal locations $y/\delta = 0.3383$ and $y/\delta = 0.1344$ at the third control plane.

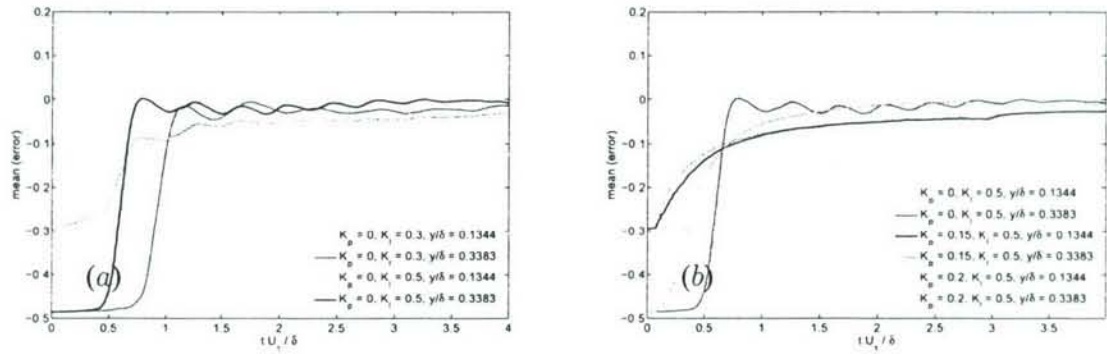


Figure 40: (a) and (b) Comparison of the rate of reduction of the mean error over time at wall-normal locations corresponding to $y/\delta = 0.1344$ and $y/\delta = 0.3383$ at the third control plane.

when the error reaches zero for the first time. In that sense, the selection of an appropriate value for the integral gain is important as a very large increase in the error may produce large variations in the instantaneous shear stress which is undesirable. However, the action of the integral controller ensures that the error reduces subsequently and moves in the opposite direction. This behavior repeats and results in error histories that are characterized by large modulations in the error for a very short period of time, followed by long periods of low frequency errors. Despite this behavior, the average error goes to zero after some time and undesirable transient effects (primarily on the wall shear stress) can be avoided by the use of smaller values of integral gains (typically values ranging from 0.2 to 0.5 yielded the desired results). From this perspective, an integral controller is sufficient to provide the desired results although the gain values need to be selected carefully. With the use of a PI controller, the r term attains large values at the beginning of a simulation. The higher frequency components of the error are taken into account in determining the control force due to the presence of the proportional term. The integral term is still present to account for the low frequency components of the error. The value of K_P plays a role in reducing the high amplitude modulations of the error that occurs when an integral controller is used. The main differences in the error histories of the PI controller and integral controller are contrasted in Figure 41 which considers the error histories at all three control planes for two simulations with the same integral gain of $K_I = 0.5$ and $K_P = 0.02$. Note that these simulations were carried out at a Reynolds number $Re_\tau = 5000$ and with a single stirring plane and three controllers spaced 0.5δ apart. The errors at wall-normal locations corresponding to $y/\delta = 0.1344$ ($y^+ = 672$) and $y/\delta = 0.3383$ ($y^+ = 1692$) are shown in the figure. The response of the system shows smaller overshoots when PI controllers are used. The use of integral controllers requires the selection of just a single parameter - the integral gain and is therefore advantageous.

Further investigations that were conducted to understand the behavior of the error at the control planes included:

- Effect of the stirring profile on the error histories. With a modified stirring profile (c.f., Figure 55) the histories of the error and the quantity r showed no changes in terms of behavior (in terms of the history of the errors over time). Note that for the comparison, the simulations were conducted with values of K_P and K_I corresponding to 0.2 and 0.5 respectively.
- Effect of the spacing between the end of the stirring region and the first control plane on the error histories. With the increase in the streamwise distance between the end of the stirring region and the first control plane to δ , the error histories at the control planes did now show any marked differences when compared with the cases with 0.2δ streamwise distance between the end of the stirring region and first control plane.

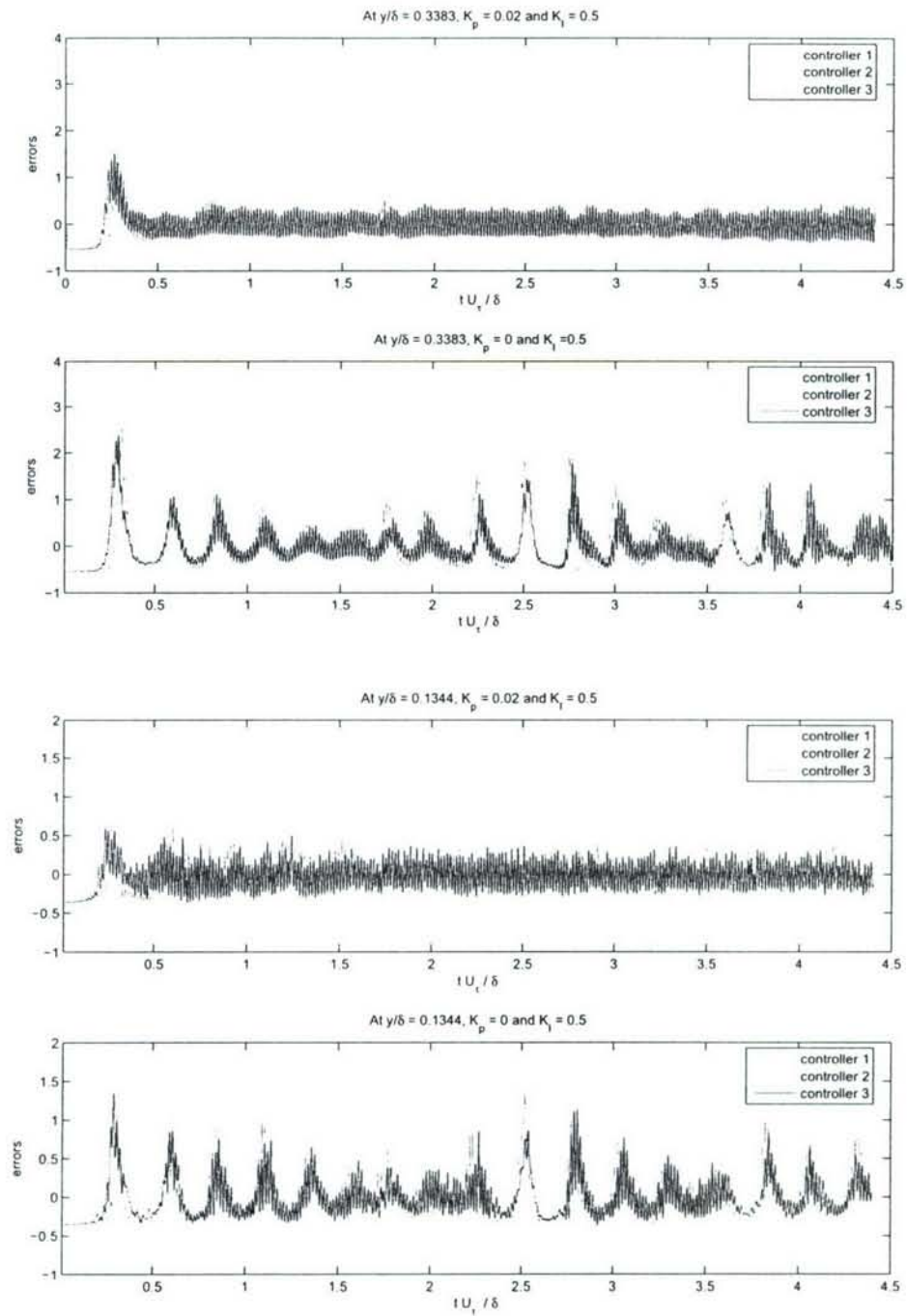


Figure 41: Comparison of error histories at two wall-normal locations at all three control planes when PI controllers and integral controllers are used.

5.5.8 Non-linear PI controller

The amplitudes of the error modulations can also be reduced by using a non-linear PI controller with the proportional gain K_P given by the rate of change of error (de/dt). This is based on the premise that when the error has a low frequency (and is not changing much), the integral term is sufficient to provide the desired control as $de/dt = 0$. When the error exhibits a high frequency, de/dt can be large, depending upon the frequency, resulting in greater proportional action that dominates over the integral action. This non-linear controller can be interpreted as a hybrid between a PI controller and an Integral-Differential (ID) controller, as the formula that expresses the control action can be written as:

$$r(t) = K_I \int_0^t e dt + e \frac{de}{dt} \quad (71)$$

When $de/dt = \text{constant}$, the controller behaves as a PI controller and when e is nearly constant, the controller becomes an approximation of a ID controller. When e is exactly equal to a constant, the controller behaves as an integral controller.

In this way, one could obtain a significant (i.e., different from zero) control action when the error is nonzero and when there are high frequency oscillations of the error. Furthermore, if one examines the term $e(de/dt)$, it is apparent that the amplitude of the control action always varies in a way that prevents the controller gain from becoming infinite. Figure 42 shows the reduction in the amplitude of the error modulations at the wall-normal location, $y/\delta = 0.3383$, due to the incorporation of the proportional gain $K_P = de/dt$. Subsequent simulations were carried out to determine the sensitivity of the choice of K_P on the errors. In these simulations, values of K_P corresponding to $2de/dt$, $4de/dt$ and $8de/dt$ were used. Figure 43 shows the comparison of the error histories at a wall-normal location corresponding to $y/\delta = 0.3383$ for two cases with $K_P = 2de/dt$ and $K_P = de/dt$. With $K_P = 2de/dt$, the amplitude of the error modulations are slightly smaller. Figure 44 shows a similar comparison for two cases with $K_P = 4de/dt$ and $K_P = 8de/dt$. With $K_P = 8de/dt$, the amplitude of the error modulations are the smallest. These cases serve to illustrate that the choice of the factor that multiplies de/dt is not critical especially in the absence of any special advantage in reducing the amplitude of the error modulations further.

5.5.9 Effect of time-averaging in the control formulation

Equation (52) is used to calculate the error at each control plane. The equation shows that the error is the difference between the set-point and the average value of resolved shear stress. The type of averaging employed is a moving time-average and simulations were conducted to assess the effect of the width of the time-averaging envelope on the results. Simulations were conducted with $K_I = 0.5$ and the width of the time-averaging envelope varied from 1 timestep (no time-averaging)

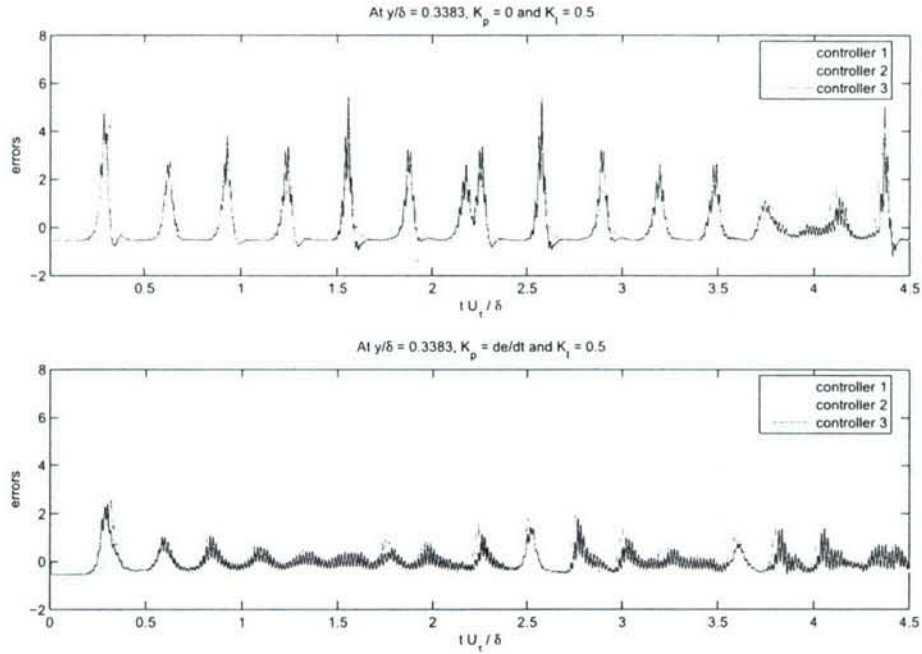


Figure 42: Reduction in the amplitude of the error modulations due to the action of the non-linear PI controller.

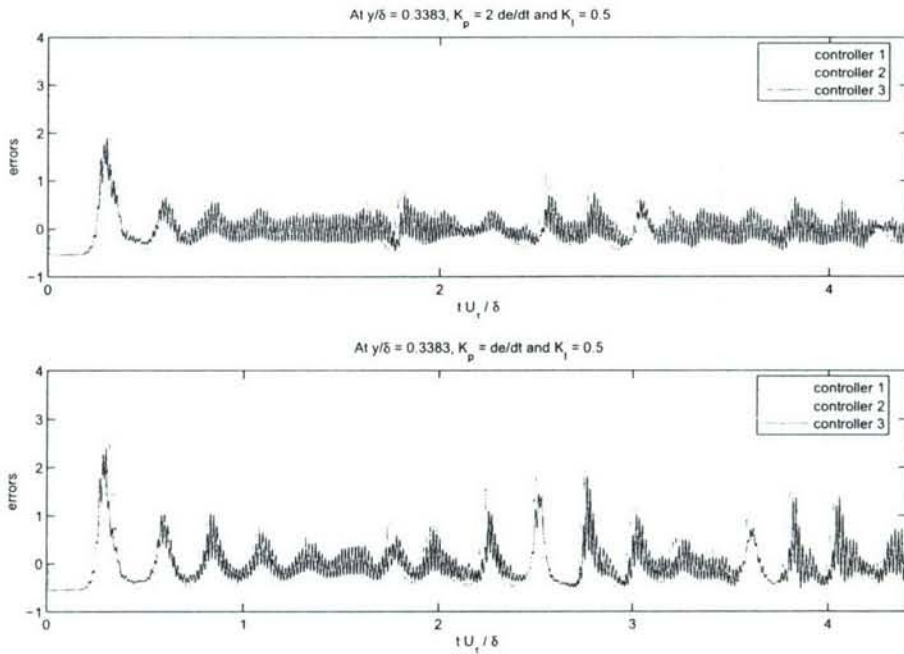


Figure 43: Comparison of the error histories for two cases corresponding to $K_P = 2de/dt$ and $K_I = 0.5$; $K_P = de/dt$ and $K_I = 0.5$.

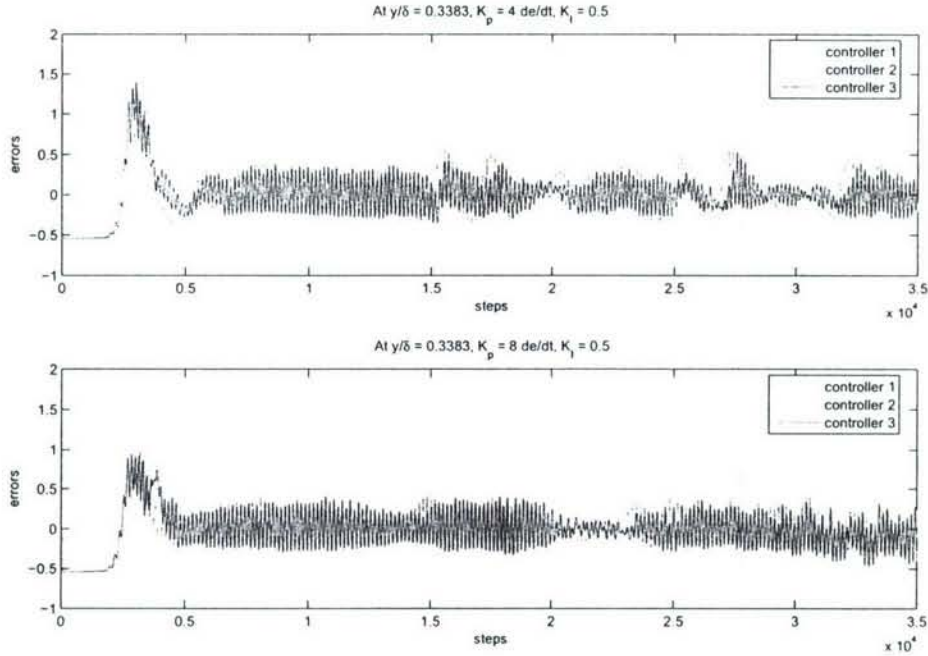


Figure 44: Comparison of the error histories for two cases corresponding to $K_P = 4de/dt$ and $K_I = 0.5$; $K_P = 8de/dt$ and $K_I = 0.5$.

to 200 timesteps (corresponding to 0.05 time units). Plots of the Power Spectral Density (PSD) of the error signals were analysed to determine the effect of time-averaging on the frequency content seen by the Integrators.

Figure 45a shows the PSD of the error signal at a location of $y/\delta = 0.3383$ at the third control plane. The figure shows that an increase in the width of the time-averaging envelope results in a smaller peak frequency of the error seen by the Integrator. For example, with a time-averaging envelope of 0.05 time units, the highest frequency errors seen by the Integrator correspond to timescales in the flow of about 0.0333 time-units (approximately 133 timesteps). This implies that all fluctuations that correspond to smaller timescales are not seen by the Integrator and are attenuated as a result of the averaging process. However, with no time-averaging, the peak frequency of the error seen by the Integrator corresponds to a flow timescale of approximately 0.0077 time units (about 30 timesteps). Higher frequencies seen by the Integrator imply better control of the resolved shear stress. With the current value of Integrator gain of 0.5, increasing the width of the time-averaging envelope to 0.10 and 0.15 time units resulted in numerical instabilities. Simulations were also conducted with $K_I = 0.1$ and with larger time-averaging envelopes of 1000, 2000 and 3000 steps (corresponding to 0.25, 0.5 and 0.75 time units). Figure 45b shows a PSD plot of the errors at a wall-normal location of $y/\delta = 0.3383$ at the third control plane. The peak frequency of the error seen by the Integrator corresponds to timescales in the flow of about 0.0667 time units

(about 265 timesteps). This implies that for errors over all scales of the flow that have a timescale lower than 0.0667 time-units are not taken into consideration by the Integrator and are attenuated.

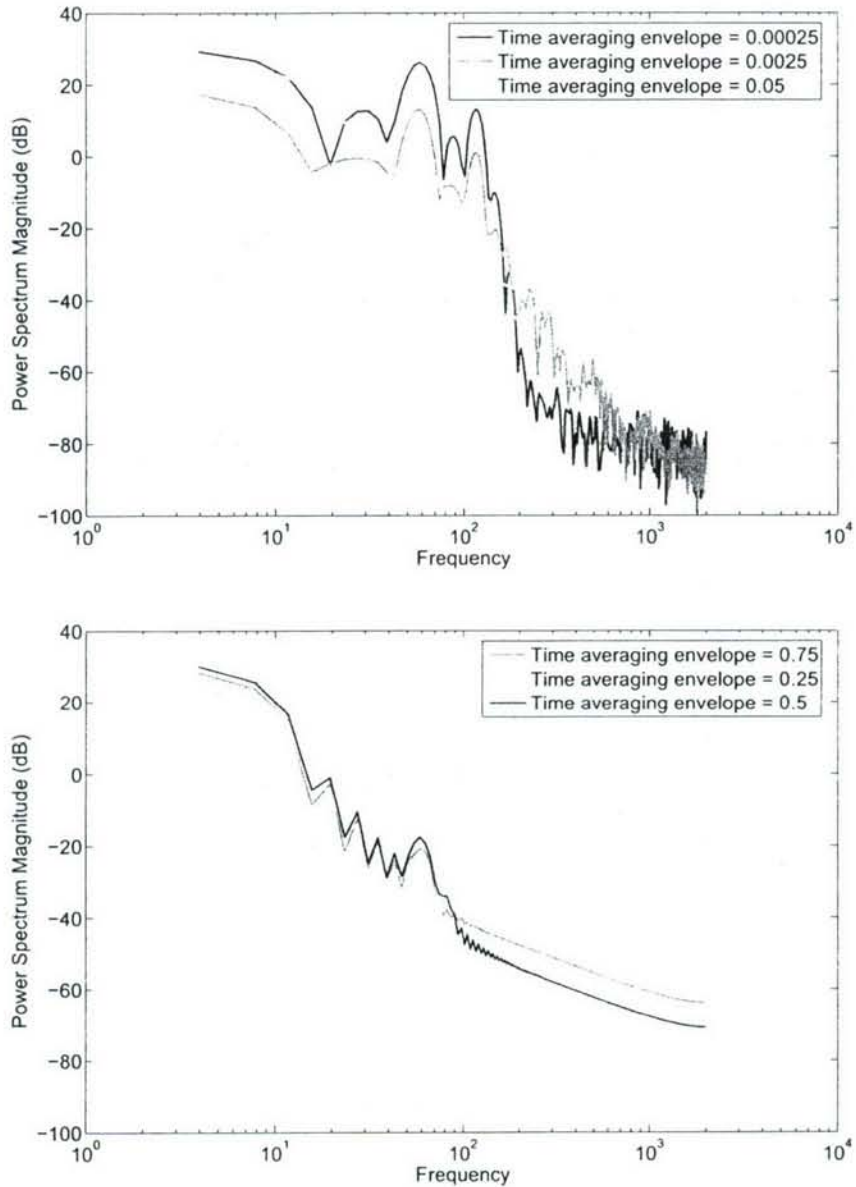


Figure 45: Power spectra of the errors with different averaging envelopes.

5.5.10 Adaptive control methodology to specify the controller gains

The previous simulations described until now showed the absence of major differences whether a PI controller or an integral controller is used, provided the integral gain is selected carefully. To further improve the selection methodology, integral controllers were used with the gain being

varied adaptively during the simulation. Initial investigations of the adaptive control methodology were carried out with the gain being varied at each wall-normal location based on the error at the wall-normal location. The formulation used for the control input is,

$$r = K_I \int_0^t edt \quad (72)$$

$$K_{I,t+1} = K_{I,t} - edt \quad (73)$$

$$K_{I,t+1} = K_{I,t} + edt \quad (74)$$

The sign of the error plays an important role in determining the gain values in the above equations. At the initiation of the simulation, for the bottom half of the channel, the error is negative (target resolved shear stress value is negative). Equation (73) is used in this case while (74) is used for the upper half of the channel. At the start of the simulation, the error is large due to which the gain increases by larger amounts. As the error starts decreasing due to the action of the integral controller, the increase in gains become smaller. When the error reaches zero and there is an overshoot, the gain begins to reduce. The initial value of the gain is the only choice made prior to the simulation. Figure 46 shows the error histories at wall-normal locations corresponding to $y/\delta = 0.1344$ and $y/\delta = 0.3383$ using the adaptive control methodology with an initial value of $K_I = 0.2$.

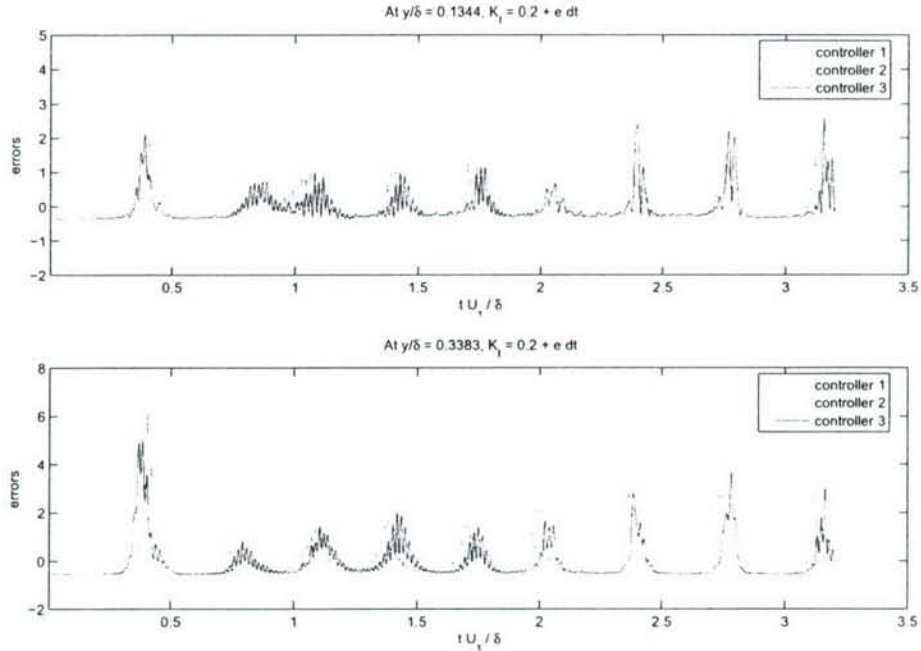


Figure 46: Error histories at two wall-normal locations using the adaptive control methodology with $K_I = 0.2$

A more standard form of an adaptive controller can be used which is described below. The gain is varied at each wall-normal location based on the error at the corresponding location. The method is based on the MIT rule which is an adaptive control methodology proposed by Whitaker (75). The formulation used for the control input consists of a cost function, defined below in (75). The integral gain is calculated using (76), with the system in open-loop at the start of the simulation ($K_I = 0$).

In (77), in order to prevent the gains from becoming too large, a modification is introduced with the gain being calculated from (78) every time the value of the term $|de/dK_{I_{n-1}}|$ is larger than unity. It must be noted that the sign preceding η is negative only for the lower half of the channel. For the upper half of the channel, the sign preceding η is positive. These modifications have been made to ensure that the gain of the system increases in the positive direction from the start of the simulation. During the simulation, by virtue of the values of the resolved shear stress and errors at the control planes, if the gains become negative, the gain values are set to zero so that the system gain values are always positive. In this method, the only choice to be made by the user in such a simulation is the value of η that ensures numerical stability.

$$C = \frac{1}{2} \sum e_n^2 \quad (75)$$

$$K_{I_n} = K_{I_{n-1}} - \eta \frac{dC}{dK_{I_{n-1}}} \quad (76)$$

$$K_{I_n} = K_{I_{n-1}} - \eta e_n \left| \frac{de_n}{dK_{I_{n-1}}} \right| \quad (77)$$

$$K_{I_n} = K_{I_{n-1}} - \eta dC \quad (78)$$

A few values of η were tested and the results are shown in Figure 47. Figure 47 shows the mean of the error at the last control plane at wall-normal locations corresponding to $y/\delta = 0.1344$ and $y/\delta = 0.3383$ using the adaptive control methodology for values of $\eta = 1, 3, \text{ and } 10$. The figure shows that the mean of the errors goes to zero faster starting from the system being in the open loop when $\eta = 10$. With the lower values of η , it can be seen that the mean of the errors moves very slowly towards zero. At larger values of η greater than 10, the change in the gain values at successive timesteps becomes too large resulting in the generation of numerical instabilities.

5.6 Flow visualizations

Figure 48 shows a comparison of the streamwise velocity contours at three wall-normal locations (corresponding to $y^+ = 161, 672 \text{ and } 1692$) for the fine grid case (consisting of $129 \times 75 \times 65$ points in the streamwise, wall-normal and spanwise directions respectively). Figures 49 shows

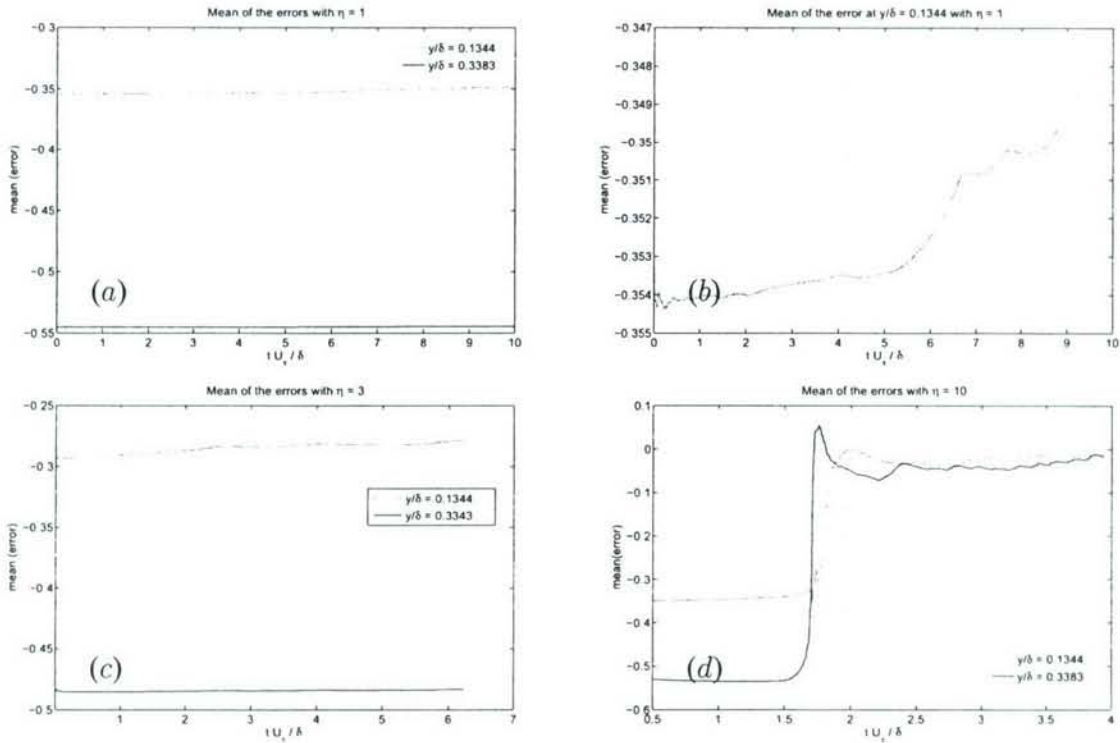


Figure 47: (a) Mean of the error at two wall-normal locations at the third control plane using the adaptive control methodology with $\eta = 1$; (b) Mean of the error at a wall-normal $y/\delta = 0.1344$ at the third control plane using the adaptive control methodology with $\eta = 1$ (Zoomed in view); (c) Mean of the error at two wall-normal locations at the third control plane using the adaptive control methodology with $\eta = 3$; (d) Mean of the error at two wall-normal locations at the third control plane using the adaptive control methodology with $\eta = 10$.

the contours of the spanwise velocity at the same three wall-normal locations. Figure 50 shows comparisons of the streamwise vorticity at three wall-normal locations (corresponding to $y^+ = 27$, 161 and 1692). All contours show evidence of turbulent structures downstream the control planes.

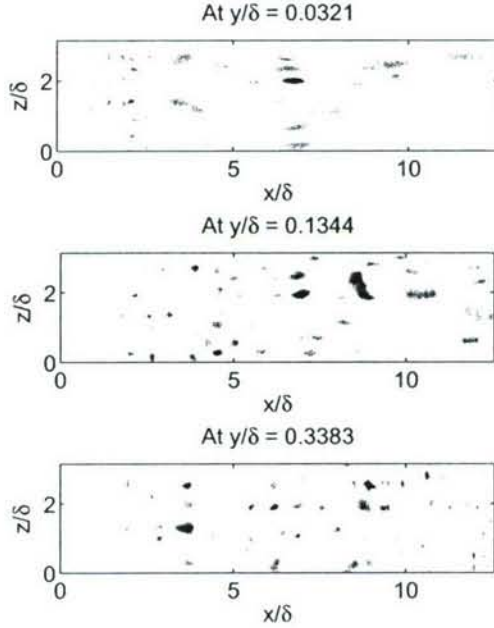


Figure 48: Streamwise velocity contours at wall-normal locations corresponding to $y/\delta = 0.0321$ ($y^+ = 161$), $y/\delta = 0.1344$ ($y^+=672$) and $y/\delta = 0.3383$ ($y^+ = 1692$).

5.7 Resolved stress and wall stress

Figure 51a shows the resolved shear stress at the last control plane from a simulation performed on a channel with a streamwise extent of 4π , with a single stirring plane at $x/\delta = 1.0$ and five controllers spaced δ apart. The simulation was performed on the fine grid consisting of $129 \times 75 \times 65$ points in the streamwise, wall-normal and spanwise directions respectively. The plot shows that the peak resolved shear stress reaches within 10% of the set point by about two time units. Figure 51b shows the resolved shear stress measured at streamwise locations 3δ and 5δ downstream the last control plane. It can be seen that the peak values of the resolved shear stress at these locations are very close to the peak resolved stress of the set point (target profile), even though the profiles seem to be shifted to the left with the peak resolved stress at the locations downstream occurring at a location corresponding to $y/\delta = 0.18$ as compared to a location of $y/\delta = 0.3$ in the target profile.

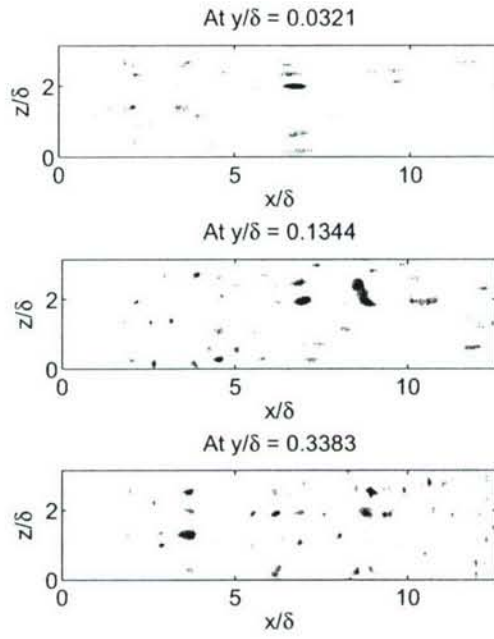


Figure 49: Spanwise velocity contours at wall-normal locations corresponding to $y/\delta = 0.0321$ ($y^+ = 161$), $y/\delta = 0.1344$ ($y^+ = 672$) and $y/\delta = 0.3383$ ($y^+ = 1692$).

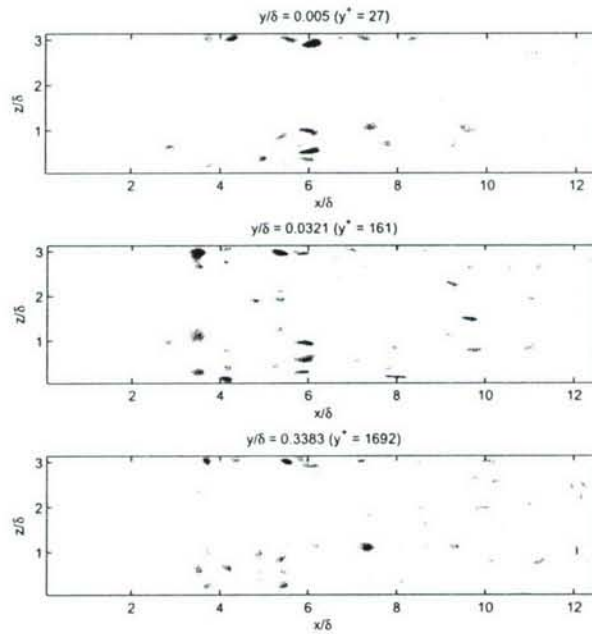


Figure 50: Streamwise vorticity contours at wall-normal locations corresponding to $y^+ = 27, 161$ and 1692.

Figure 51c shows the resolved shear stress measured at streamwise locations 3δ and 5δ downstream of the last control plane from a simulation conducted on the coarse grid consisting of $129 \times 75 \times 33$ points in the streamwise, wall-normal, and spanwise directions, respectively. As in the previous case, this simulation was performed on a channel with a streamwise extent of 4π and with a single stirring plane at $x/\delta = 1.0$ and five controllers δ apart. The plot shows that the peak values of the resolved shear stress at the locations 3δ and 5δ downstream of the last control plane are substantially less than the peak values of the resolved shear stress of the target profile by approximately 15% and 25%, respectively. This reduction in the peak values of the resolved shear stress downstream of the control plane imply an under-prediction in the wall stress.

Further investigations revealed that the under-prediction in the wall stress is a result of the use of grids with insufficient density and the number of control planes used for the simulation. Figure 52 shows a comparison of the wall shear stress for the coarse grid and fine grid cases (coarse grid consisting of $129 \times 75 \times 33$ points and fine grid consisting of $129 \times 75 \times 65$ points in the streamwise, wall-normal, and spanwise directions respectively). The channel was $4\pi\delta$ long in the streamwise direction and the stirring force was applied at a single plane, $x/\delta = 1.0$ for both simulations. The finer grid had 65 points in the spanwise direction, resulting in $\Delta_z = 0.0491$ (roughly 20 points per boundary layer thickness). In this way, the location of the RANS-LES interface for the finer grid is located at a distance of $y/\delta = 0.0318$, corresponding to a y^+ of approximately 160. The simulations were conducted at a Reynolds number of 5000. The figure shows that in the case of the fine grid, there is a good recovery of the wall shear stress to within 7 – 8% of the correct levels, with relatively small decreases in wall-shear stress downstream of the control planes. The coarse grid levels are low by about 20% close to the exit of the channel due to a steady decay in the wall stress as the flow moves downstream.

Figure 53 shows comparisons of the wall shear stress for three fine-grid cases with variations in the number of control planes and the spacing between them. All the runs were performed on a domain with a streamwise extent of 4π and a grid with 20 points per boundary layer thickness in the spanwise direction. It can be seen that with 5 controllers spaced $\delta/2$, the wall shear stress drops steadily downstream of the control planes with an error of approximately 11% at the exit of the domain. Despite the drop in the wall shear stress being less marked as the coarse grid result, it is an undesirable effect. With 5 controllers spaced δ or with 10 controllers spaced $\delta/2$, the reduction in the wall shear stress is lower with the error close to 8% at the exit of the domain. Figure 54 shows distributions of the resolved shear stress at locations 3δ and 5δ downstream of the last control plane. For the case with 5 controllers spaced $\delta/2$ apart, the peak values of the resolved shear stress are substantially lower than the peak value of the target profile indicating that there is a decay of turbulent content downstream of the control planes. The resolved shear stress for the other two cases (with 10 controllers spaced $\delta/2$ and 5 controllers spaced δ) do not show a substantial drop in the peak value as compared to the target profile and this translates to a better prediction of the wall

stress.

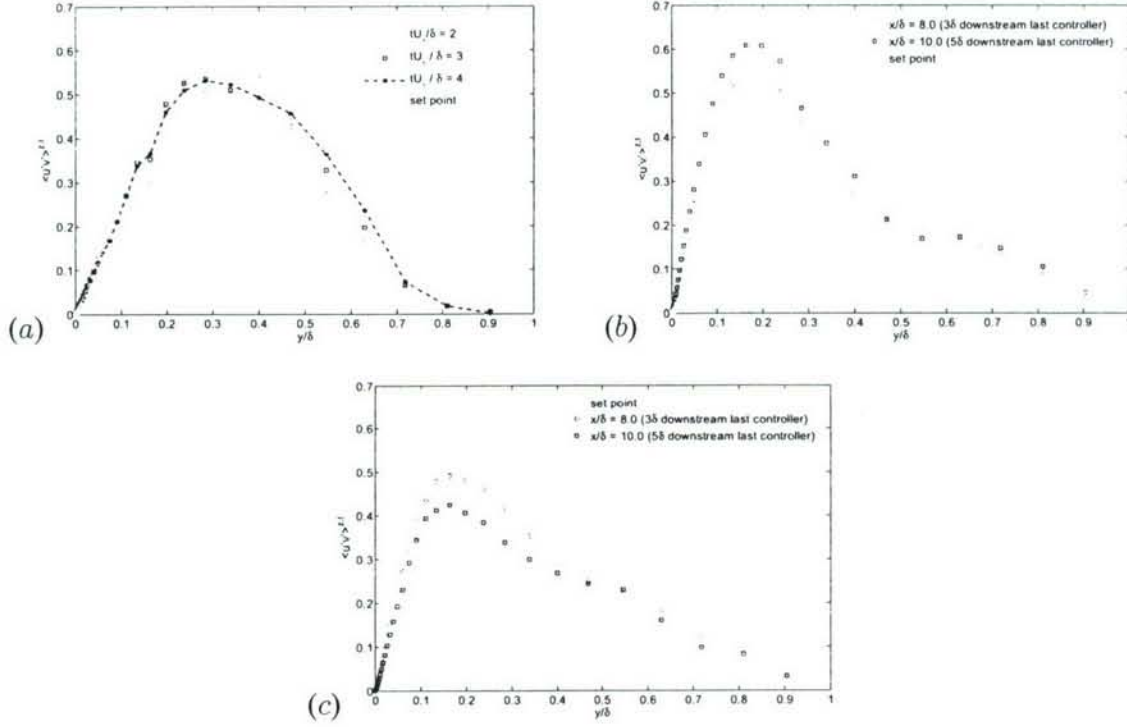


Figure 51: Resolved shear stress (a) with the fine grid ($129 \times 75 \times 65$ points in the streamwise, wall-normal and spanwise directions) at the last control plane; (b) with the fine grid ($129 \times 75 \times 65$ points in the streamwise, wall-normal and spanwise directions) at locations corresponding to 3δ and 5δ downstream the last control plane; (c) with the coarse grid ($129 \times 75 \times 33$ points in the streamwise, wall-normal and spanwise directions) at locations corresponding to 3δ and 5δ downstream the last control plane.

5.8 Influence of the stirring force

The influence of the stirring force on the control methodology was investigated using simulations performed at $Re_\tau = 400$. Computations were performed using different profiles for $f_{s,i}$, referred to as “scaling profile 1” and “scaling profile 2” in Figure 55. Scaling profile 2 was applied to distribute the force in the streamwise direction and the same profile with a magnitude half that used in the streamwise direction was employed to scale the wall-normal and spanwise components of the force. This anisotropic treatment was used since the streamwise fluctuations are larger than the wall-normal and spanwise components in boundary layers. The results obtained using scaling profile 2 are compared with those obtained using scaling profile 1 (with the same profile being applied in all three directions).

Figure 56 and Figure 57 show the rms levels of the velocity fluctuations at locations 1δ and 2δ

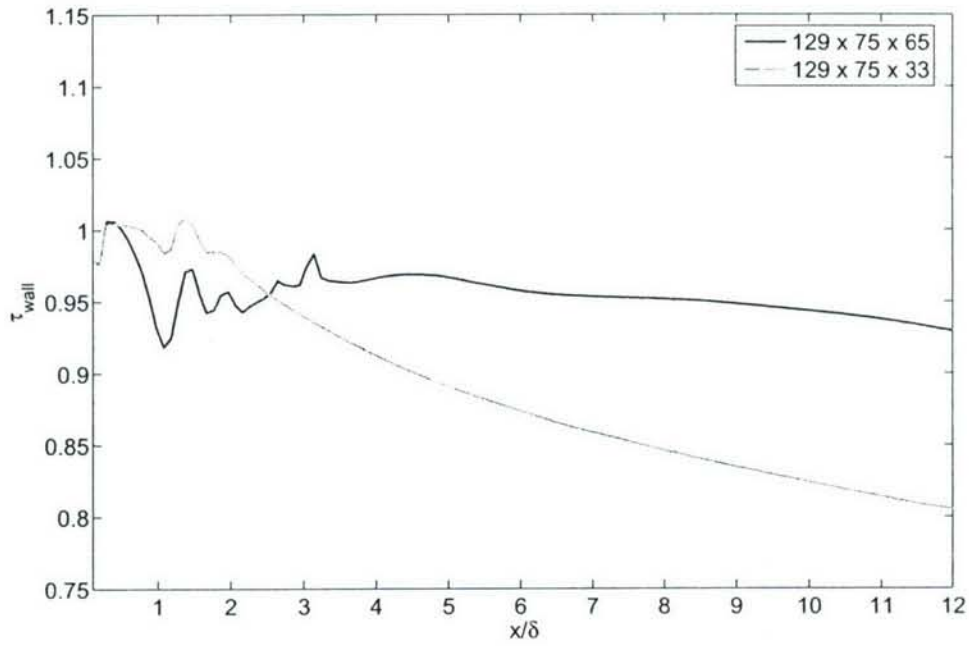


Figure 52: Comparison of the wall shear stress distribution for the coarse grid and fine grid cases.

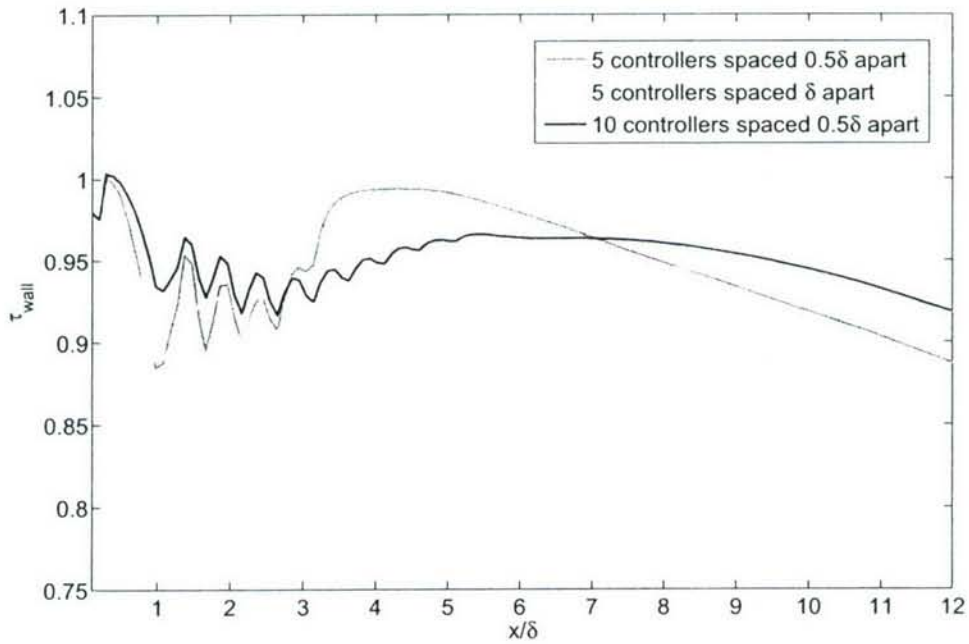


Figure 53: Comparison of the wall shear stress distribution for three cases with different number and placement of controllers using the fine grid.

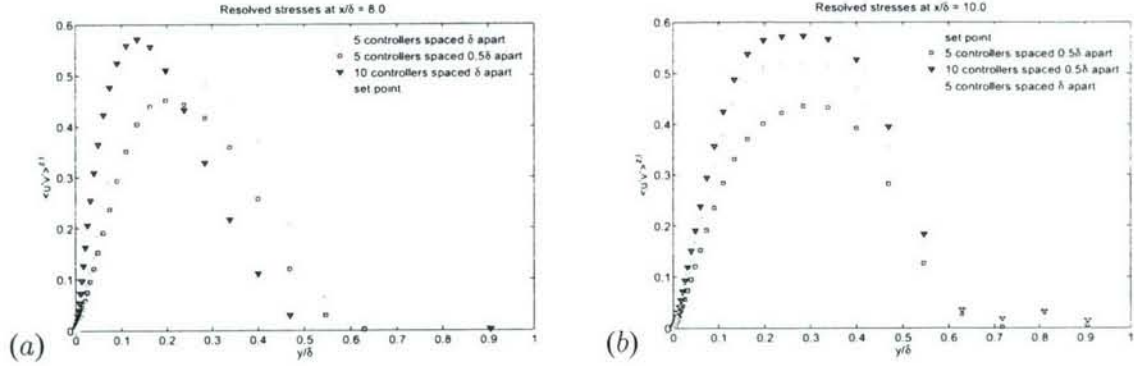


Figure 54: Resolved shear stress (a) with the fine grid ($129 \times 75 \times 65$ points in the streamwise, wall-normal and spanwise directions) at a location 3δ downstream the last control plane; (b) with the fine grid ($129 \times 75 \times 65$ points in the streamwise, wall-normal and spanwise directions) at a location 5δ downstream the last control plane.

downstream of the last controller using the two profiles. The figure shows that the velocity fluctuations in this case with stirring profile 2 exhibit better agreement with the rms velocity fluctuations from a fully-developed channel flow simulation at the same Reynolds number. This indicates that the form of the stirring force plays a role in ensuring that the flow downstream of the controller remains realistic.

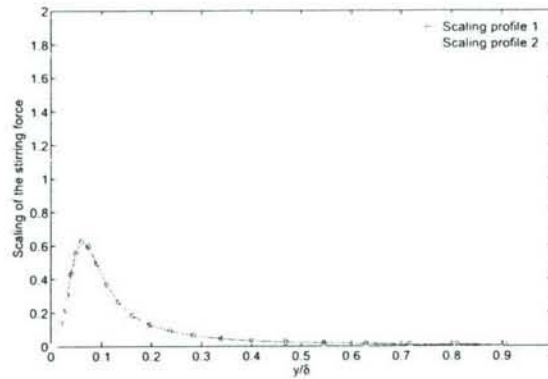


Figure 55: Scaling profiles of the stirring force.

5.9 Synthetic turbulence generation with controlled forcing

The synthetic turbulence generation method of Batten *et al.* (69) was investigated and used to provide a three-dimensional, unsteady velocity field at the inflow plane. The synthetic turbulence method was used at the inlet (instead of boundary layer stirring to generate three-dimensional content) along with controllers downstream, that amplify the fluctuations to obtain target resolved

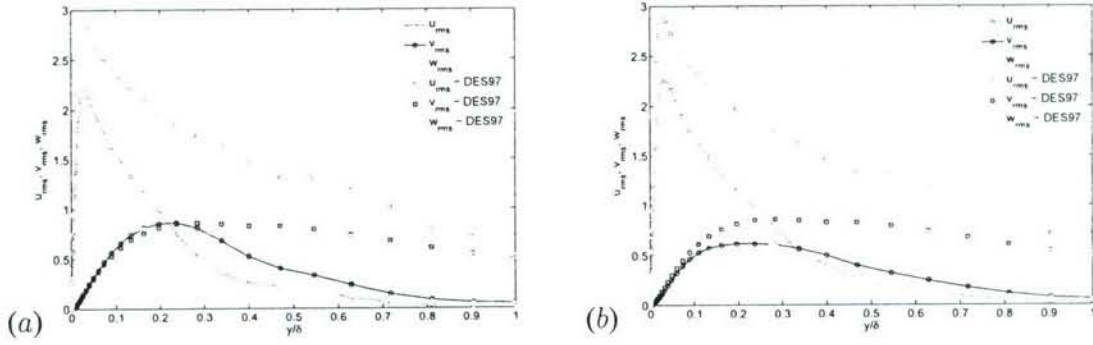


Figure 56: RMS velocities obtained using scaling profile 1 for the stirring force. (a) profiles 1δ downstream of the last controller; (b) profiles 2δ downstream of the last controller.

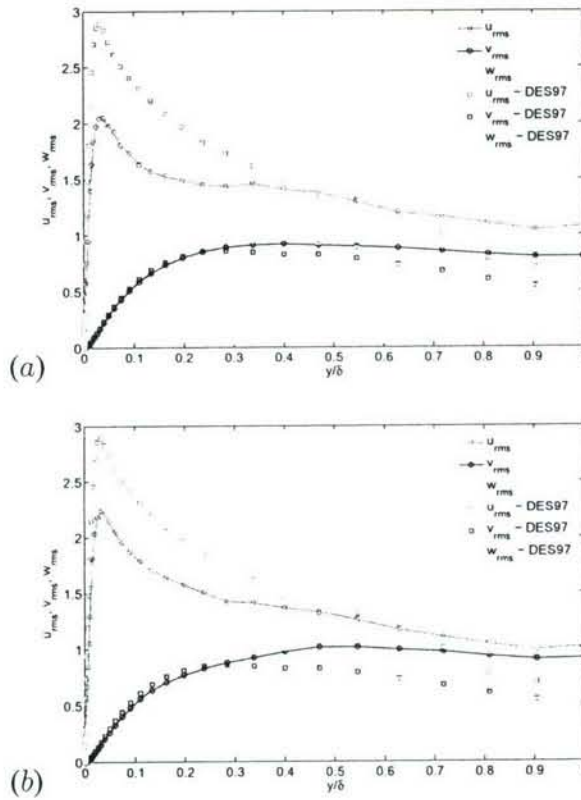


Figure 57: RMS velocities obtained using scaling profile 2 for the stirring force. (a) RMS velocities at a location corresponding to 1δ downstream of the last controller; (b) RMS velocities at a location corresponding to 2δ downstream of the last controller.

stress levels at the control planes. The results showed that synthetic turbulence was successful in generating fluctuations that are more realistic than boundary layer stirring, as a result of which the root mean square (rms) values of the velocities showed reasonable agreement with profiles from a

periodic simulation using DES97. The controllers still have a role to play, and help to ensure that the levels of resolved stresses reach the target levels quickly. Figure 58 shows the rms values of the streamwise velocity at various locations downstream of the inlet. Figure 59 shows the rms values of the wall-normal velocity at various streamwise locations downstream of the inlet. It can be seen that the profiles adjust themselves within $7 - 8\delta$ downstream of the inlet.

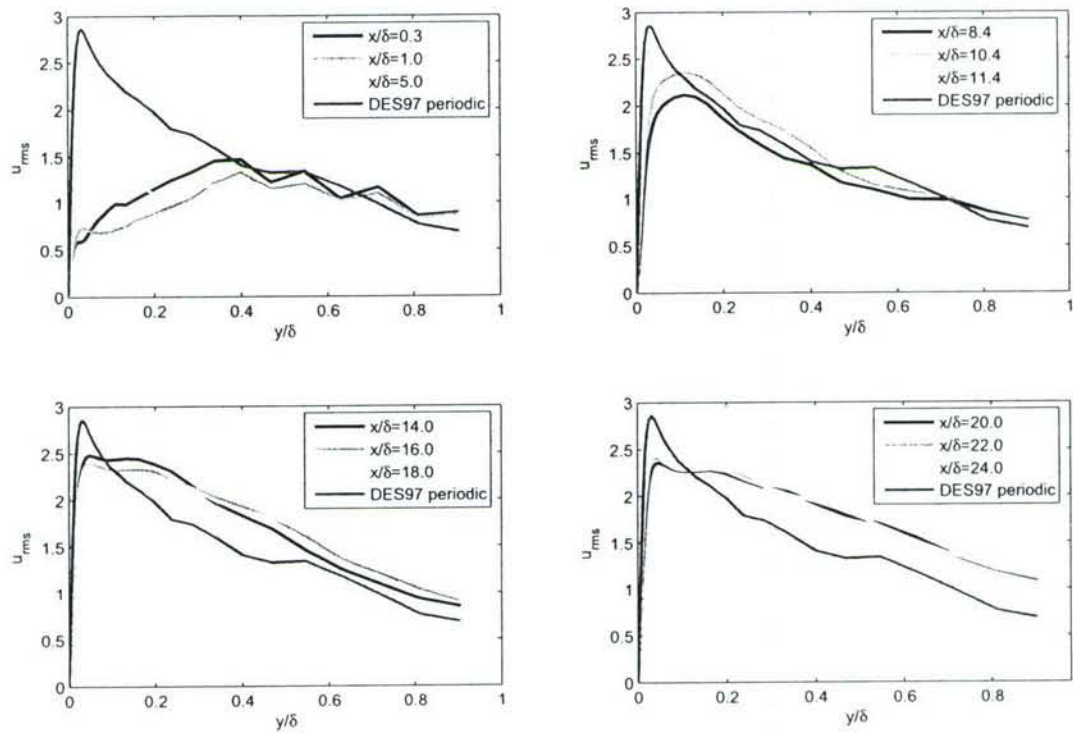


Figure 58: RMS values of the streamwise velocity at various streamwise locations (Synthetic turbulence with controlled forcing).

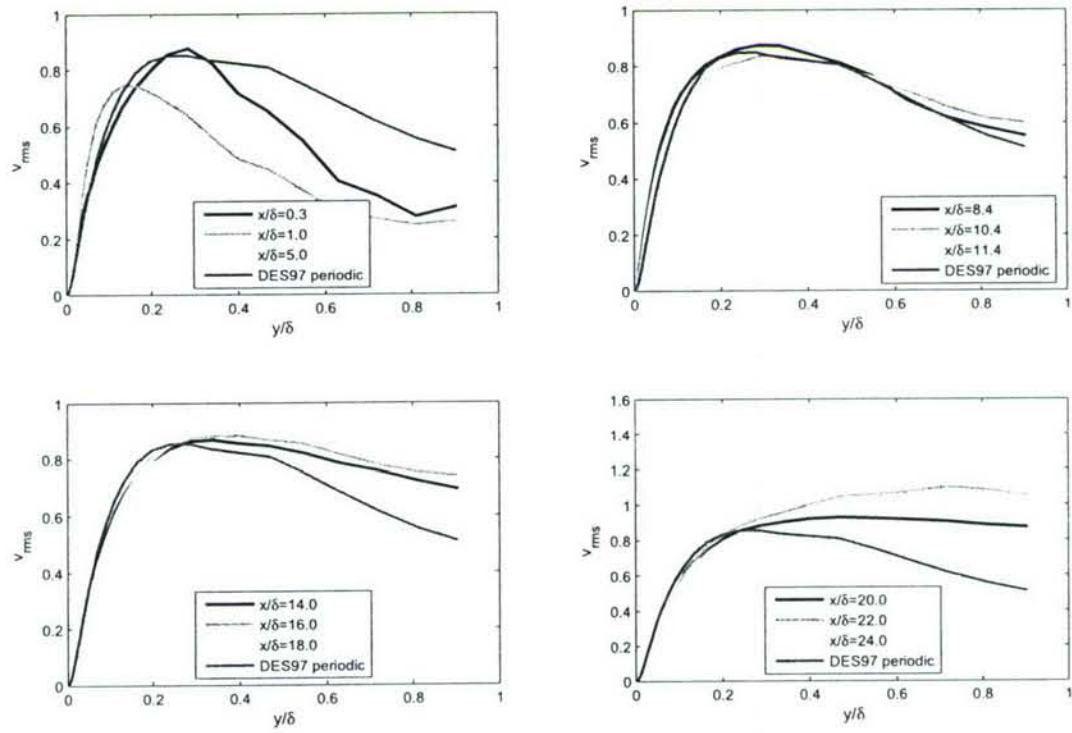


Figure 59: RMS values of the wall-normal velocity at various streamwise locations (Synthetic turbulence with controlled forcing).

6 Summary

Prediction of complex flows that include adverse pressure gradients, streamline curvature and boundary layer separation remain among the most challenging for turbulence simulation strategies. Among the various hierarchies of simulation strategies, RANS approaches remain the most widely applied simulation technique for complex flows. However, this approach often produces unsatisfactory results for flows far-removed from the thin shear layers used to calibrate the underlying RANS models. For example, significant effects of separation in flows that are massively separated are not easily predicted using RANS approaches. The strong reliance on empiricism has motivated intense development of other approaches that provide more robustness and fidelity. Strategies such as LES are attractive from the point of view that they minimize the empirical input in the models and are capable of generating solutions with rich turbulence physics. Despite this benefit, LES carries a prohibitive computational cost for resolving boundary layer turbulence at high Reynolds numbers with grid point estimates that scale as $Re^{1.8}$ (25). This provided a strong incentive to merge the two techniques in such a way that the advantages of both strategies are preserved. Among the most popular of all the hybrid RANS/LES techniques is DES (26) which has been actively applied to simulate complex flowfields with massive separation. Even though the method was initially proposed by Spalart *et al.* (26) as a numerically feasible strategy to predict massively separated flows, interest has been generated to extend the method to other classes of flows.

The use of DES to predict attached flows or flows with shallow separation is more challenging due to the difficulty in the generation and sustenance of instabilities. The over-arching goal of the investigations was to understand this aspect of DES and understand the method better so that it can be extended to all classes of flows. The initial stages of the project were focused on improving the overall understanding of DES for flows with thick boundary layers and/or shallow separation. It was found that finer grids in the streamwise and spanwise directions caused the RANS-LES interface to lie well within the boundary layer, leading to a reduction of modeled stresses in the RANS region of the simulation with resolved content lacking in the LES region due to insufficient grid densities in the LES region. This further led to a reduction in skin friction resulting in premature separation of the flow. The problems that occur in these regimes due to the use of ambiguous grids were eliminated by the use of DDES, the newer version of the model. The new version was used to simulate attached flow over a flat plate at a momentum thickness based Reynolds number of 9000. The new version was then tested on the flow over an Aerospatiale A-airfoil at an angle of attack of 13.3° and at a chord-based Reynolds number of $Re = 2.1 \times 10^6$. To ensure that the new version does not degrade predictions in massively separated flows, the flow over a circular cylinder at Reynolds numbers corresponding to 1.4×10^5 and 8×10^6 was also analyzed. These simulations reinforced the effectiveness of DDES in ensuring that RANS was maintained within the boundary

layer, leading to correct levels of modeled stresses in the hybrid simulation as compared to a RANS simulation.

Another important issue in the simulation of realistic flows using DES involves the generation of instabilities in a numerical simulation in flowfields that do not include any slope discontinuity (presence of slope discontinuities would lead to the quick growth of any generated instabilities). This becomes an important issue in simulations of spatially developing flows in a channel or a backward facing step, where the generation of inflow conditions that enable the growth and sustenance of turbulence is paramount. In the past, researchers have developed various methods of specifying inflow boundary conditions meant to be used in conjunction with wall-layer models for these flowfields. The current work provides a method to generate instabilities in the transition from a RANS treatment to an LES treatment along the main flow direction in a DES, which can result in applications due to streamwise grid refinement as necessitated by a change in geometry or by design into the grid the finer spacing needed to resolve fluctuations in the hopes of improving accuracy.

The main focus of the project involved the application of a controls-based methodology to develop velocity fluctuations for boundary layer simulations and testing of the methodology using DES of turbulent channel flow. The method employs a series of control planes in which a body force is applied to amplify velocity fluctuations seeded upstream. The control force is added to the wall-normal momentum equations at the control planes, based on a prescribed target profile for the resolved shear stress. The main focus of the present manuscript was the design of the controllers and simplifying the procedure. The design of controllers using a linear model was unsuccessful due to the inherent non-linearities of the system that ensured that the threshold of stability of the linear model did not match well with the region of stability of the non-linear system. The control methodology based on the measured response of the non-linear system was also found to be unsuccessful in predicting gain values that ensure numerical stability.

A deeper analysis of the behavior of the errors with the use of PI and integral controllers revealed that there are no specific performance advantages due to the use of PI controllers over integral controllers. The use of PI controllers involves the specification of two parameters - the Proportional gain (K_P) and the integral gain (K_I). Simulations conducted revealed that the specification of gains that ensure numerical stability was very subtle and complicated. Using integral controllers with the gain of the controllers increased adaptively is a simple alternative that ensures that the desired results are obtained. The adaptive control scheme developed and tested worked satisfactorily and yielded the desired results without the use of saturations to prevent the forces from being applied based on predefined criteria. The method was found to work satisfactorily with the resolved stress reaching target levels at the control planes, with the peak value of the resolved stress being within 10% of the peak value of the target profile at locations downstream of the control plane provided sufficient number of controllers and finer grids were used. With coarse grids,

there seemed to be a larger decay in the peak values of the resolved stress at locations even 2δ downstream the control plane. This also resulted in a large error of about 20% in the wall stress at the end of the domain (at a streamwise distance of 8δ from the last control plane). Subsequent simulations revealed that the decay of the resolved stress and wall stress downstream the control planes is largely dependent upon the mesh resolution used while applying the method. It was found that with 20 points per boundary layer thickness in the spanwise direction, the wall shear stress levels are within 8% of the RANS levels for a simulation with a domain streamwise extent of 4π and controllers occupying 30% of streamwise extent of the domain.

Appendix

Cobalt

Cobalt is a parallel, implicit, unstructured flow solver developed by the Computational Sciences Branch of the Air Force Research Laboratory. The algorithm of Cobalt is based on Godunov's first-order accurate, exact Riemann method (59). The solver is second order accurate temporally and spatially, and the time stepping is implicit. The solver adopts a cell-centered, finite-volume approach. Cobalt is compatible with grids of arbitrary cell shapes in two or three dimensions. Cobalt was chosen over other commercial codes, as it is compatible with both DES and URANS models. The computation of the flow solution consists of five fundamental tasks:

- Construction of initial conditions for the Riemann problem at any given face
- Solution of this Riemann problem
- Construction of viscous fluxes at any given face
- Time integration
- Boundary conditions

The Euler and Navier-Stokes equations are solved in an inertial frame of reference. The integral form of the equations are given below:

$$\frac{\partial}{\partial t} \int \int \int_V Q dV + \int \int_S (f\hat{i} + g\hat{j} + h\hat{k}) \cdot \hat{n} dS = \int \int_S (r\hat{i} + s\hat{j} + t\hat{k}) \cdot \hat{n} dS \quad (79)$$

where:

- V is the fluid element volume
- S is the fluid element surface area
- \hat{n} is the outward-pointing unit normal to S
- $\hat{i}, \hat{j}, \hat{k}$ are the Cartesian unit vectors

$$Q = \begin{bmatrix} \rho \\ \rho u \\ \rho v \\ \rho w \\ \rho e_t \end{bmatrix}$$

$$f = \begin{bmatrix} \rho u \\ (\rho u^2 + p) \\ \rho uv \\ \rho uw \\ u(\rho e_t + p) \end{bmatrix}$$

$$g = \begin{bmatrix} \rho v \\ \rho uv \\ (\rho v^2 + p) \\ \rho vw \\ v(\rho e_t + p) \end{bmatrix}$$

$$h = \begin{bmatrix} \rho w \\ \rho uw \\ \rho vw \\ (\rho w^2 + p) \\ w(\rho e_t + p) \end{bmatrix}$$

$$r = \begin{bmatrix} 0 \\ \tau_{xx} \\ \tau_{xy} \\ \tau_{xz} \\ u\tau_{xx} + v\tau_{xy} + w\tau_{xz} + kT_x \end{bmatrix}$$

$$s = \begin{bmatrix} 0 \\ \tau_{xy} \\ \tau_{yy} \\ \tau_{yz} \\ u\tau_{xy} + v\tau_{yy} + w\tau_{yz} + kT_y \end{bmatrix}$$

$$t = \begin{bmatrix} 0 \\ \tau_{zx} \\ \tau_{zy} \\ \tau_{zz} \\ u\tau_{zx} + v\tau_{zy} + w\tau_{zz} + kT_z \end{bmatrix}$$

where:

- ρ is the density
- p is the pressure
- u, v, w are the velocity components
- e is the specific energy per unit volume
- T is the temperature
- k is the thermal conductivity
- τ represents shear stress components

The ideal gas laws close the set of equations and the equations are non-dimensionalized by freestream density and speed of sound. The turbulence models are solved, decoupled from the main conservation equations and the semi-discrete form of the equations can be written as:

$$V_i \frac{dq_i}{dt} + \sum_{m=1}^{N_i} (f_m \hat{i} + g_m \hat{j} + h_m \hat{k}) \cdot \hat{n}_m S_m = \sum_{m=1}^{N_i} (r_m \hat{i} + s_m \hat{j} + t_m \hat{k}) \cdot \hat{n}_m S_m \quad (80)$$

where i and m denote quantities for the i^{th} cell and m^{th} face of cell i , respectively, and N_i is the number of faces bonding cell i .

The Riemann problem

Riemann problems and their solution procedure were first introduced into computational fluid dynamics by Godunov (60). A description of the Riemann problem for a non-stationary flows of a perfect gas is provided here. In this case, the state U of a perfect gas is specified completely by three dependent variables and two constants that are particular to the gas under consideration. The dependent variables are the pressure, density and flow velocity, while the constants are the ratio of the specific heats and the gas constant. It must be remembered that, all other state properties can be obtained from the aforesaid variables and constants. Considering two discrete initial states $U(x_i, t_j)$ and $U(x_{i+1}, t_j)$ at adjacent nodes at time level t_j in a numerical grid, the Riemann problem can be defined as:

$$U(x, t_j) = U_i[x < x_i + \Omega(x_i - x_{i+1})] \quad (81)$$

$$U(x, t_j) = U_{i+1}[x \geq x_i + \Omega(x_i - x_{i+1})] \quad (82)$$

where Ω is a number between 0 and 1 that fixes the location of discontinuity between these two states. Therefore, the initial data is piecewise constant, equalling $U(x_i, t_j)$ or $U(x_{i+1}, t_j)$ depending on the location of the discontinuity between the two nodes. With time, the discontinuity between the two initial states break into leftward and rightward moving waves, separated by a contact surface (this depends on the initial data, based on which a wave may either be a shock or a rarefaction). The available combinations produce four unique wave patterns which are self-similar, depending only on x/t . The problem of determining the types of waves, their strengths, and the flow properties in each region between the waves and contact surface for some particular set of initial data is called a Riemann problem, and the algorithm for determining the solution is called a Riemann Solver. Since this is a one-dimensional case, the pressure, density and velocity of the wave on either sides of the contact surface can be determined using the three conservation laws of mass, momentum and energy and the equation of state. The conservation laws reduce to the Rankine-Hugoniot relations for a shock wave and an isentropic characteristic equation across rarefaction waves. These equations are used to jump across the moving waves into the unknown state across the contact surface. By assuming that a single state exists between the waves on the left and right sides, the Riemann problem may be reduced to a single nonlinear algebraic equation in one unknown for any particular wave pattern. This equation is implicit in pressure or velocity and can be solved iteratively.

Riemann Solver of Gottlieb and Groth

An efficient Riemann solver will involve fewer mathematical operations for the entire solution procedure, inclusive of the initial guess, equations used in the iterative procedure, check used to stop the iterative procedure and additional expressions required to completely specify the states on both sides of the contact surface and the determination of the wave speeds. From experience, Gottlieb and Groth found that numerical computations are more efficient when the states at the grid nodes are defined by the variables (p, c, u, γ, R) instead of (p, ρ, u, γ, R) , as the speed of sound is a dependent variable which appears more frequently than the density in the equations (60). Instead of solving for the common pressure of the intermediate states (p^*), the common flow velocity of the intermediate states (u^*) is used to iterate in this Riemann solver, and the pressure difference ($p_l^* - p_r^*$) across the contact surface was made zero. Earlier flow solvers differ from the Riemann solver of Gottlieb and Groth, as they involved iteration with the variable p^* , which was detrimental to the computing efficiency. Newton's iterative procedure was used to determine the solution of the Riemann problem, successive iterates of u^* are given by:

$$u_{i+1}^* = u_i^* \frac{p_l^* u_i^* - p_r^* u_i^*}{p_l^{*'} u_i^{*'} - p_r^{*'} u_i^{*'}} \quad (83)$$

where the prime denotes differentiation with respect to u^* . Convergence is determined by satisfying the inequality $|1 - p_l^*/p_r^*| < \epsilon$, and the tolerance ϵ is usually 10^{-6} . Shock and rarefaction

equations yield p_l^* , p_r^* , c_l^* , c_r^* , dp_l^*/du^* and dp_r^*/du^* . The relevant equations in the case of a leftward moving shock wave ($u^* \leq u_1$) are:

$$W = \frac{\gamma_l + 1}{4} \frac{u^* - u_l}{c_l} - \left(1 + \left(\frac{\gamma_l + 1}{4} \frac{u^* - u_l}{c_l} \right)^2 \right)^{\frac{1}{2}} \quad (84)$$

$$p_l^* = p_l + C_l(u^* - u_l)W_l \quad (85)$$

$$p_l^{*'} = \frac{2C_l W_l^3}{(1 + W_l^2)} \quad (86)$$

$$c_l^* = c_l \sqrt{\frac{(\gamma_l + 1) + (\gamma_l - 1)p_l^*/p_l}{(\gamma_l + 1) + (\gamma_l - 1)p_l/p_l^*}} \quad (87)$$

where $C_l = \gamma_l p_l / c_l$ is computed before the start of the iterative process, and W_l is the shock Mach number with respect to the moving gas ahead of the shock. W_l is a by-product of the iterative process. The shock velocity is denoted as $u_l + c_l W_l$ in the laboratory reference frame. The variables c_l^* and V_l are not needed in the iterative process, and therefore are computed later. Similarly, we could write a set of equations for a right moving shock wave. For a left moving rarefaction wave ($u^* > u_1$), the relevant equations are:

$$c_l^* = c_l - \frac{\gamma_l - 1}{2}(u^* - u_l) \quad (88)$$

$$p_l^* = p_l \left(\frac{c_l^*}{c_l} \right)^{\frac{2\gamma_l}{\gamma_l - 1}} \quad (89)$$

$$p_l^{*'} = \gamma_l \frac{p_l^*}{c_l^*} \quad (90)$$

In this case, c_l^* is the by-product of the iterative procedure and the velocity of the expansion wave head is $u_l^* + c_l^*$. The initial guess for the flow velocity u_0^* is obtained by:

$$u_0^* = \frac{\bar{u}_l z + \bar{u}_r}{1 + z} \quad (91)$$

$$\bar{u}_l = u_l + \frac{2}{\gamma_l - 1} c_l \quad (92)$$

$$\bar{u}_r = u_r + \frac{2}{\gamma_r - 1} c_r \quad (93)$$

$$z = \frac{\gamma_l - 1}{\gamma_r - 1} \frac{a_r}{a_l} \left(\frac{p_l}{p_r} \right)^{\frac{\sigma - 1}{2\sigma}} \quad (94)$$

$$\sigma = \gamma_l(p_l \geq p_r) \quad (95)$$

$$\sigma = \gamma_r(p_l < p_r) \quad (96)$$

Glimm's method

Glimm's method is a method for constructing approximate solutions to systems of hyperbolic conservation laws by sampling explicit wave solutions (2). It is based on the idea of representing a piecewise continuous flow by a series of discontinuities. These waves propagate with different speeds and have different strengths. The discontinuities are modeled as a series of Riemann problems, separated by jumps. If the timestep is small, then by finite propagation speed, the waves from adjacent discontinuities do not intersect each other and the solutions to the adjacent Riemann problems fit together.

Initial conditions for the Riemann problem

The inviscid fluxes are obtained assuming a linear data variation within each cell, for second order accuracy. The left initial state for the Riemann problem at face J is given by:

$$q_i^J = q_i + \vec{r}_i^J \cdot \vec{\nabla} q_i \quad (97)$$

where q_i^J - Estimated value

$\vec{\nabla} q_i$ - Gradient vector for cell i

\vec{r}_i^J - Vector from the centroid of cell i to the centroid of cell J Similarly, the right initial state can be found out. The gradient vector for cell i is found by a least squares solution to the above equation. Replacing the unknown value at the face centroid with the known value at the centroid of cell j , and then considering all the nearest-neighbour cells of cell i , we get the matrix relation:

$$A \vec{\nabla}^c q_i = q_m - q_i \quad (98)$$

In the above relation, $\vec{\nabla}^c q_i$ is called the central difference gradient as it is based upon all the nearest neighbour cells of i . A is over-determined as a result of each cell having more nearest neighbours (equations) than unknowns. The solution is obtained by QR factorization instead of an LU decomposition as QR factorization is more stable especially for the high aspect ratio cells of the boundary layer. Constructing the gradient requires a matrix-vector multiplication yielding,

$$f \vec{\nabla}^c q_i = \sum_{m=1}^{N_i} \vec{\omega}_i^m (q_m - q_i) \quad (99)$$

where $\vec{\omega}_i^m = R^{-1}Q_i^t{}^m$ is the least-squares weights vector of cell i associated with nearest-neighbour cell m as a result of QR factorization of A . The least-squares weights vectors, $\vec{\omega}_i^m$ are computed only once and stored as they are grid-related quantities. A central difference gradient is used for extremal values at the cell centroids. In case of a non-extremal case, a one-sided difference least-squares gradient is used. A Total Variation Diminishing(TVD) scheme is used to limit the extremes at the cell faces. In regions of extrema, one-sided differencing is used resulting in a “fully-upwind” scheme. The left and right values of a given fluid quantity are computed for every face in the grid, and a cell producing a local extrema is flagged. A one-sided difference gradient is then computed for each face of every flagged cell. The fluid quantity at each face of the flagged cell is recomputed using the one-sided difference scheme for the particular face. If the recomputed fluid quantity remains, or becomes extremal, it is limited, by setting a value which is the highest of the left and right cell centroid values. A one-sided, least-squares gradient can then be obtained through a simple correction to the original central difference, least-squares gradient. The basic concept is to correct the central-difference gradient in i by adjusting the state in j such that the error over the fit is minimized. We have,

$$\frac{\delta}{\delta q_j} \sum_m^U e_m^2 = 0 \quad (100)$$

where:

$$e_m = q_m - (q_i + \vec{r}_i^m \cdot \vec{\nabla}^c \cdot q_i) \quad (101)$$

where U is the set of all flagged cells, e_m is the error of fit at all the neighbouring cells using the central difference, and \vec{r}_i^m is the vector connecting the centroid of one cell with the centroid of the neighbouring cell. This results in:

$$\vec{\nabla}^{oJ} q_i = \vec{\nabla}^c q_i + \vec{\omega}_i^j \frac{\sum_m^U e_m (\vec{r}_i^m \cdot \vec{\omega}_i^j)}{\sum_m^U (\vec{r}_i^m \cdot \vec{\omega}_i^j)^2} \quad (102)$$

where $\vec{\nabla}^{oJ} q_i$ is the one-sided least-squares gradient in cell i associated with the face J and $\vec{\omega}_i^j$ is the least-squares weights vector of cell i associated with nearest neighbour cell j . If the nearest cell neighbours fail to produce a change in the values, the resulting set of U is regarded as incomplete. This poses a problem as the correction procedure described above assumes only one nearest-neighbour cell must be eliminated from the central difference stencil. This problem can be corrected by eliminating the contribution of the flagged cells from the central difference fluxes before applying the corrections. Limiting is vital as it ensures stability and for this, dissipative effects should be avoided. This makes first order schemes better than second order schemes. The Riemann problem is solved by a combination of the approximate Riemann method of Colella (2) and Newton’s procedure of Gottlieb and Groth (60).

Viscous Fluxes

The formulation of the viscous terms should have two attributes - it must be conservative and it must satisfy the discrete maximum principle. The ratio of the eddy viscosity to the molecular value has high values in certain regions of the grid. This means that in these regions, the viscous fluxes dominate the inviscid fluxes. Viscous fluxes are required to add to the stability of the flow solver. Eventhough, they are expensive and they account for a huge fraction of the computational time, their calculation is worth the effort due to the reliability and convergence properties. The formulation of the viscous terms should be conservative and must satisfy the discrete minimum principle. Conservation can easily be satisfied by constructing viscous fluxes for the faces, but simultaneously satisfying the other conditions is difficult. Efforts are still on to construct a gradient for the viscous fluxes that would satisfy all the conditions. Current studies use a reasonably good assumption which has yielded satisfactory results (36). To accurately capture the gradients in the boundary layers, the cells are compressed in the direction of the velocity gradient.

Temporal Integration

A brief description of temporal integration is outlined below. The governing equations are recast as:

$$\theta(V \frac{\delta Q}{\delta t} + \vec{\nabla} \cdot \vec{f})_i^{n+1} + (1 - \theta)(V \frac{\delta Q}{\delta t} + \vec{\nabla} \cdot \vec{f})_i^n = 0 \quad (103)$$

where \vec{f} is the flux vector while the superscripts n and n+1 denote successive time levels and $0 \leq \theta \leq 1$ where θ blends the temporal integration scheme from fully explicit ($\theta = 0$) to fully implicit ($\theta = 1$). The discrete forms of the temporal derivatives are:

$$(\frac{\delta Q}{\delta t})^{n+1} = \frac{\alpha_{1,1}(Q^{n+1} - Q^n) + \alpha_{1,2}(Q^n - Q^{n-1})}{\Delta t} \quad (104)$$

$$(\frac{\delta Q}{\delta t})^n = \frac{\alpha_{2,1}(Q^{n+1} - Q^n) + \alpha_{2,2}(Q^n - Q^{n-1})}{\Delta t} \quad (105)$$

The flux at t^{n+1} is obtained by noting that $\vec{f} = \vec{f}(Q)$ and forming a Taylor series expansion about t^n .

$$\vec{f}^{n+1} = \vec{f}^n + (\frac{\delta \vec{f}}{\delta Q})^n (Q^{n+1} - Q^n) + O(\Delta t^2) \quad (106)$$

$$= \vec{f}^n + \hat{A} \Delta Q + O(\Delta t^2) \quad (107)$$

where $\hat{A} = \frac{\delta \vec{f}}{\delta Q}$ is the flux Jacobian matrix. This is split into two to account for the upstream and the downstream signal propagation.

$$\hat{A} \Delta Q = \hat{A}^+ \Delta Q^+ + \hat{A}^- \Delta Q^- \quad (108)$$

Substituting this in the governing equation for temporal integration, and rearranging we get an equation in matrix notation as :

$$LHS(Q^{n+1} - Q^n) = RHS \quad (109)$$

Computation of the analytical viscous and inviscid flux Jacobians, due to the nature of the Riemann solver is expensive. So the Jacobians of the Van Leer splitting methods are used. The splitting involves a temporal damping term which tends to make LHS diagonally dominant. The flux Jacobian matrix \hat{A} is split as

$$\hat{A}^\pm = \hat{A} \pm I\beta\lambda_{max} \quad (110)$$

where $[\lambda_{max} = \vec{V} \cdot \hat{n} + c]$, \vec{V} is the velocity vector, c is the speed of sound, β is the temporal damping term. The viscous fluxes ensure robustness and are split using a simplified eigenvalue approach. Temporal damping may be used when large time steps are used, but this leads to a decrease in the temporal accuracy and therefore a sufficiently small timestep is used so that the temporal damping is very less. However, the addition of temporal damping to the viscous fluxes leads to an improvement in the stability of the solution. This matrix is solved iteratively using a symmetric Gauss-Seidel procedure. Newtons sub-iterations have been used to increase the temporal accuracy of the unsteady problems. This implicit scheme is stable for any Courant-Freidrichs-Lewy(CFL) number, but generally a value of 10^6 , is used as recommended by Strang *et al.* (36).

Parallelization of the code

Originally, Cobalt was written in FORTRAN 77, but was then rewritten in FORTRAN 90 to take advantage of the new features such as runtime usage of memory and parallelization of the code. In the new code, it is also possible to reduce memory requirements when the user requests simpler physics or simpler numerics. Using FORTRAN 90 significantly improves software modularity and maintainability.

The parallel version is based on the domain decomposition of the grid, according to which each processor operates on a subsection (zone) of the original grid. Message Passing Interface (MPI) is used to pass information between the processors. A variety of MPI features such as non-blocking communications, persistent communication requests and vector MPI datatypes are used to minimize the communication overhead. The zonal boundaries are computed exactly the same manner as the zonal interiors. At the zonal boundaries, the conserved variables for each boundary cell, the initial conditions for the Riemann problem for each boundary face and the gradients in each boundary cell (viscous cases only) are passed to the processors.

A preprocessing program is used to partition the grid into zones. The intermediate decomposition is done by METIS (15). This helps in creating almost equally balanced zones in such a way that the sizes of the zones are almost identical and excellent load balancing is achieved between

the processing nodes. A block Gauss-Siedel scheme is used along with sub-iterations to increase the temporal accuracy of unsteady problems.

References

- [1] Bradshaw, P., Ferriss, D.H. and Atwell, N.P., “ Calculation of boundary layer development using the turbulent energy equation”, *J. Fluid Mech.* 23(31), 1967.
- [2] Colella, P., “Glimm’s method for gas dynamics”,*SIAM J. of Scientific Computing*, Vol. 3, No. 1, March 1982.
- [3] Moser, R., Moin, P. and Kim, J., “Turbulence Statistics in Fully Developed Channel Flow at Low Reynolds Number”, *J. Fluid Mech.*, 1987.
- [4] Balaras, E., Benocci, C. and Piomelli, U., “ Two-layer approximate boundary conditions for large-eddy simulations”, *AIAA Journal*,34, 1111.1996.
- [5] Balaras, E. and Benocci, C., “Subgrid-scale models in finite-difference simulations of complex wall bounded flows”, AGARD CP 551, 1994.
- [6] Cabot, W.H., “Near-wall models in large-eddy simulations of flow behind a backward-facing step”,*Annual Research Briefs–1996*, Center for Turbulence Research, Stanford University, pp.199-210.
- [7] Diurno, G.V., Balaras, E. and Piomelli, U., “Wall-layer models for LES of separated flows”, *Modern Simulation Strategies for Turbulent Flows*, Edwards, pp. 207-222.
- [8] Wang, M. and Moin, P., “ Dynamic wall modeling for large-eddy simulation of complex turbulent flows”, *Phys.Fluids* 14, pp. 2043 2051, 2002.
- [9] Baggett, J.S., “ On the feasibility of merging LES with RANS in the near-wall region of attached turbulent flows”, *Annual Research Briefs1998*, Center for Turbulence Research, Stanford University, pp.267277, 1998.
- [10] Spalart, P. R. and Watmuff, J. H., “Experimental and numerical study of a turbulent boundary layer with pressure gradients”, *J. Fluid Mech.*, 249, 1993.
- [11] Li, N., Balaras, E. and Piomelli, U., “Inflow conditions for large-eddy simulations of mixing layers”, *Phys. Fluids*, **12**, 935, 2000.
- [12] Piomelli, U., Balaras, E. and Pascarelli, A., “Turbulent structures in accelerating boundary layers”, *Journal of Turbulence*, **1**, 1, 2000.
- [13] Le, H., Moin, P. and Kim, J., “Direct numerical simulation of turbulent flow over a backward-facing step”, *J. Fluid Mechanics*, **330**, 349, 1997.
- [14] Lee, S., Lele, S. and Moin, P., “Simulation of spatially evolving compressible turbulence and application of Taylor’s hypothesis”, *Phys. Fluids A*, **4**, 1521, 1992.
- [15] Karypis. G.,Schhloegel, K., and Kumar, V,*ParMETIS: Parallel Graph Partitioning and Sparse Matrix Ordering Library Version 1.0* Department of Computer Science,University of Minnesota, Department of Computer Science, Minneapolis, MN 55455, July 1997.
- [16] Strelets, M., “Detached Eddy Simulation of Massively Separated Flows”, *AIAA Paper 2001-0879*, 2001.

- [17] Squires, K.D., Forsythe, J.R., Morton, S.A., Strang, W.Z., Wurtzler, K.E., Tomaro, R.F., Grismer, M.J. and P.R. Spalart, "Progress on Detached-Eddy Simulation of massively separated flows", *AIAA Paper 2002-1021*, 2002.
- [18] Shur, M., Spalart, P. R., Strelets, M., and Travin, A, "Detached-Eddy Simulation of an Airfoil at High Angle of Attack, 4th Int. Symp. Eng. Turb. Modelling and Measurements, Corsica, May 24-26, 1999.
- [19] Rodi, W., Turbulence models and their application in hydraulics - *A State-of-the-Art Review*, IAHR Publication.
- [20] Germano, M., Piomelli, U., Moin, P. and Cabot, W., "A dynamic subgrid-scale eddy viscosity model", *Phys. Fluids A* 3, 1760, 1991.
- [21] Kundu, P.K., Fluid Mechanics, 638 pp., Academic Press, 1990.
- [22] Chapman, D.R., "Computational aerodynamics development and outlook", *AIAA Journal*, 17, 1293-1313, 1979.
- [23] Spalart, P.R., Deck, S., Shur, M.L., Squires, K.D., Strelets, M.Kh. and Travin, A., "A new version of Detached-Eddy Simulation, resistant to ambiguous grid densities", *Theoretical and Computational Fluid Dynamics*, 20(3), 2006.
- [24] Durbin, P.A. and Pettersson Reif, B.A., "Statistical Theory and Modeling for Turbulent Flow", Wiley, 2001.
- [25] Pope, S.B., "Turbulent Flows", Cambridge Univ. Press, UK, 2000.
- [26] Spalart, P. R. , Jou W-H. , Strelets M. and Allmaras, S. R., "Comments on the Feasibility of LES for Wings, and on a Hybrid RANS/LES Approach," *Advances in DNS/LES, 1st AFOSR Int. Conf. on DNS/LES*, Aug 4-8, 1997, Greyden Press, Columbus Oh.
- [27] Spalart, P.R. and Allmaras, S.R., " A One- Equation Turbulence model for Aerodynamic Flows." *La Recherche Aerospatiale*, No 1, 1994, pp 5-21.
- [28] Hansen, R. and Forsythe, J., "Large and Detached Eddy Simulations of a Circular Cylinder Using Unstructured Grids." *AIAA 2003-0775*, 2003.
- [29] Gleyzes, C., "Opération décrochage – résultats de la 2ème campagne d’essais à F2 – Mésures de pression et vélocimétrie laster", Tech. Rep. RT-DERAT 55/5004, ONERA, 1989.
- [30] Huddeville, R., Piccin, O. and Cassoudealle, D., "Opération décrochage – mesurement de frottement sur profils AS 239 et A 240 á la soufflerie F1 du CFM", Tech. Rep. RT-OA 19/5025 (RT-DERAT 19/5025 DN), ONERA, 1987.
- [31] Mellen, C.P., Frolich, J. and Rodi, W., "Lessons from the European LESFOIL project on LES of flow around an airfoil", *AIAA Paper 2002-0111*, 2002.
- [32] Steinbrenner, J., Wyman, N. and Chawner, J., "Development and Implementation of Gridgen’s Hyperbolic PDE and Extrusion Methods", *AIAA Paper 2000-0679*, 2000.
- [33] Mary, I. and Sagaut, P., "Large Eddy Simulation of flow around an airfoil near stall", *AIAA Journal*, Vol. 40, 2002, pp. 1139-1145.

- [34] Pirzadeh, S., "Unstructured Viscous Grid Generation by Advancing-Front Method", NASA CR 191449, Apr 1993
- [35] Spalart, P.R., "Young-Person's Guide to Detached Eddy Simulation Grids", *NASA/CR-2001-211032*, July 2001.
- [36] Strang, W. Z., Tomaro, R. F. and Grismer, M. J., "The Defining Methods of Cobalt₆₀: a Parallel, Implicit, Unstructured Euler/Navier-Stokes Flow Solver," *AIAA 99-0786*, January 1999.
- [37] Menter, F. R., Kuntz, M. and Durand, L., "Adaptation of eddy-viscosity turbulence models to unsteady separated flow behind vehicles", *Aerodynamics of Heavy Vehicles: Trucks, Buses and Trains*, 19, 2004, Springer-Verlag, Berlin.
- [38] Samareh-Abolhassani, J., "GridTool: A Structured Modeling and Grid Generation Tool", *Proceedings of the Workshop on Surface Modelling, Grid Generation, and Related Issues in CFD Solutions, NASA CP -3291*, May 1995
- [39] Strang, W.Z., "Parallel Cobalt User's manual", June 1999.
- [40] Piomelli, U., Balaras, E., Pasinato, H., Squires, K.D. and Spalart, P.R., "The inner-outer layer interface in Large-Eddy Simulations with wall-layer models", *International Journal of Heat and Fluid Flow*, **24**, pp. 538-550, 2003.
- [41] Travin, A., Shur, M., Spalart, P.R. and Strelets, M., "On URANS solutions with LES-like behavior", *European Congress on Computational methods in applied Sciences and Engineering (ECCOMAS)*, Jul, 2004.
- [42] Menter, F.R., Kuntz, M. and Bender, R., A Scale-Adaptive Simulation Model for Turbulent Flow Predictions, *AIAA 2003-0767*.
- [43] Batten, P., Goldberg, U. and Chakravarthy, S., LNS - An approach towards embedded LES, *AIAA 2002-0427*.
- [44] Forsythe, J. R., Fremaux, C. M. and Hall, R. M., Calculation of Static and Dynamic Stability Derivatives of the F/A-18E in Abrupt Wing Stall using RANS and DES, *3rd International Conference on CFD*, Toronto, Canada, July 2004.
- [45] Spalart, P. R., "Numerical study of sink-flow boundary layers", *J. Fluid Mechanics*, **172**, 307, 1986.
- [46] Spalart, P. R., "Direct Simulation of a turbulent boundary layer up to $Re_\theta = 1410$ ", *J. Fluid Mechanics*, **187**, 61, 1986.
- [47] Keating, A., Piomelli, U., Balaras, E. and Kaltenbach, H.-J., "A priori and a posteriori tests of inflow conditions for Large-Eddy Simulation", *Physics of Fluids*, **16**(12), pp. 4696-4712, 2004.
- [48] Hoffman, K.A. and Chiang, S.T., *Computational Fluid Dynamics - Volume II, Engineering Education System, Third Edition*, 1998, pp 312 - 319.

- [49] Spalart, P. R., "Strategies of turbulence modelling and simulations" *Int. J. of Heat and Fluid Flow* 21, 2000.
- [50] Spille-Kohoff, A. and Kaltenbach, H.-J., "Generation of turbulent inflow data with a prescribed shear-stress profile", *Third AFOSR International Conference on DNS/LES*, 5-9 August 2001, Arlington, TX. *DNS/LES Progress and Challenges*, editors, Liu. C., Sakell, L. and Beutner, T., Greyden, Columbus, OH, 2001.
- [51] Squires, K.D., Forsythe, J.R., Morton, S.A., Strang, W.Z., Wurtzler, K.E., Tomaro, R.F., Grismer, M.J. and Spalart, P.R., "Progress on Detached-Eddy Simulation of massively separated flows", *AIAA Paper 2002-1021*, 2002.
- [52] Spalart, P.R. and Shur, M.L., "On the Sensitization of Turbulence Models to Rotation and Curvature", *Journal of Fluid Mechanics*, 358, pp. 223, 1997.
- [53] Morton, S.A., Forsythe, J.R., Squires, K.D. and Wurtzler, K.E., "Assessment of unstructured grids for Detached-Eddy Simulation of high Reynolds number separated flows", *Proceedings of the Eighth International Conference on Numerical Grid Generation in Computational Field Simulations*, 2002.
- [54] Squires, K.D., Forsythe, J.R., Morton, S.A., Blake, D.C., Serrano, M., Wurtzler, K.E., Strang, W.Z., Tomaro, R.F. and Spalart, P.R., "Analysis of full aircraft with massive separation using Detached-Eddy Simulation", *Proceedings of the High Performance Computing Modernization Program 2002 Users Group Conference*, Austin, Texas, 2002.
- [55] Garriz, Javier A., "VGRID 3.2 - Reference Documents", Sep 1998.
- [56] Shur, M., Spalart, P. R., Strelets, M. and Travin, A., "Detached-Eddy Simulation of an Airfoil at High Angle of Attack", *4th Int. Symp. Eng. Turb. Modelling and Measurements*, Corsica, May 24-26, 1999.
- [57] Travin, A., Shur, M., Strelets, M. and Spalart, P.R., "Detached Eddy Simulations past a Circular Cylinder", *Flow, Turb and Combustion* 63 2000.
- [58] Colella, P., "Glimm's method for gas dynamics", *SIAM Journal of Stat. Comput.* March 1982.
- [59] Godunov, S. K., "A difference scheme for numerical computation of discontinuous solution of hydrodynamic equations", *Sbornik Mathematics*, 47:271-306, 1959.
- [60] Gottlieb, J. J. and Groth, C. P. T., "Assessment of Riemann solvers for unsteady one-dimensional inviscid flows of perfect gases." *Journal of Computational Physics*, 78:437-458, 1988
- [61] Keating, A., Prisco, G. D., Piomelli, U. and Balaras, E., "Interface conditions for hybrid RANS/LES calculations", *ERTOFAC International Symposium on Engineering Turbulence Modelling and Measurements*, Sardinia, Italy, 2005.
- [62] Lund, T.S., Wu. X. and Squires, K.D., "Generation of inflow data for spatially-developing turbulent boundary layer simulations", *Journal of Computational Physics*, 140, 233, 1998.
- [63] Cebeci, T. and Smith, A.M.O., "A finite-difference method for calculating compressible laminar and turbulent boundary layers", *Journal of Basic Engineering*, Vol. 92, No. 3, pp.523-535

- [64] Baldwin B. S. and Lomax, H., "Thin layer approximation and algebraic model for separated turbulent flows", AIAA-78-257.
- [65] Johnson, D. A. and King, L.S., "A mathematically simple turbulence closure model for attached and separated turbulent boundary layers", *AIAA Journal*, Vol. 23, No. 11, 1985, pp.1684-1692.
- [66] Launder, B. E. and Tselepidakis, D. P., "Directions in second-moment modeling of near wall turbulence", AIAA-91-0219.
- [67] Baldwin B. S. and Barth T. J., "A one-equation turbulence transport model for high Reynolds number wall-bounded flows", AIAA-91-0610.
- [68] Hunt J.C.R., "Developments in Computational Modelling of Turbulent Flows", Proceedings of ERCOFTAC Workshop at EPFL, 26-28 March 1990, Lausanne, Switzerland.
- [69] Batten, P., Goldberg U. and Chakravarthy, S., "Interfacing statistical turbulence closures with large-eddy simulation", *AIAA Journal*, **42**, 485, 2004.
- [70] Roshko, A., "Experiments on the Flow past a Circular Cylinder at Very High Reynolds Number", *Journal of Fluid Mechanics*, 10 (1961), 345-356.
- [71] van Nunen, J., "Pressure and Forces on a Circular Cylinder in a Cross Flow at High Reynolds Number", *Flow Induced Structural Vibrations*, Springer-Verlag, Berlin, 1974.
- [72] Nikitin, N.V., Nicoud, F., Wasistho, B., Squires, K.D. and Spalart, P.R., An approach to wall modeling in Large-Eddy Simulation, *Physics of Fluids*, 12(7), pp. 1629-1632, 2000.
- [73] Karypis, G., Schloegel, K. and Kumar, V., *ParMETIS: Parallel Graph Partitioning and Sparse Matrix Ordering Library Version 1.0*. University of Minnesota, Department of Computer Science, Minneapolis, MN 55455, July 1997.
- [74] Menter, F.R., "Improved Two equation $k-\omega$ turbulence models for aerodynamic flows", *NASA Technical memorandum 103975*, October 1992.
- [75] Whitaker, H. P., "An Adaptive System for Control of the Dynamics Performances of Aircraft and Spacecraft", Inst. Aeronautical Services, 59-100, 1959.